



**UTILIZING MICRO-ELECTRO-MECHANICAL SYSTEMS (MEMS) MICRO-  
SHUTTER DESIGNS FOR ADAPTIVE CODED APERTURE IMAGING (ACAI)  
TECHNOLOGIES**

**THESIS**

Mary M. Ledet, Captain, USAF

AFIT/GEO/ENG/09-03

**DEPARTMENT OF THE AIR FORCE  
AIR UNIVERSITY**

***AIR FORCE INSTITUTE OF TECHNOLOGY***

---

---

**Wright-Patterson Air Force Base, Ohio**

APPROVED FOR PUBLIC RELEASE; DISTRIBUTION UNLIMITED

The views expressed in this thesis are those of the author and do not reflect the official policy or position of the United States Air Force, Department of Defense, or the U.S. Government.

AFIT/GEO/ENG/09-03

**UTILIZING MICRO-ELECTRO-MECHANICAL SYSTEMS (MEMS) MICRO-  
SHUTTER DESIGNS FOR ADAPTIVE CODED APERTURE IMAGING (ACAI)  
TECHNOLOGIES**

THESIS

Presented to the Faculty

Department of Electrical and Computer Engineering

Graduate School of Engineering and Management

Air Force Institute of Technology

Air University

Air Education and Training Command

In Partial Fulfillment of the Requirements for the  
Degree of Master of Science in Electrical Engineering

Mary M. Ledet, BSEE

Captain, USAF

March 2009

APPROVED FOR PUBLIC RELEASE; DISTRIBUTION UNLIMITED


AFIT/GEO/ENP/09-03

**UTILIZING MICRO-ELECTRO-MECHANICAL SYSTEMS (MEMS) MICRO-  
SHUTTER DESIGNS FOR ADAPTIVE CODED APERTURE IMAGING (ACAI)  
TECHNOLOGIES**


Mary M. Ledet, BSEE

Captain, USAF

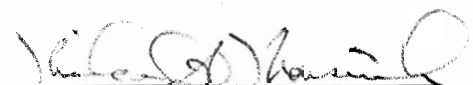
Approved:

  
\_\_\_\_\_  
LaVern A. Starman, PhD, Major, USAF (Chairman)

26 Feb 09  
Date

  
\_\_\_\_\_  
Ronald A. Coutu, Jr., PhD, LtCol, USAF (Member)

17 Feb 09  
Date

  
\_\_\_\_\_  
Michael A. Marciniak, PhD (Member)

17 Feb 09  
Date

## **Abstract**

The Air Force has long relied on surveillance for intelligence and strategic purposes. Most surveillance systems rely on a lensing system to acquire their images, most of which are in either the visible or infrared wavelengths. Because lensing systems can be expensive, obtrusive, or hard to maintain, researchers have designed adaptive coded aperture imaging (ACAI) as a replacement system. Coded aperture imaging (CAI) has been used in both the astronomical and medical communities for years due to its ability to image light at short wavelengths and thus replacing conventional lenses. Where CAI is limited, researchers have discovered that adaptive coded aperture imaging can recover what is lost. ACAI uses a reconfigurable coding mask and digital signal processing to recover the original scene from the detector.

In this effort, a prototype of MEMS microshutters has been designed and fabricated onto a 3 mm x 3 mm square of silicon substrate using the PolyMUMPS™ process. This prototype is a line-drivable array using thin flaps of polysilicon to cover and uncover an 8 x 8 array of 20  $\mu\text{m}$  apertures and is the first known microshutter array to incorporate a line-drivable array driven by physical actuation. A characterization of the micro-shutters to include mechanical, electrical and optical properties is provided. This prototype, its actuation scheme, and other designs for individual microshutters have been modeled and studied for feasibility purposes, and this revealed that the actuation scheme failed in its design due to oversights in the design process and lack of space for

each gear actuator. Because of conformality in the PolyMUMPS™ process, none of the microshutters could physically move, but optical analysis with a 632 nm HeNe laser revealed that they will not undergo upward deflection when exposed to irradiance sources of less than 0.5 W. The microshutters were also designed to transmit less than 20% of irradiated light and initial testing confirmed that fact. In addition, microshutters fabricated from an Al-Au alloy on a quartz wafer were characterized and showed that wedge-style shutters are functional, if not ideal for an ACAI array.

## **Acknowledgments**

I'd like to thank Major Starman, LtCol Coutu, and Dr. Marciniak for their expertise and insight regarding this research for the past months. I'd especially like to thank Maj Starman for being a patient but steady guide through this thesis work—your help was immeasurable, and I'll always appreciate your support. I'll also be willing to argue the merits of Notre Dame football over Nebraska anytime. Thanks especially to my fellow MEMS classmates: Coleman, Dan, Adam, Moe, Tod, Tom, Luke, and James. You guys kept me sane throughout all this madness, and I will miss the daily banter, lunch conversations, philosophical discussions, and silly office pranks. Thanks also to my fellow section mates: Sean, Neil, Rob, Steve, Steve, Travis, Jeremy, Al, and Spud. I couldn't have asked for a better crew of assigned friends, and I hope our paths cross again someday.

Finally, I owe it all to my family—to my mom and dad, without whom I'd have never pushed for engineering in the first place, let alone pursue my master's degree. Thank you for your continuous support and confidence in my abilities even when I had none. To my sisters, you are my closest of friends, and thank you for your patience and your phone calls these past 18 months. To my brother, I'm proud of you and wish you the best of luck in your future engineering and Air Force career. I love you all dearly, and as cliché as it is, I couldn't have done it without you.

Mary M. "Mimi" Ledet

## Table of Contents

	Page
<b>Abstract.....</b>	<b>iv</b>
<b>Acknowledgments .....</b>	<b>vi</b>
<b>Table of Contents .....</b>	<b>vii</b>
<b>Table of Figures.....</b>	<b>xi</b>
<b>List of Tables .....</b>	<b>xviii</b>
<b>Acronym List .....</b>	<b>xix</b>
<b>1. Introduction.....</b>	<b>1</b>
1.1 Coded Aperture Imaging Description.....	1
1.2 Microshutter Fundamentals .....	3
1.3 Problem Background .....	3
1.4 Microshutters Design Proposal .....	4
1.5 Summary .....	5
<b>2. Background .....</b>	<b>6</b>
2.1 ACAI Fundamentals .....	6
2.2 Current Research and Development on Applications of Microshutters .....	8
2.2.1 <i>James Webb Space Telescope</i> .....	9
2.2.2 <i>Adaptive Coded Aperture Imaging</i> .....	11
2.2.3 <i>Others</i> .....	17
2.3 MEMS Fabrication Process .....	23
2.4 MEMS Actuation Techniques.....	25



2.4.1 <i>Electrostatic Actuation</i> .....	26
2.4.2 <i>Electro-thermal Actuation</i> .....	28
2.4.3 <i>Scratch Drive Actuators</i> .....	32
2.4.4 <i>Other Actuators</i> .....	34
2.5 Introduction to MEMS Microshutter Design Concept.....	35
2.6 Summary .....	35
<b>3. Methodology .....</b>	<b>37</b>
3.1 MEMS Design Concepts.....	37
3.1.1 <i>Wedge-style shutter using electro-thermal actuation</i> .....	37
3.1.2 <i>Final line-drivable array design</i> .....	42
3.2 Component Breakdown .....	43
3.2.1 <i>Shutter array</i> .....	43
3.2.2 <i>Individual gear assemblies</i> .....	47
3.3 Microshutter Implementation.....	53
3.3.1 <i>Microshutter Preparation</i> .....	53
3.3.2 <i>Integration and Assembly</i> .....	54
3.4 Chapter Summary .....	55
<b>4. Analytical Modeling .....</b>	<b>57</b>
4.1 Electro-Thermal Actuator .....	57
4.1.1 <i>Electro-Thermal Actuator Analysis</i> .....	57
4.1.2 <i>Wedge-style Shutters using Electro-Thermal Actuation</i> .....	60
4.1.3 <i>Electro-thermal Actuator Summary</i> .....	62
4.2 Coupled Electro- Thermal Actuators .....	63

4.2.1 Coupled Actuator Designs .....	64
4.2.2 Coupled Actuator Analysis .....	66
4.3 Two-Dimensional Electro-Thermal Gear Actuator .....	69
4.4 Optical Modeling .....	73
4.5 Chapter Summary .....	80
<b>5. Results .....</b>	<b>82</b>
5.1 Fabrication Results.....	82
5.1.1 PolyMUMPS™ Run 83 Fabrication Results .....	83
5.1.2 PolyMUMPS™ Run 84 Fabrication Results .....	86
5.2 AFRL Quartz Wafer Results.....	90
5.3 Optical Results .....	92
5.4 Results Summary .....	95
<b>6. Conclusions and Recommendations .....</b>	<b>97</b>
6.1 Thesis Objectives Restated .....	97
6.2 Conclusions .....	97
6.3 Recommendations .....	98
<b>A. Appendix A .....</b>	<b>100</b>
A-1 PolyMUMPS™ Failed Wedge Shutter Designs.....	100
A-2 Failed iris-style shutter using scratch drive actuation.....	102
A-3 Failed flat shutter using scratch drive actuation .....	103
<b>B. Appendix B .....</b>	<b>104</b>
B-1 PolyMUMPS™ Run 83 Submission.....	104
B-2 PolyMUMPS™ Run 84 Submission.....	105

<b>References.....</b>	<b>106</b>
------------------------	------------

## Table of Figures

### Page

Figure 1-1: Basic principle of coded aperture imaging (CAI). [3] .....	2
Figure 2-1: Illustration of the principle of conventional CAI. Light from every point in a scene within the field-of-view (FOV) casts a shadow of the aperture onto the detector array. The detector then measures the sum of the irradiances it receives, and the image is decoded through deconvolution of the irradiance sums [6]. .....	7
Figure 2-2: Different advantages of ACAI without macroscopic moving parts. On the left is a steerable FOR. On the right are two images of adjustable FOV [6]. .....	7
Figure 2-3: Illustration of how ACAI works. [6].....	8
Figure 2-4: Array of microshutters on the JWST. [7].....	10
Figure 2-5: Individual JWST shutter being activated by a probe. [4] .....	10
Figure 2-6: SEM picture of a single JWST shutter. [7] .....	10
Figure 2-7: (left) Fully functional 128 by 64 pixel model of the JWST array. (right) Demo of model array displaying JWST acronym. [7].....	11
Figure 2-8: (left) Scanning Electron Microscope (SEM) image of a single eyelid microshutter 50 $\mu\text{m}$ long and 50 $\mu\text{m}$ wide. This eyelid was manufactured with ridges etched along the width of the microshutter to encourage uniformed curling. (right) SEM image of an eyelid shutter 200 $\mu\text{m}$ long and 50 $\mu\text{m}$ wide. Note the difference in the curl between the two eyelids [10]. .....	12
Figure 2-9: SEM image of failed curling of eyelids. [10].....	13
Figure 2-10: Combination of eyelid microshutter panel with microprisms and micropistons. The shutters are designed to limit look direction, the prisms provide the look direction, and the pistons allow the prisms to move vertically to provide a clear line-of-sight to the scene being imaged, as well as providing the necessary phase corrections for each look direction. [11].....	14
Figure 2-11: Fabry-Perot interferometer microshutter design for MWIR. As a voltage is passed to the moveable mirror, the gap begins to decrease, which then affects which wavelengths will be passed to the buried electrode. [5] .....	16

Figure 2-12: Microscope image of 3 x 3 Fabry-Perot microshutter array. The wiring via rows and columns allows each microshutter to be individually driven, as they only respond to signals in both electrodes. [5].....	16
Figure 2-13: SEM picture of an individual VOA shutter. [12] .....	17
Figure 2-14: (top) Mask layout for VOA shutter. (bottom) SEM picture of self-assembled VOA microshutter. [13] .....	19
Figure 2-15: (a) VOA microshutter before actuation. (b) VOA microshutter after actuation. Note the extended microsprings and the location of the scratch drive actuators. [13].....	20
Figure 2-16: a) 3D cross-section of an individual shutter-blade. b) Cross-sectional actuation of shutter-blade in closed position. c) Shutter-blade in open position. [8] ...	21
Figure 2-17: a) Array of shutter-blades. b) Photo of a shutter-blade moving from fully closed (1) to fully open (4). [8] .....	22
Figure 2-18: Cross sectional view of all seven layers of the PolyMUMPs™ process (not to scale). The two oxide layers are sacrificial layers, and the nitride, or isolation layer, is the surface which provides the foundation for the device; it is grown on a (100) silicon wafer [14]. .....	24
Figure 2-19: Force diagram for a parallel plate electrostatic actuation device [16]. .....	27
Figure 2-20: MEMS electro-thermal technique illustrating beam elongation due to Joule heating caused by current flow through the conductor material. $L_0$ is the initial beam length; $L_{new}$ is the new total length of the beam after thermal expansion; $A$ is the cross-sectional area of the beam; and $\Delta L$ is the change in beam length [15]. .....	29
Figure 2-21: Single hot-arm electro-thermal actuator showing increasing force and displacement with increasing applied voltage [16]. .....	30
Figure 2-22: a) Diagram of current flowing through a single hot-arm thermal actuator. b) Diagram of current flowing through a double hot-arm thermal actuator. [16] .....	31
Figure 2-23: Side view of a scratch drive actuator showing the four main components and where the voltage is applied [17]. .....	33
Figure 2-24: (State 1) The SDA is at rest before actuation. (State 2) Positive voltage is applied to the SDA, pulling down the plate. (State 3) Voltage is removed from the plate, causing the bushing to press forward along the insulator. (State 4) Negative voltage is applied, causing the plate to warp towards the insulator. The forward movement is denoted by $DX$ , the length of the plate by $L$ , and the warped portion of the plate by $L_p$ . Once actuated, the SDA will alternate between State 2, State 3, State 4, and State 3 again to provide the forward movement [17]. .....	34

Figure 3-1: (left) The optical iris is shown fully open. (middle) The optical iris is shown half closed. (right) The optical iris is shown fully closed. .... 38

Figure 3-2: a) Test design of a quarter-wedge, single hot arm shutter. The hot arm is 250  $\mu\text{m}$  in length, and the wedge has a 100- $\mu\text{m}$  radius. This is a Poly1-2 stack with no trapped oxide layer. b) SEM picture of a single quarter-wedge single hot arm. .... 39

Figure 3-3: a) Test design of a sixth-wedge, single hot arm shutter. The hot arm is 200  $\mu\text{m}$  in length, and the wedge has a 100- $\mu\text{m}$  radius. This is a Poly1-2 stack with no trapped oxide layer, and the extra flaps of polysilicon allow for more conformal covering of the aperture. b) SEM picture of a single sixth-wedge, single hot arm shutter. .... 40

Figure 3-4: a) Test design of a quarter-wedge, single hot arm shutter. The hot arm is 250  $\mu\text{m}$  in length, and the wedge has a 100- $\mu\text{m}$  radius. This is a Poly1-2 stack with a trapped oxide layer. b) SEM picture of fabricated shutter. .... 41

Figure 3-5: a) Line-drivable array microshutter design. The square in the center of the design is the actual microshutter array, while everything else provides the actuation scheme to drive the array. b) Simplified layout of microshutter array. There are four line sliders and 16 gear actuators in all. .... 42

Figure 3-6: Aperture array that the microshutters are designed to cover. .... 44

Figure 3-7: Line-drivable microshutter array. As before in the previous designs, the light red color corresponds to the Poly1 layer, the grey corresponds to the Poly2 layer, and the dark red is where the two layers overlap. Closure springs are located at the end of each flap, and dimples are located where each aperture should be to minimize stiction when the apertures have not yet been etched. .... 45

Figure 3-8: (top) 3-D view of the original design for the microshutters. The conformal nature of the PolyMUMPS™ process causes the Poly2 layer to fill in the gaps between the shutters, which then keeps the Poly2 flap from moving. (bottom) Cross-section of the original shutter design accentuating where the Poly2 layer will fill in the gaps. .... 46

Figure 3-9: Illustrated representation of a single cycle of the 4-step pawl and drive mechanisms from a previous thesis effort; (a) shows the pawl pushing the drive gear to an engaged position; (b) depicts the drive actuators pulling in a linear motion causing the gear to rotate; (c) at the peak of the drive stroke, the pawl is released allowing the spring tension in the drive gear arm to clear the drive from the wheel gear teeth; (d) the drive actuator then returns to its original position and the process is repeated until the desired motion is achieved. [16] .... 48

Figure 3-10: Design (top) and SEM picture (bottom) of the slider mechanism that is attached to all flaps from the microshutter array. The gear teeth receive the actuation from the gear mechanism, the two Poly2 overlaps provide anchors to keep the flap from

floating away during the release, and the slider pin ensures movement only ranges from 0-20  $\mu\text{m}$ . ..... 49

Figure 3-11: Design of the individual gear actuator assembly. In this design, the pawl and drive gears are connected so that no slipping between the two mechanisms occurs during actuation. In this setup, the drive gear is actuated first, rather than the pawl as in Figure 3-9; the actuation is still a very similar 4-step process as before. .... 49

Figure 3-12: Example of the box spring incorporated at the end of each microshutter flap. The spring acts to keep the entire array closed when there are no electrical signals to the actuation scheme. .... 50

Figure 3-13: a) L-Edit design of how the lock actuator is incorporated into the gear actuator. Without having an electrical signal, the lock actuator prevents movement of the gear. b) SEM picture of two test full gear actuators with the lock actuator present. .... 51

Figure 3-14: Illustration of the final layout of the microshutter array design. Note the symmetry and the wiring scheme. .... 52

Figure 4-1: Applied voltage versus deflection curve for Poly1/Poly2 stacked 300- $\mu\text{m}$  single hot-arm actuator (shown on right); analysis modeled in CoventorWare® Version 6.0 [16]. .... 58

Figure 4-2: Applied voltage versus deflection curve for Poly1/Poly2 stacked 300- $\mu\text{m}$  double hot-arm actuator (shown on right); analysis modeled in CoventorWare Version 6.0 [16]. .... 59

Figure 4-3: CoventorWare® simulation of a Poly1/Poly2 stacked, 250- $\mu\text{m}$ -long quarter wedge shutter at both 5 V and 12 V. The aperture is 47  $\mu\text{m}$  when the shutter is at 12 V. .... 60

Figure 4-4: CoventorWare® simulation of a Poly1/Poly2 stacked, 200- $\mu\text{m}$ -long sixth wedge shutter at both 5 V and 12 V. The aperture is 33  $\mu\text{m}$  when the shutter is at 12 V. .... 61

Figure 4-5: Deflection vs. power curves for an individual wedge from each shutter type. These values were obtained from iterative studies in CoventorWare®. .... 62

Figure 4-6: CoventorWare® analysis of actuator displacement vs. applied power for both the single and double hot-arms. .... 63

Figure 4-7: L-Edit design of two coupled double hot-arm thermal actuators. .... 64

Figure 4-8: a) Two banked electro-thermal actuators coupled together to provide the pawl device for the gear actuator. b) Four coupled electro-thermal actuators banked together to provide the drive for the gear actuator. .... 65

Figure 4-9: Force vs. deflection curve for 1-5 banked electro-thermal actuators. [16] ...	66
Figure 4-10: Temperature charts depicting how the temperature of the electro-thermal actuators increases with deflection and voltage. The red horizontal line represents the melting point of polysilicon; failure points of the devices lie where this line intersects the curves. ....	68
Figure 4-11 : a) L-Edit design of combined pawl and drive device; while the design shows the original design of the pawl as it is combined with the drive, b) shows that no physical overlapping takes place. ....	69
Figure 4-12: Chart of deflections achieved with the gear actuator in both horizontal and vertical directions. ....	70
Figure 4-13: Comparison between step 1 and step 5 for the gear actuator. Step 1 represents when all inputs are at a minimum of 1 volt. Step 5 represents when all inputs are at a maximum of 8 volts; this is easily seen by the curvature in all six hot-arms as well as the tilting of the gear and pawl device and the bending of the driving arm in the horizontal direction. ....	71
Figure 4-14: Illustration of the 8 steps modeled in CoventorWare® for the gear actuator. ....	72
Figure 4-15: Charts illustrating the total power required to drive the gear actuator and how much deflection can be expected. ....	72
Figure 4-16: Experimental data that provides $\alpha$ and $\rho$ coefficients. At 632.8 nm, $\alpha$ is $9 \times 10^3 \text{ cm}^{-1}$ [22], and $\rho$ is 0.2 [23]. ....	75
Figure 4-17: Simulated image from CoventorWare® detailing the deflection of the microshutter array when the Poly2 layer has been heated to 1400K. The maximum deflection is seen near the ends of the shutter flaps and measures only 1 $\mu\text{m}$ upwards. ..	76
Figure 4-18: Representative thermal circuit for a fixed-fixed polysilicon beam. [20] ....	77
Figure 5-1: SEM pictures showing both the quarter wedge and sixth wedge shutter with wedges fused. ....	83
Figure 5-2: Magnification of quarter-wedge shutter highlighting spaces between wedges in the original design. The actual spacing between the wedges is 0.25 $\mu\text{m}$ smaller than the minimum spacing called for by the design rules [14]. ....	84
Figure 5-3: Magnification of sixth-wedge shutter highlighting spaces between wedges in the original design. ....	85



Figure 5-4: Deflection vs. voltage curves for an individual wedge from both the quarter-wedge and sixth-wedge shutters. The smaller deflections for the sixth wedge result from shorter electro-thermal actuators. ....	86
Figure 5-5: Both the drive- and pawl- banked actuators after actuation failure. Both back-bending, or plastic deformation, was observed, as well as breakage of the hot-arms in both cases. ....	87
Figure 5-6: SEM image of the Poly2 shutter flap conforming to the Poly1 layer beneath it. These small conformal dips, while no deeper than 2 $\mu\text{m}$ , prevented the Poly2 shutter flaps from moving. ....	88
Figure 5-7: a) SEM image of one side of an aperture in the Poly1 shutter flap. There is very little Poly2 filling in the hole on this side. b) SEM image of the other side of the same aperture. The Poly2 has filled the hole slightly on this side, preventing the Poly1 shutter flap from moving. In both images, the Poly2 dips between Poly1 flaps have been marked. ....	89
Figure 5-8: a) 100 $\mu\text{m}$ Al shutter prior to actuation. b) Shutter with 0.5 V actuation. Surface burning has already begun. c) Shutter at its maximum, 0.8 V. d) Shutter back-bent after being relaxed back to 0 V. ....	91
Figure 5-9: Optical setup to find $\alpha$ , $\tau$ , and $\rho$ coefficients for PolyMUMPS™ chips. The Jodon spatial filter passes only the TEM <sub>00</sub> mode of the 1.5 mW HeNe laser. The 70 mm convex lens focuses the beam onto a 60% reflective mirror that is designed to measure the reflection from the mounted chips. Radiometer 1 measures both the original flux and the transmittance, while Radiometer 2 measures the reflectance. ....	93
Figure 5-10: Charts illustrating the results of optical testing for five different microshutter arrays. The numbers along the x-axis represent each individual chip tested. ....	94
Figure A-1: Test design of a quarter-wedge, double hot arm shutter. ....	100
Figure A-2: Test design of a sixth-wedge, double hot arm shutter. ....	101
Figure A-3: (left) Iris-style shutter with scratch drive actuation, submitted to PolyMUMPS™ Run 84. (right) Individual wedge of iris-style shutter. ....	102
Figure A-4: Design of a 4x1 array of a flat shutter using SDAs, submitted to PolyMUMPS™ Run 85 for fabrication. ....	103
Figure B-1: Run 83 final design. ....	104
Figure B-2: Run 84 final design. ....	105



## List of Tables

	Page
Table 2-1: PolyMUMPS™ process layer break-down [14]. .....	25
Table 3-1: Colors of MEMS designs and their corresponding PolyMUMPS™ layers. ...	39
Table 4-1: Comparison of Single and Double Hot-Arm Thermal Actuator Devices [16]	60
Table 4-2: Power requirements at 12 V for each wedge shutter. ....	61
Table 4-3: Comparison of coupled actuator devices. ....	67
Table 4-4: CoventorWare® steps and their corresponding input voltages for simulating the gear actuator. ....	70
Table 4-5: Parameters for determining optical absorption for the Poly1 and Poly2 layers. ....	75
Table 4-6: Calculations to determine absorptivity and heat conversion for Poly1 and 2.	76
Table 4-7: Physical parameters for thermal equations [20] .....	78
Table 5-1: Measured values for reflectance, transmittance, and absorptance from five chips from the PolyMUMPS™ process. ....	93

## Acronym List

ACAI	Adaptive Coded Aperture Imaging
AFIT	Air Force Institute of Technology
AFRL	Air Force Research Laboratory
CAI	Coded Aperture Imaging
CVD	Chemical Vapor Deposition
DC	Direct Current
DoD	Department of Defense
DRIE	Deep Reactive Ion Etch
DSP	Digital Signal Processing
FOR	Field-of-Regard
FOV	Field-of-View
FPA	Focal Plane Array
IR	Infrared
LPCVD	Low-Pressure Chemical Vapor Deposition
MEMS	Micro-Electro-Mechanical Systems
MOEMS	Micro-Optical-Electro-Mechanical Systems
MUMPs®	Multi-User MEMS Process
MWIR	Mid-Wave Infrared
PolyMUMPs™	Polysilicon Multi-User MEMS Process
RIE	Reactive Ion Etch
SEM	Scanning Electron Microscope
SNR	Signal-to-Noise Ratio
TEM	Transverse Electric and Magnetic
VDC	Volts Direct Current
VOA	Variable Optical Attenuator

# UTILIZING MICRO-ELECTRO-MECHANICAL SYSTEMS (MEMS) MICRO-SHUTTER DESIGNS FOR ADAPTIVE CODED APERTURE IMAGING (ACAI) TECHNOLOGIES

## 1. Introduction

Cameras have been in use since the 1800s, and were built off a simple principle of exposing film to light through a pinhole, known as the aperture, and at least one lens to focus the images onto the film. While cameras have become more advanced since then, they still follow the same theory of operation: light passes through an aperture and is sent through one or multiple lenses until it is observed by a detector which then processes and transmits the optical information.

Unfortunately, not all wavelengths of light are able to be steered via a lens system. Light at extremely short wavelengths, such as  $\gamma$ -rays and X-rays, are not affected when they are passed through a lens [1]. A new process of imaging these rays was designed nearly forty years ago, and recent strides in technology have allowed this imaging technique to be applied to both visible and infrared (IR) wavelengths.

### 1.1 Coded Aperture Imaging Description

Coded aperture imaging, or CAI, was first conceptualized in 1968 by R.H. Dicke at Princeton University's Palmer Physical Laboratory. He described a multiple pinhole camera for astronomical applications [2]:

*"A pinhole camera for which the entrance area, covered with a very large number of randomly distributed pinholes, is 50 percent open is shown to be a very effective way of forming images of a complex of X-ray stars. A simple statistical trick is used to reduce the multitudinous overlapping images to a single image. Less than forty detected photons are needed to form an image of a single star."*

Since CAI was first exposed to the scientific community, advances in computing technology have allowed it to become more prevalent within imaging devices, particularly in satellites designed to observe X-ray and  $\gamma$ -ray sources [2].

Figure 1-1 illustrates the basic principle of CAI. The two fluxes provide different images onto the detector based on their angle, and these images are summed on the detector. The black photon counts are from Flux 1, and the gray photon counts that are added on top of the black counts are from Flux 2. [3] The image of the separate fluxes is then “coded” on the detector and must be decoded for processing. Adaptive CAI, or ACAI, allows the mask to be fully adjustable to the user’s needs. One can easily see how this system can provide advantages within the imaging community.

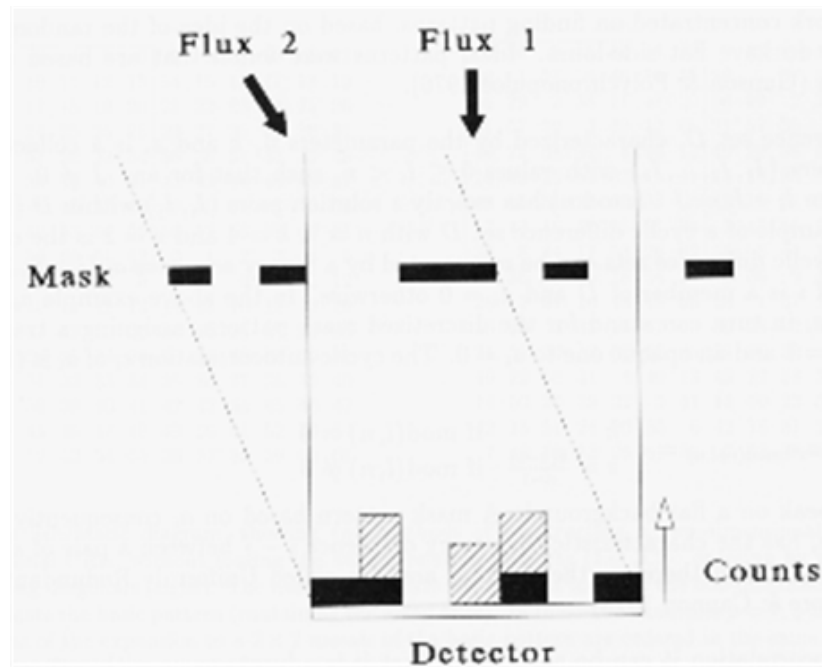


**Figure 1-1:** Basic principle of coded aperture imaging (CAI). [3]

## **1.2 Microshutter Fundamentals**

Microshutters are exactly that—shutters on a small scale. Typically, they range in size from a few microns square to as large as 200  $\mu\text{m}$  by 200  $\mu\text{m}$ . Most commercial cameras use an iris-style shutter, but microshutters are not limited to just this technique. For instance, while an iris-style shutter is efficient when used alone, its efficiency may not be as great when implemented within an array, as it needs both electrical and mechanical stimuli to cause the shutter to close or open. Other styles of microshutters, such as flexible eyelid cantilever shutters, shutter flaps that are able to bend 90 degrees, and moveable covers will be examined for their presence and usefulness both as an individual microshutter and within a microshutter array.

## **1.3 Problem Background**

Adaptive coded aperture imaging (ACAI) is such a new technological concept that only a few microshutter arrays have been designed and fabricated in order to answer the need for adjustable masks. While systems such as the James Webb Space Telescope (JWST) are able to utilize microshutters that flap open and closed vertically, these systems have shown that they require external sweeping sources in order to actuate the microshutters [4]. These external actuators enable the individual shutters to be adjacent to each other, but cause the problem of blocking the entire scene the detector is attempting to observe, thus rendering the entire detector useless for the duration of actuating the shutters.

An ideal microshutter array would require no external actuation; its functionality would depend solely on electrical or magnetic stimuli and generate all movement within

its design. It also would have individual functionality for each shutter within its array, so that its application to ACAI would be fully realized.

#### **1.4 Microshutters Design Proposal**

As this is the first research project of this nature performed at the Air Force Institute of Technology (AFIT), the goal of this effort is first and foremost to design a functioning microshutter array that allows the shutters to be as close as possible to each other. For this effort, an 8 x 8 array of 64 apertures measuring 18 microns x 18 microns spaced 22 microns apart was chosen, as typical small pixels tend to be approximately the same size. The array needs to have as few macroscopic moving parts as possible, and be designed in such a way that each shutter within the array can be individually opened and closed. Optically, the microshutters will be tested in the visible wavelengths; ideally, as much light as possible should be blocked when all the shutters are closed, and as much as 1/64 of the light should be passed when one microshutter is open.

The optical effectiveness of this microshutter array design will be tested and compared with an already fabricated eyelid microshutter design from research sponsored by the Air Force Research Laboratory (AFRL). The overall design should require small voltages in order to perform--ideally on the order of 20 volts or less. Lastly, the design should be as small as possible while still allowing full functionality. It should be noted that while all ACAI systems require digital signal processing (DSP) in order to calculate the image from the signals, developing a functioning DSP system as well as designing and testing a functional microshutter array is out of scope for the time allotted for this research effort.



## 1.5 Summary

This thesis effort will develop individual shutters as well as an array of microshutters using MEMS technology as a prototype for an ACAI mask. The MEMSCAP polysilicon multi-user MEMS process, or PolyMUMPs™, will be used for the fabrication of the individual shutters and the array of microshutters. This process will furnish an affordable means to manufacture MEMS devices with a relatively quick turn-around time, allowing for multiple designs to be fabricated. While the designs explored within this research will be strictly prototypes, it is expected that they will be able to open the door for further similar applications.

In order to fully comprehend how these microshutters work, a thorough background of microshutter and ACAI research will be performed. The fabrication process will be analyzed as well as actuation techniques that can be applied in order to activate the microshutter array. A complete analysis of the design steps will be followed by theoretical modeling to predict how effective the designs are in the physical moving of the shutters. Experimental testing will then show the physical and optical performance of the microshutters and how they compare to the optical results of other physically proven microshutters. This thesis will finish by reviewing how successful the designs are in accomplishing the goals outlined in the previous section. This will then be followed by recommendations for future research in this area.

## **2. Background**

This chapter will explore the basics of adaptive coded aperture imaging (ACAI) and its advantages and disadvantages. Once the fundamentals have been thoroughly explained, applications of microshutters, as well as current research and development efforts, will be listed with each of their methodologies and how they might apply to this research project. Following a thorough examination of these efforts, fabrication techniques will be investigated, particularly the technique chosen for the manufacturing of this project. Next, various MEMS actuation techniques will be examined, including advantages and disadvantages of each and their application to the scope of this research effort. Finally, an introduction to the design concept for this research effort will be given.

### **2.1 ACAI Fundamentals**

Coded aperture imaging (CAI) has been used in both the astronomical and medical communities for years due to its ability to image light at short wavelengths and thus replace conventional lenses. While CAI has its advantages, it also has its limitations. Unfortunately, these CAI systems have fixed masks and can only vary their direction of gaze by moving the entire platform [4]. Because of this, their angular resolution is fixed by the mask separation from the detector plane, the configuration of the detector array, and the mask pattern itself [4]. The basic principle of this imaging process can be seen in Figure 2-1. Also, because the photons from the scene are not brought to a focus, the number of photons seen per detector pixel, known as photon irradiance, is lowered, which then lowers the signal-to-noise ratio (SNR) of the coded image [6]. The SNR determines how well the detector can read the original scene.

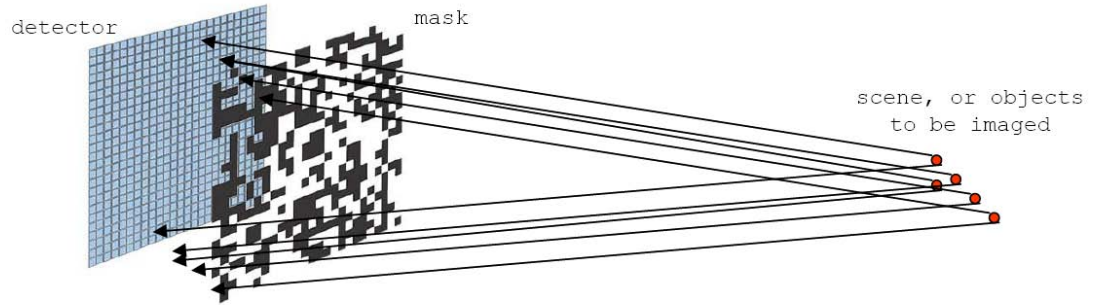


**Figure 2-1:** Illustration of the principle of conventional CAI. Light from every point in a scene within the field-of-view (FOV) casts a shadow of the aperture onto the detector array. The detector then measures the sum of the irradiances it receives, and the image is decoded through deconvolution of the irradiance sums [6].

Where CAI is limited, researchers have discovered that adaptive coded aperture imaging (ACAI) can recover what is lost. Due to the adjustable nature of ACAI, the detector can selectively steer its field-of-regard (FOR) and adjust its FOV, as can be seen in Figure 2-2. It uses a reconfigurable coding mask and digital signal processing to recover the original scene from the detector, as in Figure 2-3.

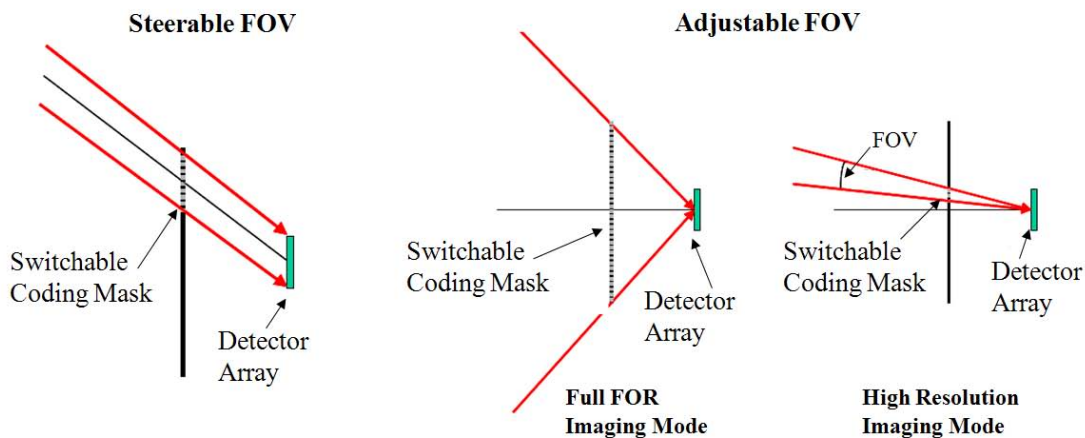


**Figure 2-2:** Different advantages of ACAI without macroscopic moving parts. On the left is a steerable FOR. On the right are two images of adjustable FOV [6].

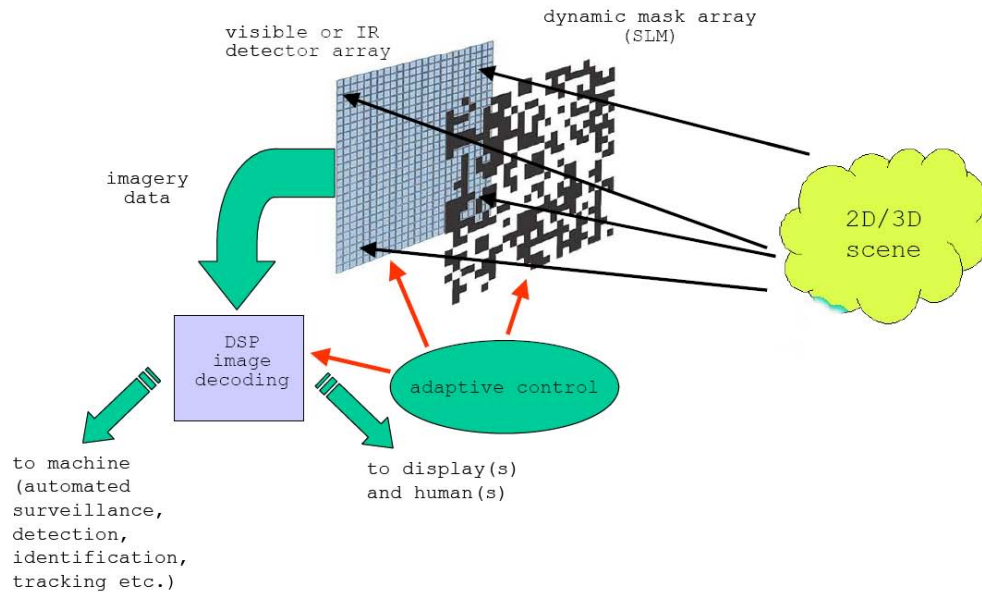


**Figure 2-3:** Illustration of how ACAI works. [6]

Due to the standard size of most detector pixels, one would desire an ACAI mask to be on the order of the same size as the detector array. Nearly all pixels are on the order of microns, leaving detector arrays typically on the order of millimeters or centimeters. In this effort, a prototype of ACAI microshutters will be designed onto a 3 mm x 3 mm square of silicon substrate. All ACAI systems require digital signal processing in order to properly evaluate the scene observed by the detector; however, the time, budget, and materials required to design such a system is out of scope for this research project.

## 2.2 Current Research and Development on Applications of Microshutters

Various efforts throughout the scientific community have explored the uses of microshutters for many applications. These applications include uses as spatial light modulators, variable optical attenuators (VOA), and CAI.

### ***2.2.1 James Webb Space Telescope***

The most common example of microshutters being actively used is the array designed for the James Webb Space Telescope (JWST). The JWST is designed by NASA to study the early stars galaxies of the universe, and is scheduled to launch in 2011. [7] This infrared-optimized telescope contains four 175 by 384 pixel modules of pixel shutters that are 100  $\mu\text{m}$  by 200  $\mu\text{m}$ , as seen in Figures 2-4 through 2-7. [7,4] Due to the harsh space environment to which these microshutters will be subjected, the array must be held to stringent design requirements. Among these requirements are the 7000:1 contrast ratio [8], the 37 K operating temperature [7], individual actuation [4], and stiction from electrostatic latching [9]. To target the individual shutters for actuation, all the shutters are opened electromagnetically; this is then followed by an electromagnetic scan to close all but the desired shutters. [8] Should a particular shutter need to be held open for days at a time, or “latched”, the shutter will receive a 40V charge. [9] This charge can be inadvertently stored in the shutter’s dielectric core, causing the shutter to stick to the substrate, also known as stiction. [9] This was overcome by a brief reverse in polarity of the charge, but demonstrates the multitude of problems these shutters can undergo. [9]

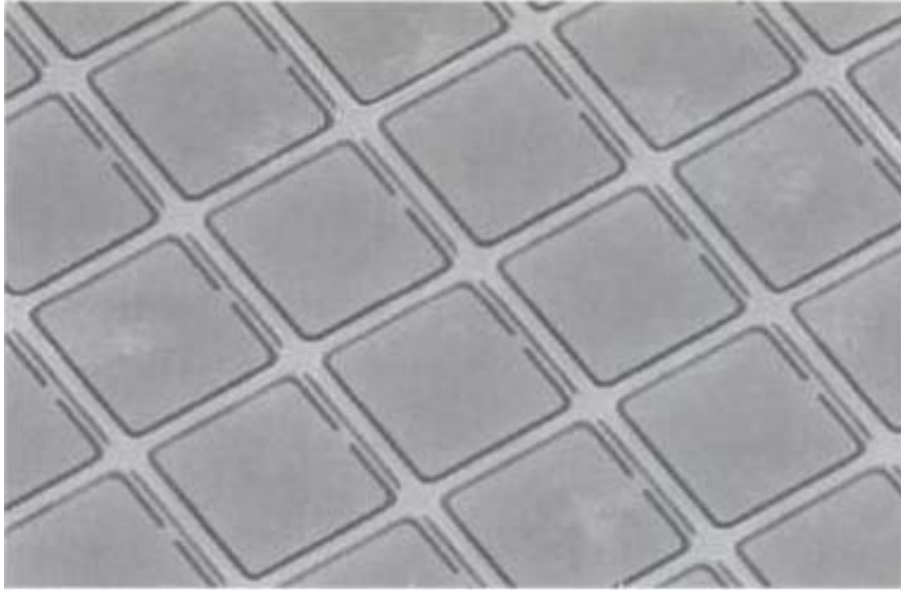


**Figure 2-4:** Array of microshutters on the JWST. [7]

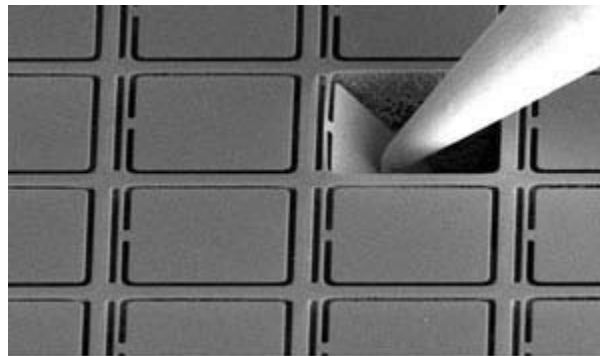


**Figure 2-5:** Individual JWST shutter being activated by a probe. [4]

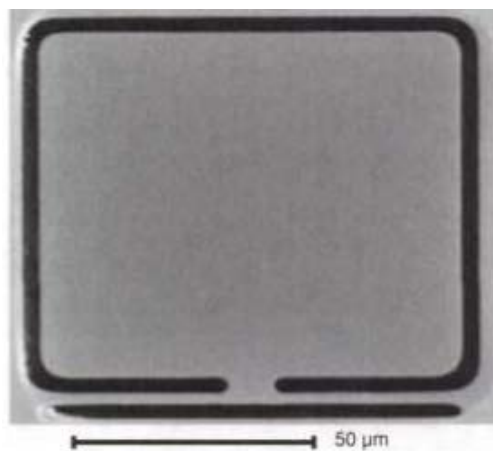


**Figure 2-6:** SEM picture of a single JWST shutter. [7]

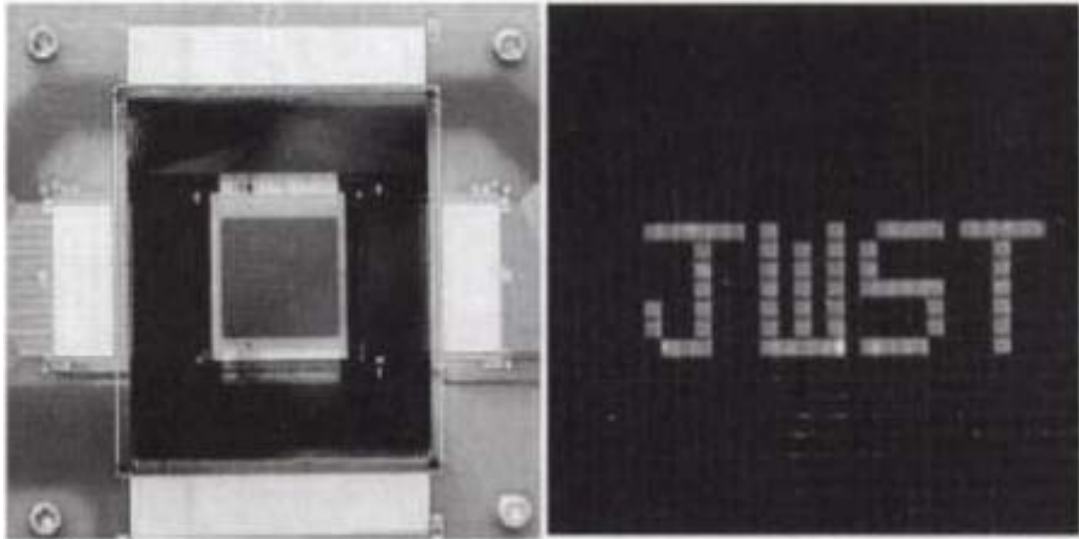


**Figure 2-7:** (left) Fully functional 128 by 64 pixel model of the JWST array. (right) Demo of model array displaying JWST acronym. [7]

### *2.2.2 Adaptive Coded Aperture Imaging*

ACAI research is very recent, with the vast majority of research published in 2007 and 2008. Nearly all of this research experiments with different types of microshutter systems in order to create the ACAI mask. These systems can vary in technique, size, materials, and function.

At the Air Force Research Laboratory (AFRL), scientists are researching various methods of fabricating “eyelid” microshutters for the purpose of serving as an ACAI mask. Eyelid microshutters are built of at least one flexible material, are able to conduct electricity, and also have an internal stress that causes them to curl up and away from the substrate and aperture, as seen in the left image of Figure 2-8.

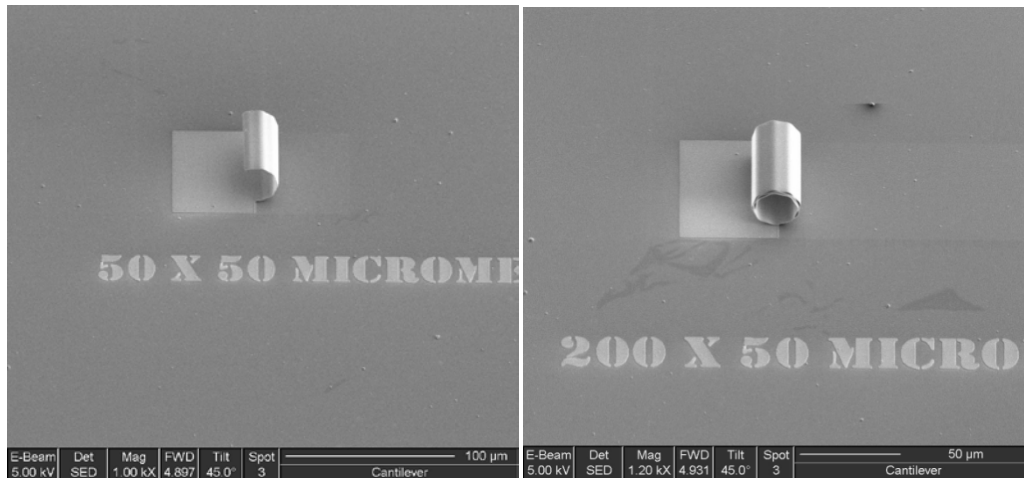


**Figure 2-8: (left)** Scanning Electron Microscope (SEM) image of a single eyelid microshutter 50  $\mu$ m long and 50  $\mu$ m wide. This eyelid was manufactured with ridges etched along the width of the microshutter to encourage uniformed curling. **(right)** SEM image of an eyelid shutter 200  $\mu$ m long and 50  $\mu$ m wide. Note the difference in the curl between the two eyelids [10].

The eyelid microshutters used for this study at AFRL were fabricated in-house of titanium and gold. The disparities in the Young's Modulus value, as well as the coefficient of thermal expansion between titanium and gold, cause the eyelids to curl so profoundly. The right image of Figure 2-8 shows how profound the curling is within these eyelids as the length increases [10]. For these eyelids, the substrate is held at ground, a dielectric layer provides electrical insulation between ground and the eyelids, and the eyelids are fabricated on the dielectric layer. When a voltage is passed through the contact pad, electrostatic forces cause the eyelid to uncurl and "close" the aperture. Since these eyelids were fabricated on a quartz wafer, the apertures are merely arbitrary as the entire wafer passes visible and IR light waves [10].

Some limitations of these eyelid shutters include nonuniformity in curling and difficulties in closing the shutters. While the eyelids were designed to be closed with a voltage less than 10 V, voltages up to 100 V were tested, and the eyelids could not be



pulled down to the substrate [10]. Nonuniformity in curling, seen in Figure 2-9, also highlighted some of the issues in realizing these eyelids as a viable ACAI mask.

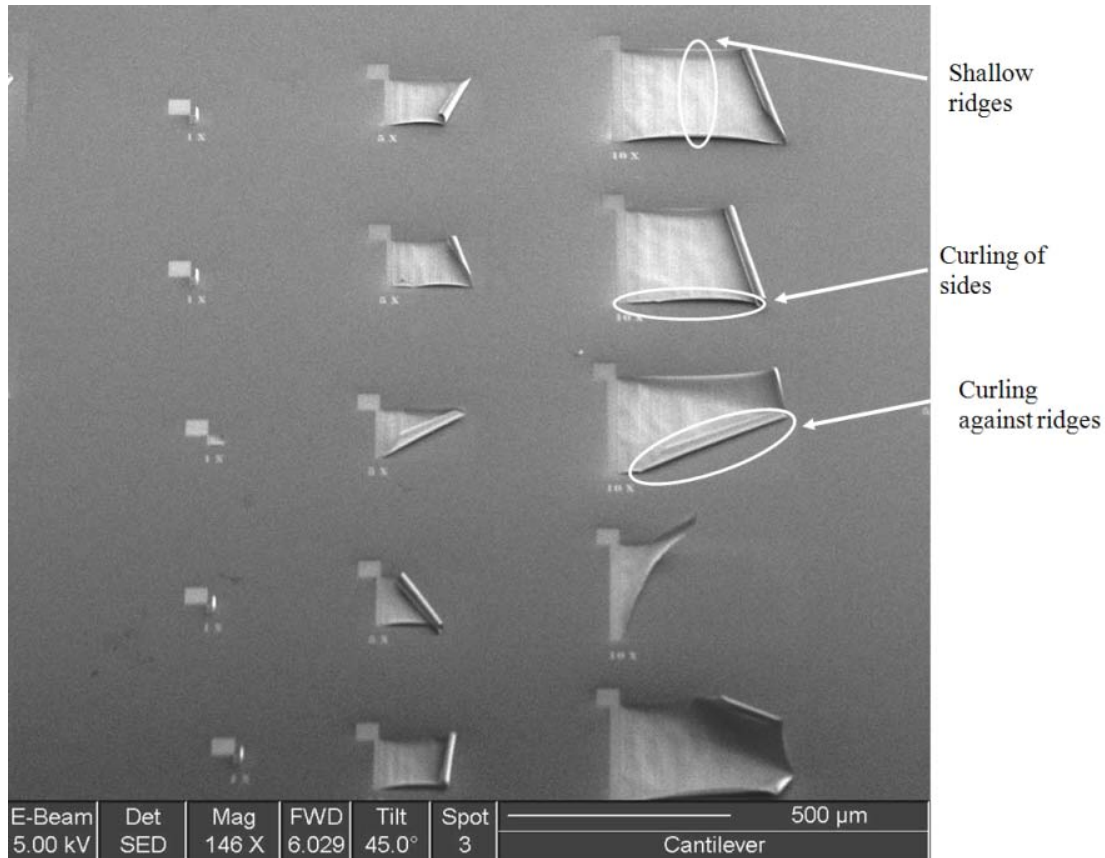


**Figure 2-9:** SEM image of failed curling of eyelids. [10]

Another group of scientists utilized the eyelid microshutter concept in addition to micro-prisms and micro-piston arrays to achieve a functional ACAI mask. This research layered small prism lens on pistons to allow the system to look in a certain direction. Figure 2-10 illustrates this concept. By closing the shutters over all apertures designed to look at directions 2, 3, and 4, the focal plane array, or FPA, can look solely in direction 1

to decode a scene [11]. On the other hand, if all the eyelids are open, then the detector can image in all four directions.

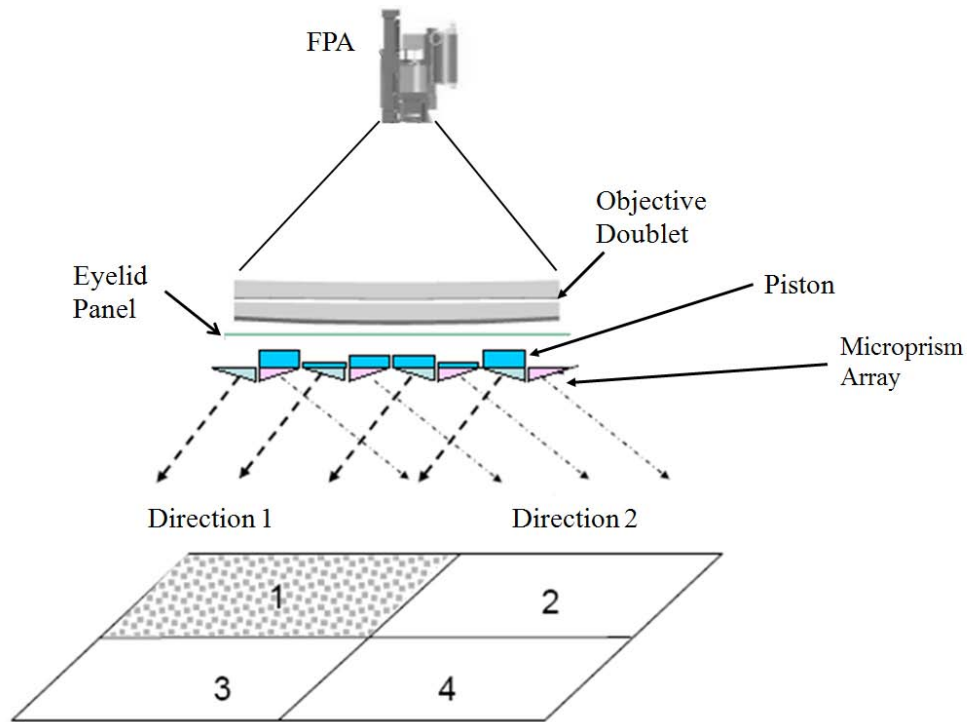


**Figure 2-10:** Combination of eyelid microshutter panel with microprisms and micropistons. The shutters are designed to limit look direction, the prisms provide the look direction, and the pistons allow the prisms to move vertically to provide a clear line-of-sight to the scene being imaged, as well as providing the necessary phase corrections for each look direction. [11]

As with the eyelids in the previous effort, manufacturing a uniform array of eyelid microshutters is not trivial, though the uniformity in this effort was vastly improved. In addition, the purpose of growing ACAI technologies is to replace conventional lensing systems with a coded aperture mask; by introducing lensing prisms and pistons, this study begins to stray from the original goal of ACAI research.

Another AFRL research effort takes a different approach to microshuttering for ACAI. Instead of designing a microshutter array to physically open and close apertures,

these engineers have utilized the optical properties of polysilicon in the mid-wave-infrared (MWIR) range to create Fabry-Perot interferometers that will either reflect or transmit light waves depending on their thickness. When a Fabry-Perot interferometer's thickness is a multiple of the wavelength being passed to it, it transmits the maximum amount of light. However, if the width of the interferometer is not a multiple of  $\lambda$ , or wavelength, then the phase difference of the passed light will cause destructive interference and a minimum signal. [1] These micro-interferometers are constructed of simple electrostatic actuators, and the details of these types of actuators will be explored in a later section.

Figure 2-11 shows a cross-section of these interferometers. Note that connections to the substrate are not included in this illustration. As the moveable mirror experiences voltage (typically less than 20V), the gap width shortens, causing the interferometer to adjust its peak transmission wavelength. This wavelength can be explained by

$$\delta = \left( \frac{2\pi}{\lambda} \right) 2nd \cos \theta \quad (2.1)$$

where  $\delta$  is the phase difference in the transmitted wavelengths,  $\lambda$  is the wavelength of light entering the interferometer,  $n$  is the index of refraction of the medium inside the interferometer,  $d$  is the width of the gap, and  $\theta$  is the angle of the entering light as compared to normal [1].

One advantage of this technique is the ability to design microshutters close to each other. The research at AFRL successfully developed a line-drivable array for just this purpose and was able to implement this design into a 3 x 3 array, shown in Figure 2-12. The line-drivable array is shown through wiring the rows separate from the

columns, and this technique will be utilized for the designs developed through this effort. While this microshutter array proves quite useful in the MWIR range, it falls short of ideal in that it cannot pass light in the visible range [5].

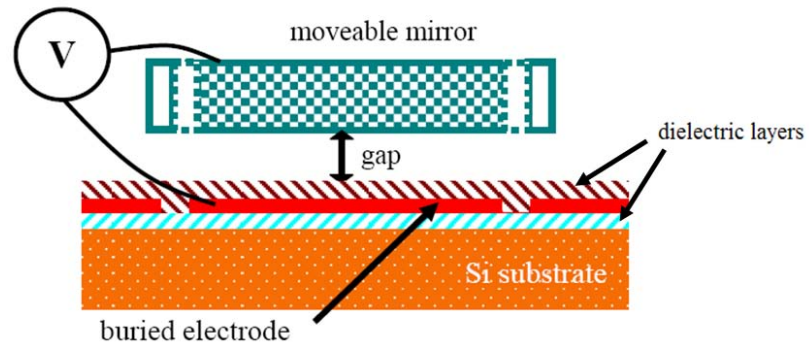


**Figure 2-11:** Fabry-Perot interferometer microshutter design for MWIR. As a voltage is passed to the moveable mirror, the gap begins to decrease, which then affects which wavelengths will be passed to the buried electrode. [5]

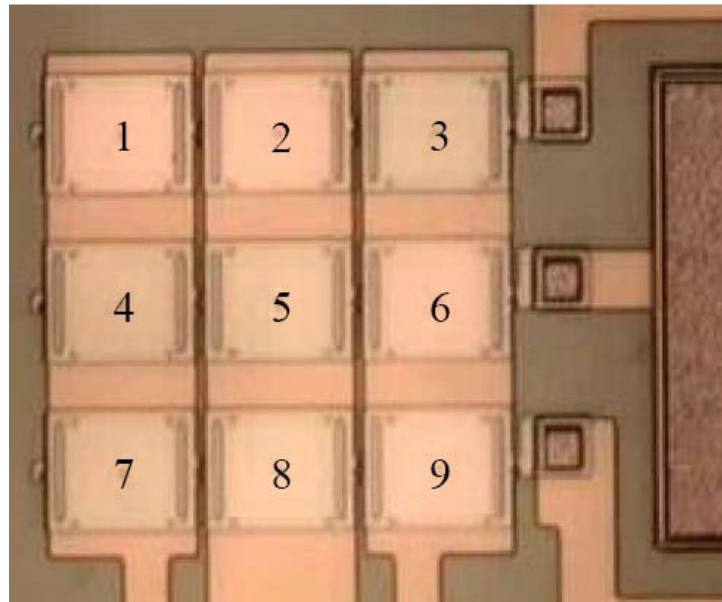


**Figure 2-12:** Microscope image of 3 x 3 Fabry-Perot microshutter array. The wiring via rows and columns allows each microshutter to be individually driven, as they only respond to signals in both electrodes. [5]

### 2.2.3 Others

One purpose for these microshutter arrays is to serve as a spatial light modulator or variable optical attenuator (VOA). While spatial light modulators are normally based off of micromirror arrays for their use in image projectors and displays, high intensities of light and fast switching indicate that microshutter arrays could be beneficial in improving the performance of these modulators. [12] Ravnkilde et al. designed a microshutter from micromachined and electroplated nickel for just this purpose, as seen in Figure 2-13. [12] Their microshutter was a 35- $\mu\text{m}$  diameter nickel disk on a 300- $\mu\text{m}$  long actuation beam that moved the shutter from side to side, covering and uncovering an aperture underneath. This microshutter array was very resilient and functioned normally after  $10^8$  cycles. [12] While the shutter array was functional, the massive amount of actuation schemes do not allow for individual pixel shuttering.

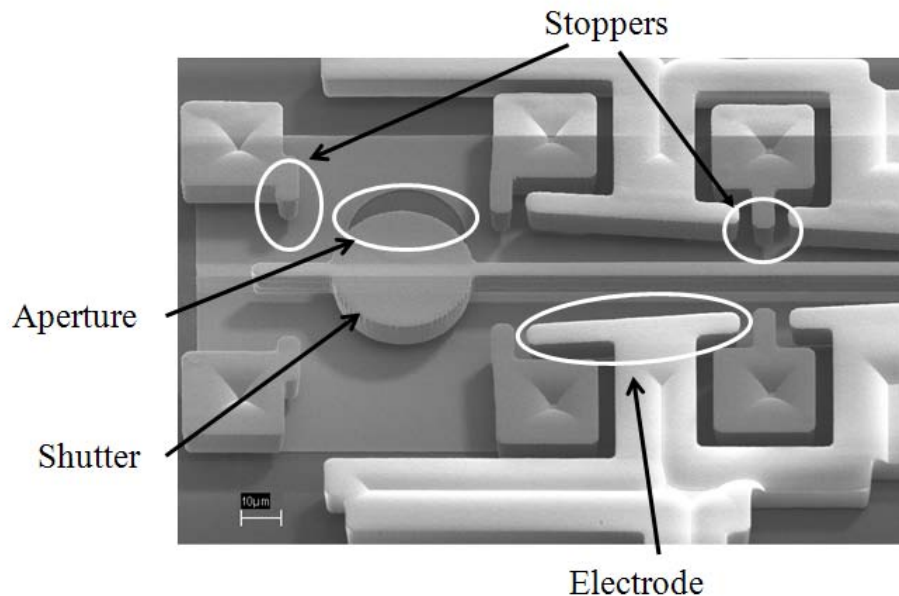


**Figure 2-13:** SEM picture of an individual VOA shutter. [12]

Another use for a microshutter is within a VOA. VOAs are used in fiber-optic circuits by regulating the intensity of light that is transmitted between two fibers, and are extremely useful in the growing optical telecommunications field. [13] MEMS VOAs function by having a shutter inserted into the optical signal path to stop down the optical signal as needed. Zawadzka et al. designed a successful shutter by using the foundry PolyMUMPs™ process offered by MEMSCAP. This process uses three polysilicon layers of varying thicknesses to fabricate devices, of which two are releasable. In order to effectively stop down the intensity, the shutter contained etch holes that would be moved back and forth between the fibers; when everything was perfectly aligned, the shutter would either pass light or reject it. [13] This can be seen in Figure 2-14. The shutter used six scratch drive actuators to shift the shutter between the fibers, as can be seen in Figure 2-15.

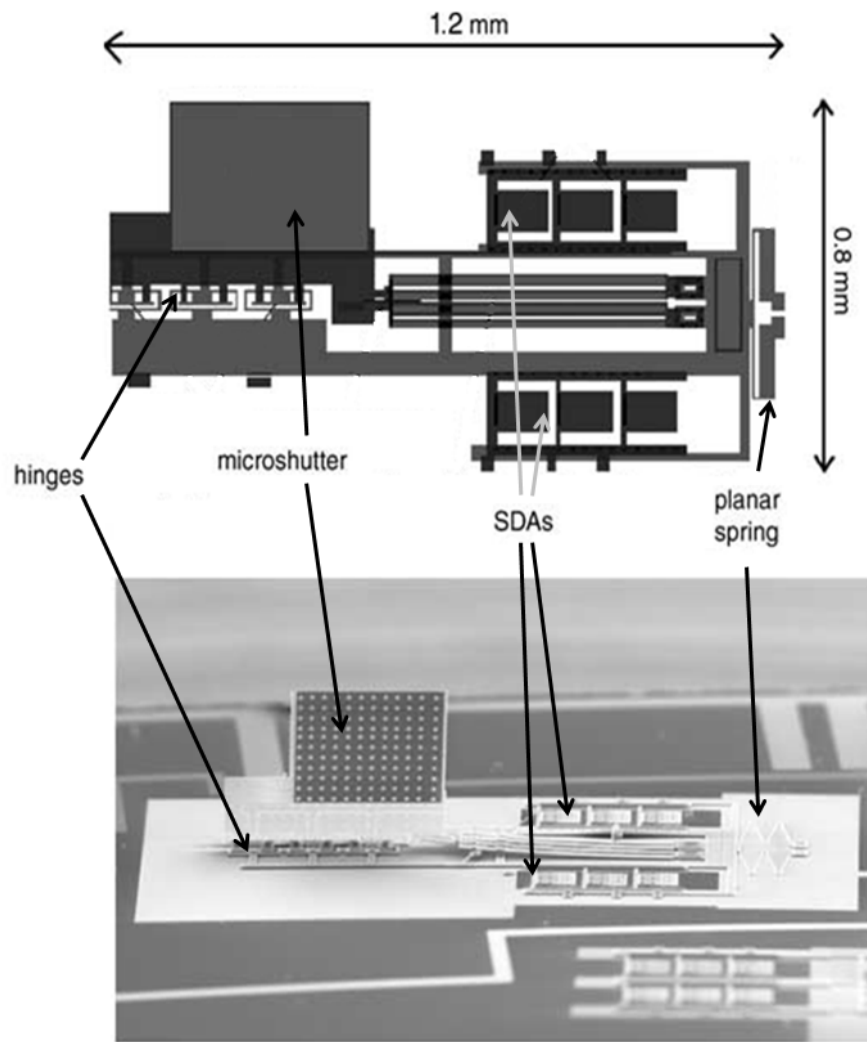


**Figure 2-14:** (top) Mask layout for VOA shutter. (bottom) SEM picture of self-assembled VOA microshutter. [13]

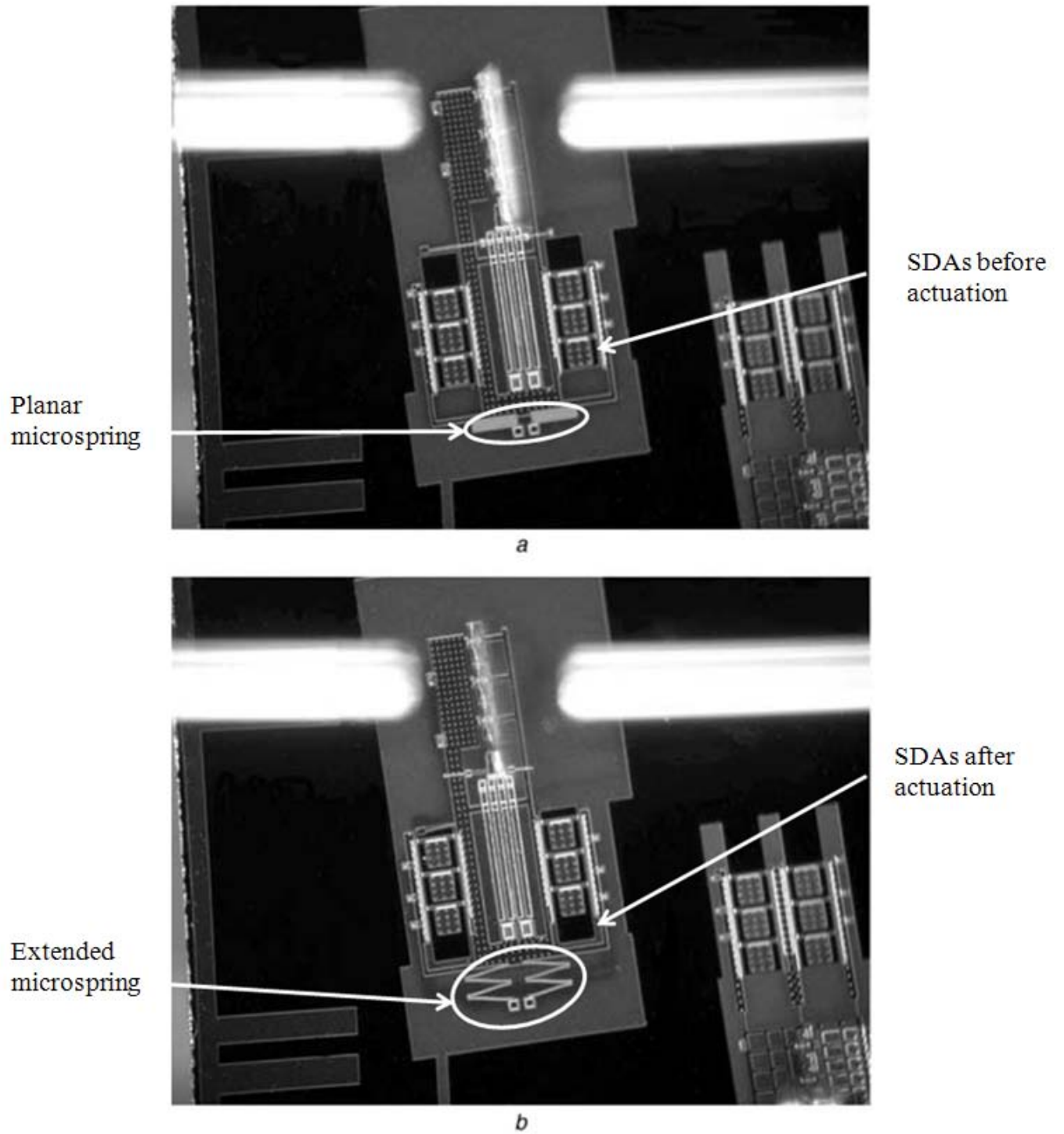


**Figure 2-15:** (a) VOA microshutter before actuation. (b) VOA microshutter after actuation. Note the extended microsprings and the location of the scratch drive actuators. [13]



While the VOA shutter is effective at stopping down an optical signal, it does not prove useful if an array of microshutters is needed. Motohara et al. designed a microshutter that lends itself well to an array design. [8] The shutters are rectangular blades with dimensions of  $100\text{ }\mu\text{m} \times 1000\text{ }\mu\text{m}$  and actuate either electrostatically or electromagnetically into an aperture fabricated within the substrate, as seen in Figure 2-16; pictures of the functioning microshutters can be seen in Figure 2-17.

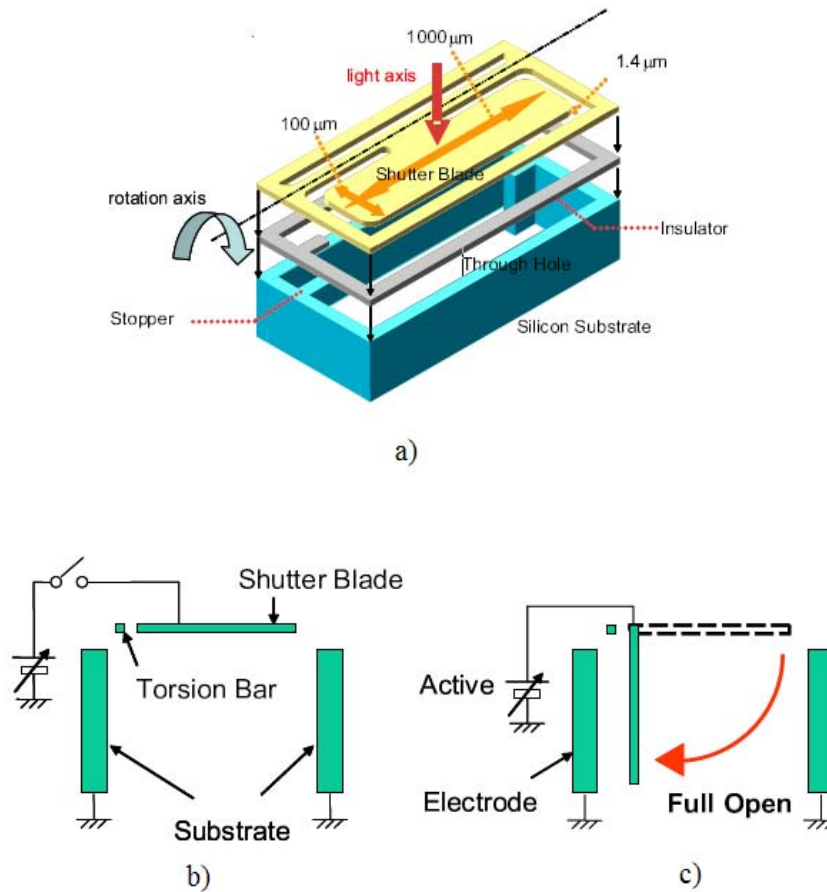


**Figure 2-16:** a) 3D cross-section of an individual shutter-blade. b) Cross-sectional actuation of shutter-blade in closed position. c) Shutter-blade in open position. [8]

The shape and fabrication of these shutter-blade actuators is highly conducive to fabrication and function within an array. Unfortunately, there are limits with the functionality of these shutters. The current shutter design has a fill factor of over 80%, but with that comes a contrast ratio of 2000:1 and a required drive voltage of over 100V [8]. The drive voltage is worrisome, in that if one were to deploy this array as a self-standing unit, ease and transport of a power supply would have to be taken into account.

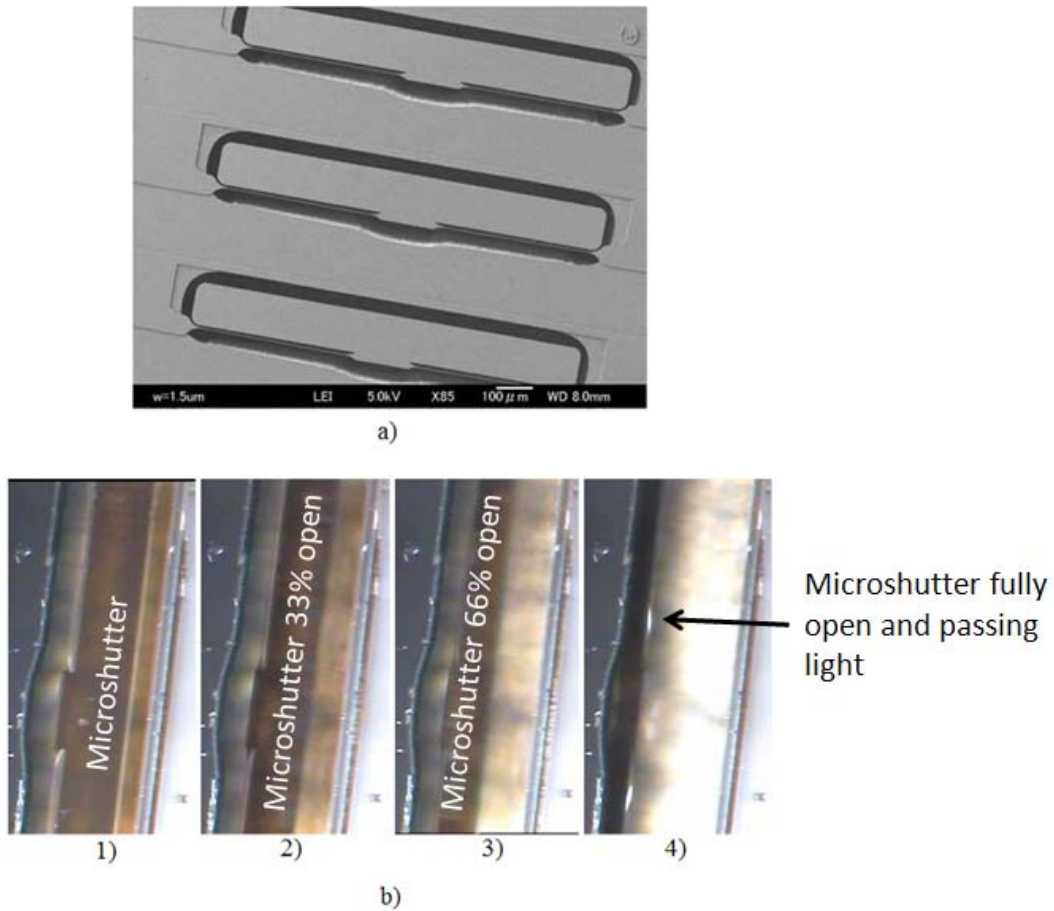


**Figure 2-17:** a) Array of shutter-blades. b) Photo of a shutter-blade moving from fully closed (1) to fully open (4). [8]

### 2.3 MEMS Fabrication Process

In order to understand exactly how these microshutters will perform, one must understand the various types of MEMS fabrication. In short, there are three different categories for MEMS fabrication: bulk micromachining, surface micromachining, and micromolding. Bulk micromachining is a subtractive process; it involves selective etching of a substrate (usually silicon) to create devices. Surface micromachining involves chemical vapor deposition (CVD) of alternating thin layers of patterned materials to create devices. These devices typically range from two to five microns in height, and thus are difficult to use for 3-D structures; however, the simplicity of sequential deposition usually allows for more inexpensive fabrication costs. Micromolding uses high-aspect ratios and deep etching processes to create devices of up to hundreds of microns in height. Because of this height, the devices are usually more robust; but the high-aspect processes are much more expensive than those found in surface or bulk micromachining processes.

Because the budget and time for a thesis research project is limited, the Multi-User MEMS Process, or MUMPs<sup>®</sup>, was selected for this effort. Specifically, the polysilicon deposition MUMPs<sup>®</sup>, or PolyMUMPs<sup>™</sup> process will be used for the designs that are fabricated in this thesis. PolyMUMPs<sup>™</sup> is a three-layer polysilicon surface micromachining process that utilizes two sacrificial layers of silicon dioxide to provide separation between the three polysilicon mechanical layers, shown in Figure 2-18 [14].

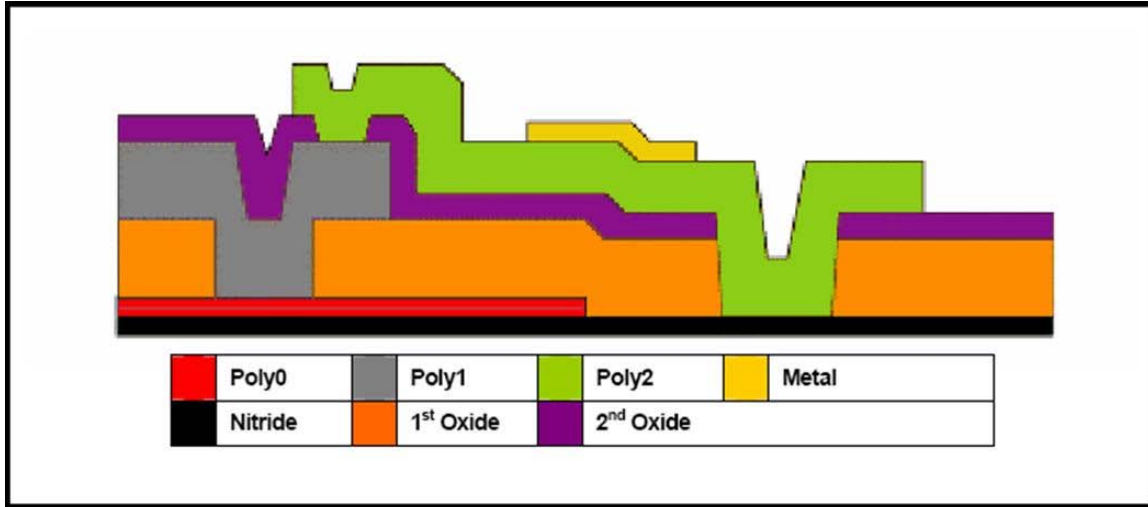


**Figure 2-18:** Cross sectional view of all seven layers of the PolyMUMPs™ process (not to scale). The two oxide layers are sacrificial layers, and the nitride, or isolation layer, is the surface which provides the foundation for the device; it is grown on a (100) silicon wafer [14].

The process starts with a (100) n-type doped silicon wafer. First, a 0.6- $\mu\text{m}$  layer of silicon nitride is deposited on the surface of the wafer using a low-pressure chemical vapor deposition (LPCVD) process to provide electrical isolation. This is followed by a 0.5- $\mu\text{m}$  layer of polysilicon, termed Poly0, which is deposited using LPCVD and patterned using standard photolithography processes. A 2.0- $\mu\text{m}$  silicon dioxide layer, called 1<sup>st</sup> Oxide, is the next layer added via LPCVD; this is then annealed at 1050°C for an hour. This annealing both dopes the polysilicon and reduces the residual film stress. After etching anchor points for the first releasable layer, the wafer is patterned with a 2.0- $\mu\text{m}$  polysilicon layer; this layer is called Poly1. A second oxide layer, 0.75- $\mu\text{m}$  thick, is then deposited, patterned, and annealed. Anchor points are once again etched, followed by a 1.5- $\mu\text{m}$  thick Poly2 layer deposition. Lastly, a 0.5- $\mu\text{m}$  gold layer, labeled as Metal, is deposited and patterned by using a lift-off process; this layer provides electrical

connections for probing, bonding, and electrical routing, and can be used as a highly reflective layer for optical mirror applications [14]. A summary of the layer thicknesses and their description can be found in Table 2-1 below.

**Table 2-1:** PolyMUMPs™ process layer break-down [14].

Material Layer	Layer Thickness	Layer Description
Nitride	0.6 $\mu\text{m}$	Provide electrical isolation from wafer
Poly0	0.5 $\mu\text{m}$	Electrical layer for ground plane/electrode formation.
1st Oxide	2.0 $\mu\text{m}$	First sacrificial layer providing gap between Poly0 and Poly1 layers.
Poly1	2.0 $\mu\text{m}$	First mechanical layer
2nd Oxide	0.75 $\mu\text{m}$	Second sacrificial layer providing gap between Poly1 and Poly2.
Poly2	1.5 $\mu\text{m}$	Second mechanical layer
Metal	0.5 $\mu\text{m}$	Electrical contact layer or optically reflective surface

## 2.4 MEMS Actuation Techniques

In order for any of the above research designs to function, they must use an actuation scheme that converts an input energy into a mechanical motion. An actuator is defined as a device that converts energy from one form, such as electrical or thermal energy, into another form, such as mechanical energy [15]. Actuators are designed to be as efficient as possible, but energy losses naturally will be incurred and must be expected. Due to the size and scale of most MEMS devices, certain effects like thermal conduction must be taken into account, while other forces, such as gravity, are negligible and thus

can be ignored. In this section, common MEMS actuation techniques will be explored and examined for their advantages and disadvantages in relation to this research effort.

#### ***2.4.1 Electrostatic Actuation***

Electrostatic actuation is a common actuation technique within MEMS technology, and is typically used as a switching drive to pull in an electrical contact [16]. It uses Coulomb attractive forces of separated charges to overcome mechanical restorative forces of the structure in which it is being applied [15]. Figure 2-19 shows a simple parallel plate capacitor and the forces acting upon it. The restoring force,  $F_r$ , is a function of the axial spring constant,  $k_z$ , which is dependent on structural geometries and material properties of the device. The electrostatic force,  $F_e$ , is a function of the applied voltage,  $V$ , the surface area of the plate,  $A$ , the permittivity of the dielectric between the plates (in this case air),  $\epsilon_o$ , and the distance between the plates, represented as  $z_o$  [16]. The applied voltage causes electrons to collect on the bottom plate, and positive charge to collect on the top plate. When the charges are separated like this, an electrostatic force is created. When the plates are in equilibrium, the electrostatic force is balanced by the restoring force. If the voltage is driven high enough, the electrostatic force will overcome the restoring force, causing the plates to “snap in” and close the gap between them [16].

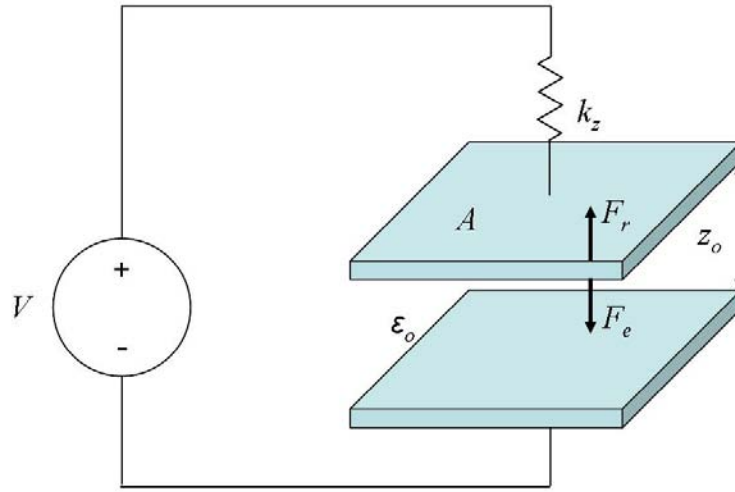


**Figure 2-19:** Force diagram for a parallel plate electrostatic actuation device [16].

Electrostatic actuators prove useful in their simplicity and dependable responses. In most cases, once the potential across the device is removed, the electrostatic force rapidly drops to zero, allowing the restoring force to return the device to its starting position [15]. Unfortunately, these devices typically require high voltages due to device designs for the electrostatic force to overcome the restoring force, particularly when the physical displacement is on the order of microns. Coulomb's Law is given by

$$F_e = k_e \frac{Q_1 Q_2}{d^2} \quad (2.2)$$

where  $F_e$  is the electrostatic force,  $k_e$  is Coulomb's constant,  $Q_1$  and  $Q_2$  are the two charges being measured, and  $d$  is the distance between them. The charge difference between the two plates is measured as

$$Q = CV \quad (2.3)$$

where  $Q$  is the charge,  $C$  represents the capacitance, and  $V$  is the potential difference between the two plates. The capacitance for the actuator shown in Figure 2-19 is given by

$$C = \frac{\epsilon_0 A}{d} \quad (2.4)$$

where  $\epsilon_0$  is the dielectric permittivity of free space,  $A$  is the surface area of the electrode plate, and  $d$  is the distance between the two plates. The capacitance is inversely proportional to the distance separating the plates, so as the distance increases, the capacitance decreases. Because the charge difference is directly proportional to the capacitance, it will decrease as well. As Equations 2.3 and 2.4 are substituted back into Equation 2.2, Coulomb's law can be rewritten as

$$F_e = k_e \frac{\epsilon_0^2 A^2 V^2}{d^4} \quad (2.5)$$

showing that as the distance between the two plates is increased, the voltage will need to be drastically increased in order to provide the same electrostatic force. Due to the magnitudes of the Coulomb constant and the permittivity of free space, distances on the order of microns will only generate very small forces despite requiring higher voltages. Because of this, the number of mechanisms that can use this type of actuation for physical movement are limited [15].

#### ***2.4.2 Electro-thermal Actuation***

Electro-thermal actuators function due to the thermal properties of materials in the MEMS devices. When current passes through a conductor, the conductor generally heats up due to the thermal losses in the conductor. This is called Joule heating [16]. This



Joule heating then causes the conductor to expand in length. While this expansion is typically negligible on a macro scale, Joule heating within MEMS devices causes expansion to be much more significant as a result of their size. Figure 2-20 shows this elongation effect of a MEMS beam and can be described by

$$L_{new} = L_0 + \alpha_L [L_0 (T_{avg} - T_0)] \quad (2.6)$$

where  $L_{new}$  is the new beam length;  $L_0$  is the initial beam length;  $\alpha_L$  is the coefficient of linear thermal expansion;  $T_0$  is the initial temperature before current flow; and  $T_{avg}$  is the average final temperature of the beam [15]. This change in beam length can then be used to create physical displacements in MEMS devices in various ways. One type of electro-thermal actuator often used is the bi-morph configuration; this device uses the difference in thermal expansion between two different materials to create a deflection [16]. While the PolyMUMPs™ process uses both polysilicon and gold for its mechanical layers, the bi-morph actuation provided from these materials do not apply to this thesis and will not be studied further.

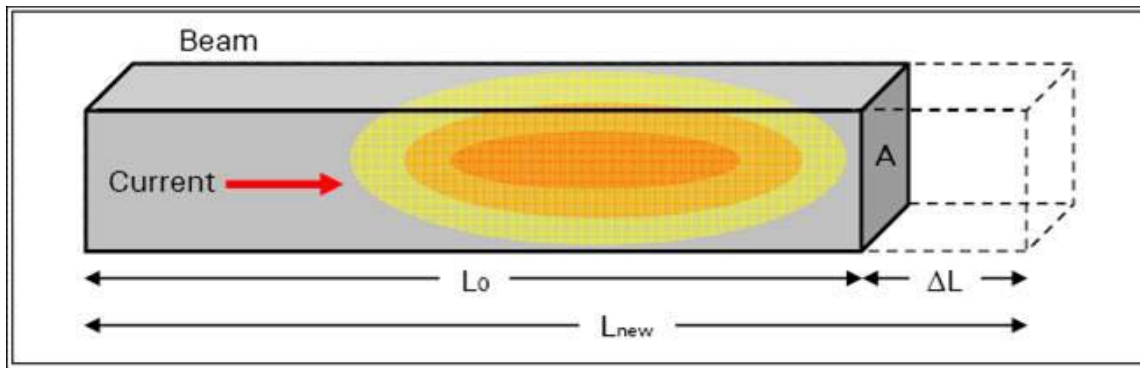


**Figure 2-20:** MEMS electro-thermal technique illustrating beam elongation due to Joule heating caused by current flow through the conductor material.  $L_0$  is the initial beam length;  $L_{new}$  is the new total length of the beam after thermal expansion;  $A$  is the cross-sectional area of the beam; and  $\Delta L$  is the change in beam length [15].

To make a thermal actuator using only one material such as polysilicon, one can vary the cross-sectional areas of the beams. The larger the area, the more easily heat is dispersed, so that beams with a small cross-sectional area will be much hotter than those with a large cross-sectional area when the same current is passed through both beams. Because the thinner beam, or hot-arm, has a much higher temperature, it will undergo a longer expansion than that of the thicker beam, or cold-arm. Figure 2-21 shows that if these two beams are connected, the thermal expansion of the hot-arm will cause the entire beam assembly to move laterally. This beam assembly is the electro-thermal actuator. Figure 2-22 illustrates how current flow through these devices causes deflection. One of the primary advantages of these devices is that significant displacements of between 10 to 15  $\mu\text{m}$  can be achieved using voltages of less than 20 volts [15]. In addition to the excellent displacement-to-voltage ratio achieved using these devices, significant force can also be applied by these devices, usually from 10 to 100  $\mu\text{N}$  [16].

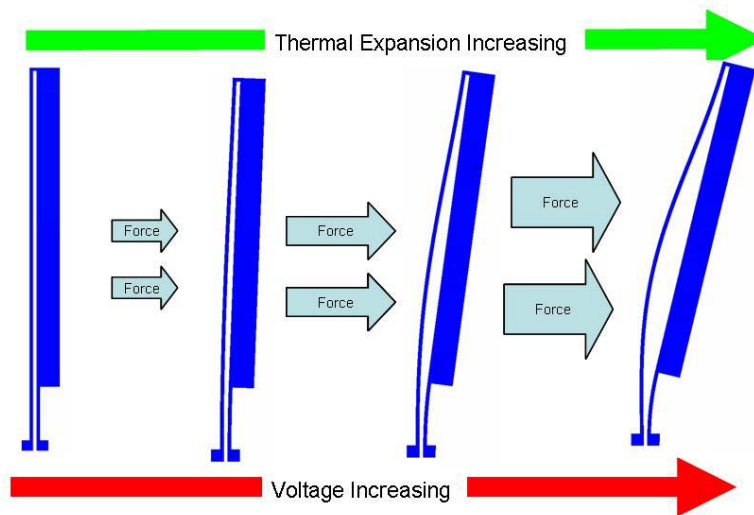
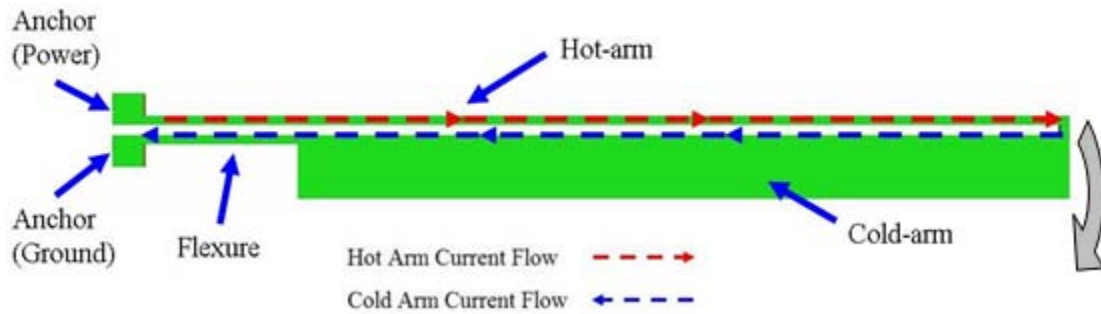
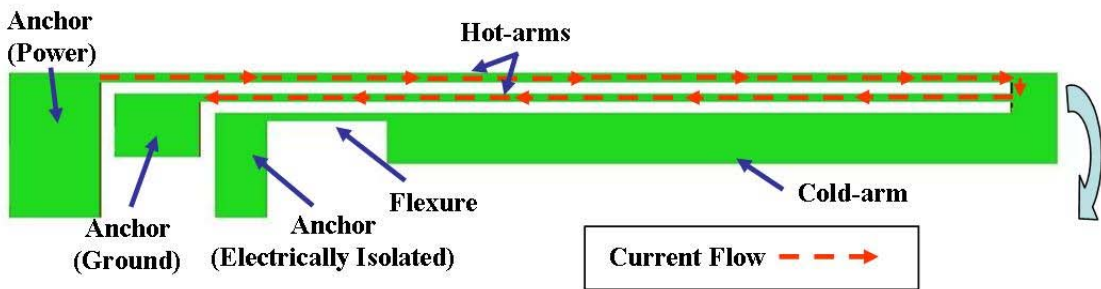


**Figure 2-21:** Single hot-arm electro-thermal actuator showing increasing force and displacement with increasing applied voltage [16].



a)



b)

**Figure 2-22:** a) Diagram of current flowing through a single hot-arm thermal actuator. b) Diagram of current flowing through a double hot-arm thermal actuator. [16]

While electro-thermal actuators are quite efficient at converting low voltages into lateral displacements, they typically have slower response times due to the time needed for the material to heat up for expansion and then cool down to return to neutral. When the voltage is removed, this cooling must be via thermal conduction or convection [15]. Another limitation results from deformations these devices undergo when pushed to their maximum voltage capability or beyond. These deformations can cause the hot-arm to be

permanently plastically deformed, so that when the voltage is removed, the actuator comes to rest slightly past its original position. This condition is known as back-bending, and while it can be useful for certain designs, it almost always ensures that the lateral motion will not be as effective as a normal thermal actuator.

#### ***2.4.3 Scratch Drive Actuators***

Scratch drive actuators, or SDAs, utilize the stiction properties of polysilicon to create movement within MEMS devices. They also have many advantages over other types of MEMS actuation techniques. Due to the nature of their actuation, they move in a linear direction, as opposed to the curved motion of the thermal actuator. This linear motion can then be used to drive various MEMS mechanisms, including those involved with microshutters.

SDAs consist of four main components: the substrate on which they function, the insulator, the bushing, and the plate, as seen in Figure 2-23. When a voltage is applied between the plate and the substrate, a virtual capacitor is created, and the plate experiences an electrostatic force that pulls it down towards the substrate [17]. As the plate pulls down, it warps and causes the bushing to tilt, which then causes the bushing to push forward along the insulator [18]. When the voltage is removed, both the plate and bushing return to their previous position, but have been inched forward a small distance. Figure 2-24 illustrates the vertical and lateral motions of an SDA as well as the periodic voltage needed for each step. A periodic voltage is necessary to actuate an SDA; this voltage can be tuned so that the appropriate waveform and frequency translate into the necessary velocity and step size for the SDA's movement [17].

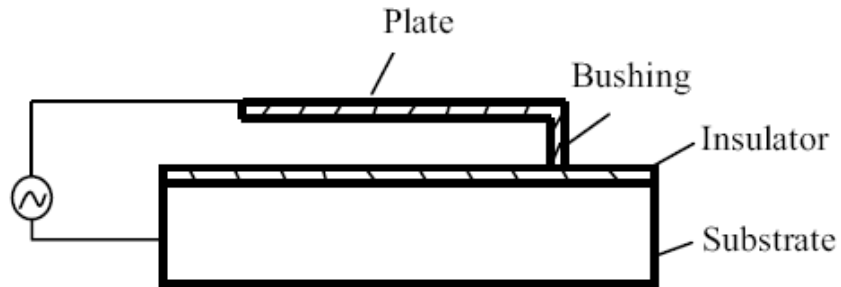


**Figure 2-23:** Side view of a scratch drive actuator showing the four main components and where the voltage is applied [17].

SDAs can prove to be quite useful, but they do not provide much displacement given an applied force. Researchers at the University of Strathclyde showed that given SDAs fabricated with the PolyMUMPs™ process, an SDA would require 250  $\mu\text{N}$  of force to move just 5  $\mu\text{m}$ ; it would require 550  $\mu\text{N}$  of force for a maximum displacement of 10  $\mu\text{m}$  [18]. Some designs within this effort will attempt to use scratch drive actuation as a proof-of-concept, but the SDA's usefulness within this research is limited.

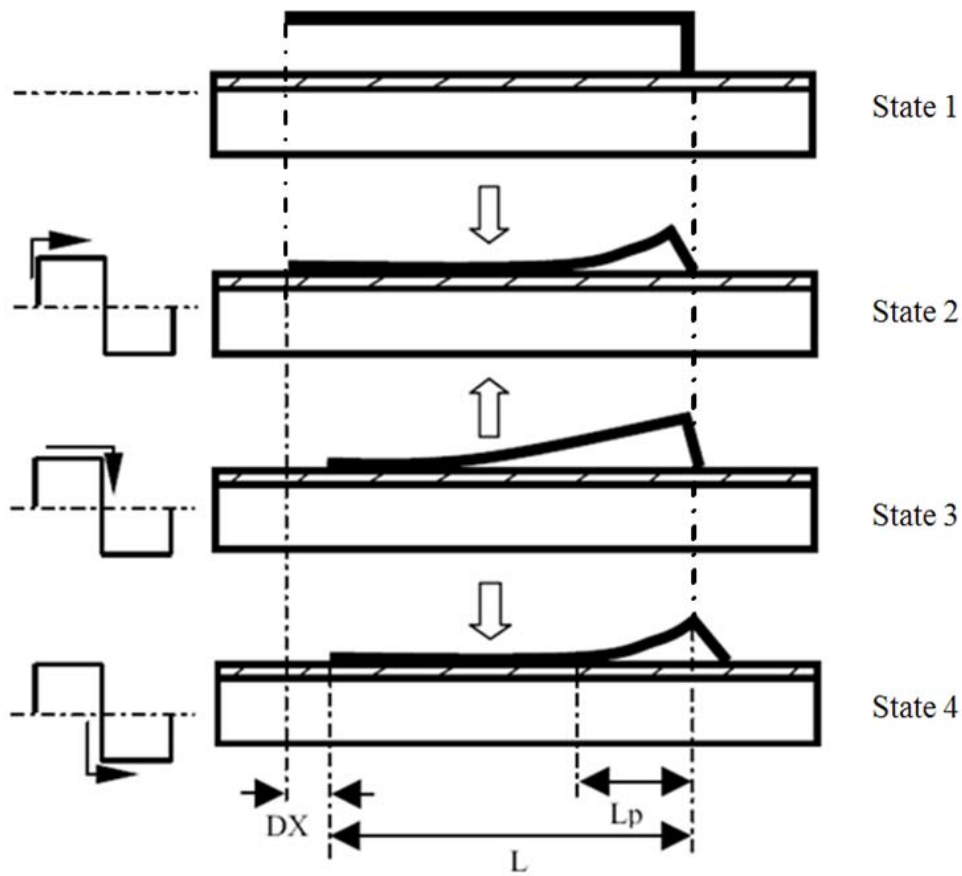


**Figure 2-24:** (State 1) The SDA is at rest before actuation. (State 2) Positive voltage is applied to the SDA, pulling down the plate. (State 3) Voltage is removed from the plate, causing the bushing to press forward along the insulator. (State 4) Negative voltage is applied, causing the plate to warp towards the insulator. The forward movement is denoted by  $DX$ , the length of the plate by  $L$ , and the warped portion of the plate by  $L_p$ . Once actuated, the SDA will alternate between State 2, State 3, State 4, and State 3 again to provide the forward movement [17].

#### 2.4.4 Other Actuators

There are many other categories of MEMS actuators, but unfortunately, they typically require specific fabrication processes [16]. Among these categories are piezoelectric actuators, which generate electric potentials in response to mechanical

stress; piezoresistive actuators, which change their resistivity in response to mechanical stress; and magnetostrictive actuators, which can change their shape when exposed to an external magnetic field. Since these categories of actuators require special materials and deposition techniques, the actuators within those categories will not be studied for this research effort.

## **2.5 Introduction to MEMS Microshutter Design Concept**

Because the time and budget was limited for this research effort, the PolyMUMPs™ process was chosen. A design was needed that would not depend on materials other than two releasable layers of polysilicon, which eliminated any possibility of using piezoelectric materials or designing shutters to function in three dimensions, such as those designed for the JWST and other “eyelid” shutters. A more mechanical approach was taken that utilizes gears and arrays of electro-thermal actuators to move arms with etched holes to uncover the apertures in the substrate. This approach and its functionality will be explored more in the following chapters.

## **2.6 Summary**

In this chapter, the fundamentals of CAI and ACAI functionality were discussed and explored. This examination revealed that microshutters are the best method to obtain a working ACAI mask. Various types of microshutter research and their applications were explored, to include those in current ACAI research. The advantages and disadvantages of these various microshutters were examined thoroughly in order to discover where certain deficits within the technologies might cause them to fail or be more inefficient than other designs. Noting what is within range for a master's thesis

effort, a fabrication process was explored as well as different actuation schemes for MEMS devices. With this knowledge, one can then deduce where shortfalls within the microshutter and ACAI community might lie, and how a new fabricated design might be able to close some of those technology gaps. This new design will be closely examined and tested in the next chapters.



### **3. Methodology**

As previously mentioned, the goal of this research effort is to design and fabricate a MEMS microshutter array. This array requires that apertures within the array can be opened and closed individually without disrupting the function of the other apertures. Due to the fabrication process used, this array must be designed to function with only two releasable layers of polysilicon. This section will discuss the various designs attempted and describe the final design in detail, as well as discuss implementation for testing purposes.

#### **3.1 MEMS Design Concepts**

Because no previous research projects have attempted to construct a microshutter array with these requirements, the initial design attempts took on an indiscriminate approach. The initial goal was simply to construct functioning microshutters that could be positioned as close together as possible to create the array. Failures in these designs inspired changes to the microshutter concept, culminating in the final design attempt in hopes that the original goal could be realized.

##### ***3.1.1 Wedge-style shutter using electro-thermal actuation***

The designs for the initial shutters were inspired by an optical iris and were submitted for fabrication in Run 84 of PolyMUMPS™. The optical iris, shown in Figure 3-1, changes its center aperture size through the movement of the blades. As the blades pull away from each other, the center aperture increases in diameter. The blades of the iris are curved in such a way that they slide smoothly to open and close, and each iris

contains enough blades so that the aperture remains relatively circular regardless of the diameter.

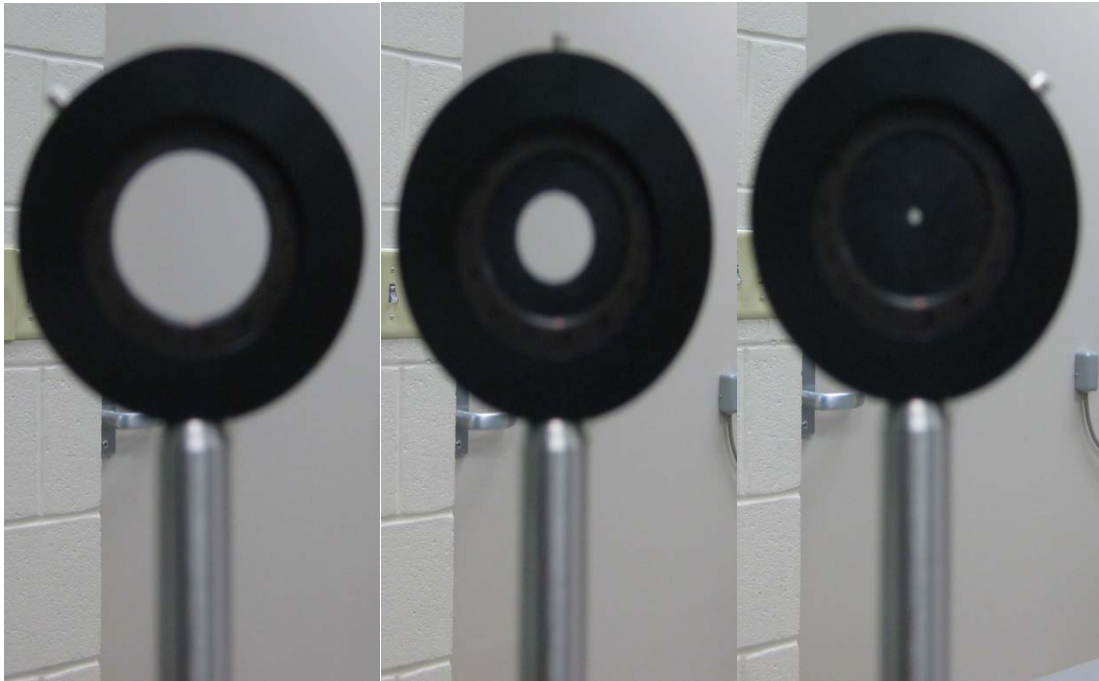


**Figure 3-1:** (left) The optical iris is shown fully open. (middle) The optical iris is shown half closed. (right) The optical iris is shown fully closed.

Due to the design rules enforced by PolyMUMPS™, creating an exact replica of an optical iris within the two layers of polysilicon proved to be a challenge. Instead, these first designs simplified the concept by using electrothermal actuation to open and close pie-shaped wedges of shutters over a theoretical 200- $\mu\text{m}$  aperture. All of the designs involved two layers of polysilicon; some included a layer of trapped  $\text{SiO}_2$ . This was done to limit residual stress within the wedges and to provide strength throughout the shutter. The thermal actuation was performed by either a 200- $\mu\text{m}$  single hot arm or a 250- $\mu\text{m}$  single hot arm. The length and design of the thermal actuator varied with the

wedges; the quarter wedges were paired with the 250  $\mu\text{m}$  hot arm, while the sixth wedges were paired with the 200  $\mu\text{m}$  hot arm.

Figure 3-2 and Figure 3-3 illustrate how the various wedges and hot arms were coupled together to create a wedge-style shutter. Table 3-1 illustrates how the colors in the following figures correspond to the various layers in the PolyMUMPS™ process.

**Table 3-1:** Colors of MEMS designs and their corresponding PolyMUMPS™ layers.

<i>Color</i>	<i>Layer</i>
Orange	Poly0
Light Red	Poly1
Dark Red	Poly1-2 stack
Grey	Poly2
Light blue	Poly2-Metal stack
Purple	Poly0-2-Metal stack
Black	Poly0-1-2-Metal stack

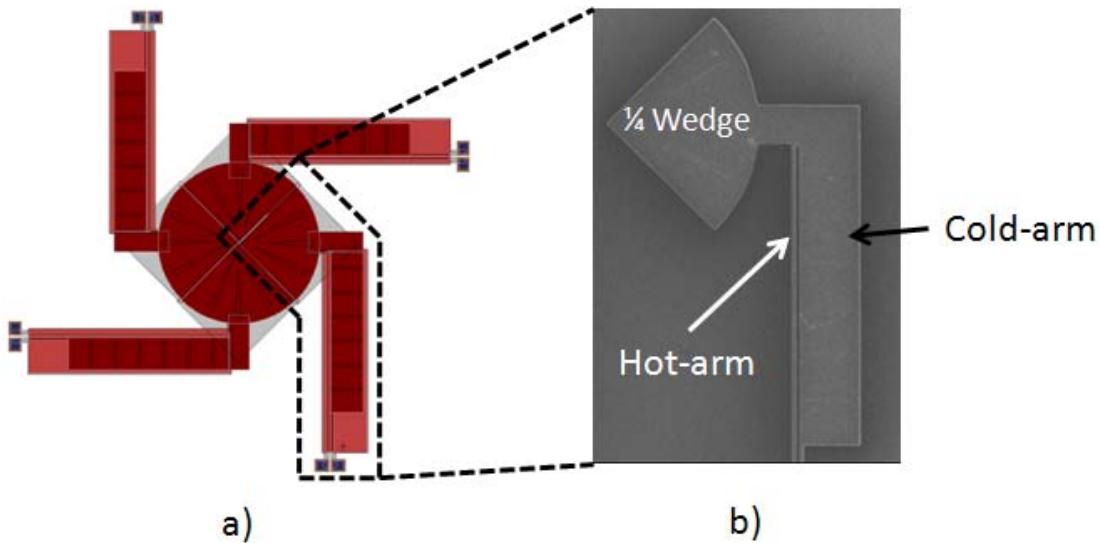


**Figure 3-2:** a) Test design of a quarter-wedge, single hot arm shutter. The hot arm is 250  $\mu\text{m}$  in length, and the wedge has a 100- $\mu\text{m}$  radius. This is a Poly1-2 stack with no trapped oxide layer. b) SEM picture of a single quarter-wedge single hot arm.

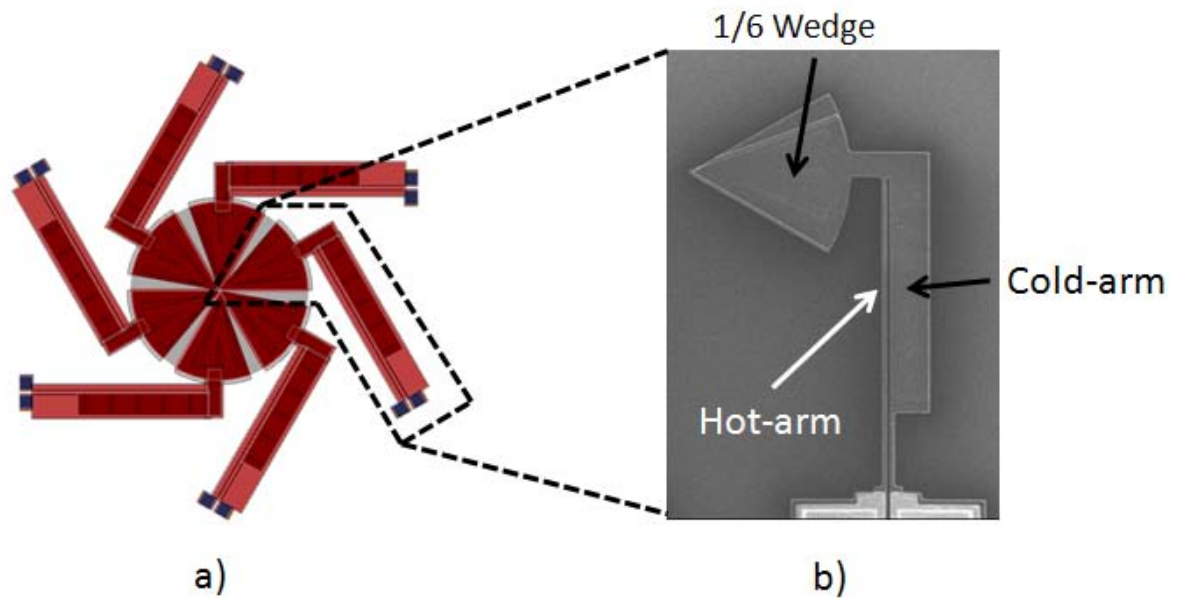


**Figure 3-3:** a) Test design of a sixth-wedge, single hot arm shutter. The hot arm is 200  $\mu\text{m}$  in length, and the wedge has a 100- $\mu\text{m}$  radius. This is a Poly1-2 stack with no trapped oxide layer, and the extra flaps of polysilicon allow for more conformal covering of the aperture. b) SEM picture of a single sixth-wedge, single hot arm shutter.

In addition to the complete wedge shutter designs above, individual wedges were fabricated in order to fully comprehend their properties. Four wedges and their corresponding hot arms were fabricated from each of the shutter designs above. An additional four wedges were fabricated using a quarter wedge with trapped oxide and a 250  $\mu\text{m}$  single hot arm, as shown in Figure 3-4.

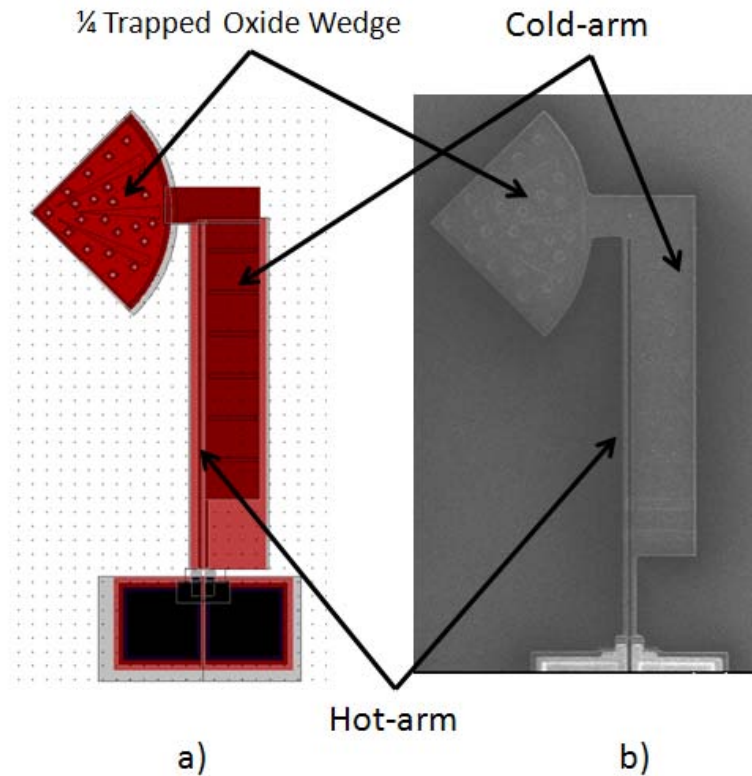


**Figure 3-4:** a) Test design of a quarter-wedge, single hot arm shutter. The hot arm is 250  $\mu\text{m}$  in length, and the wedge has a 100- $\mu\text{m}$  radius. This is a Poly1-2 stack with a trapped oxide layer. b) SEM picture of fabricated shutter.

While these designs are an acceptable first step in solving the problem of needing an array of microshutters, there are potential shortcomings that should be foreseen if not expected. Firstly, these designs do not actually provide an array of microshutters as needed for ACAI. These microshutters serve more as a proof-of-concept of an individual microshutter, not a full array. Secondly, the designs in Figure 3-2 and Figure 3-3 connected the thermal actuators in series. Potential problems with these designs arise when the thermal actuators do not receive the full voltage from the contact pads, meaning that they might not deflect evenly, if at all. Typically, thermal actuators require at least a 5-V drop across the actuator to see any significant movement; when the actuators are

connected in series, they will only experience a fraction of the voltage. There also is less room for the actuators to deflect, which would contribute to the shutter being unable to open fully.

### 3.1.2 *Final line-drivable array design*

The final design incorporates ideas from the Fabry-Perot ACAI device discussed in Section 2.2.2. Similar to that device, this design contains shutter flaps in two directions; the individual aperture only opens when both its shutter flaps move to uncover it. This design uses a drastically different actuation scheme than that seen in the previous designs and will be discussed in detail in the next section. An illustration of this design can be seen in Figure 3-5.

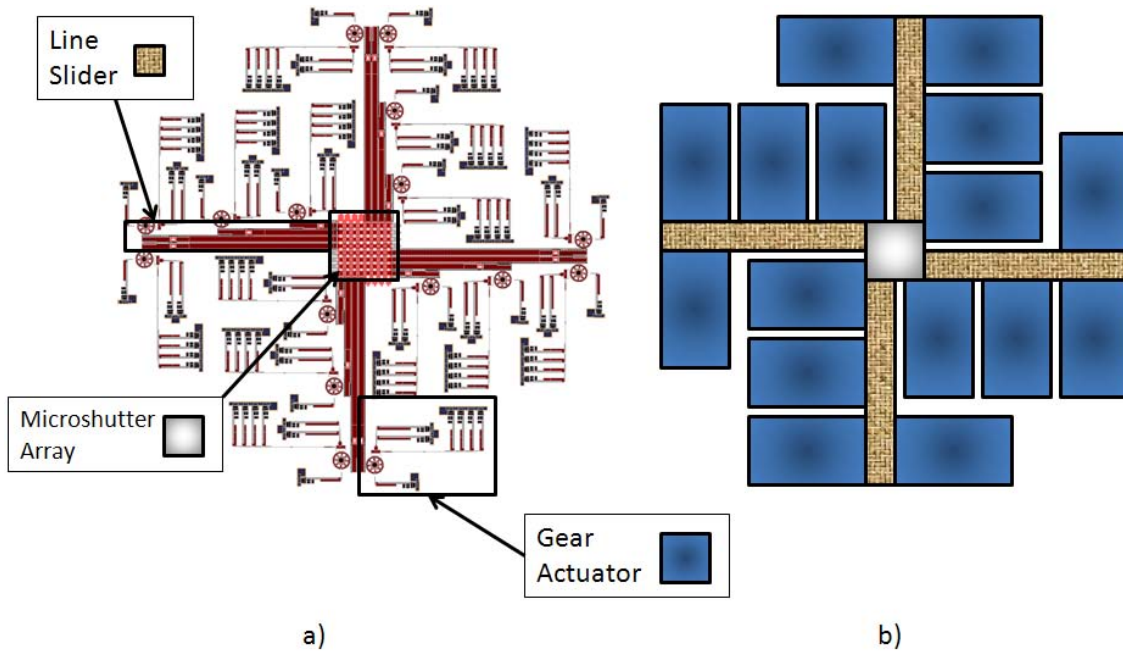


**Figure 3-5:** a) Line-drivable array microshutter design. The square in the center of the design is the actual microshutter array, while everything else provides the actuation scheme to drive the array. b) Simplified layout of microshutter array. There are four line sliders and 16 gear actuators in all.

## 3.2 Component Breakdown

This section will discuss in detail the layout and design of the line-drivable microshutter array. This array utilizes both releasable layers available through the PolyMUMPS™ process to create linear flaps of each layer to move vertically, in the case of Poly1, or horizontally, in the case of Poly2. This section will also discuss some of the obstacles encountered within the design process and how they were overcome.

### 3.2.1 *Shutter array*

The first obstacle encountered when designing the line-drivable microshutter array was deciding how the apertures would be laid out on the substrate. The aperture array was nominally chosen to be an 8 x 8 array of 20 μm square apertures. If the apertures were located adjacent to each other on the substrate, then the shutter flaps would require up to 160 μm of movement in order to clear all apertures. This is by no means an impossible feat, but it requires extensive actuation and space on the substrate for the actuation scheme; as substrate space was limited for this effort, adjacent apertures were ruled out for this research.

If actuation was not an issue, diffraction could then become a limiting factor. The Huygens-Fresnel Principle states simply that if the wavelength is large compared to the aperture, the waves will spread out at large angles into the region beyond the obstruction [1]. Two types of diffraction exist: Fresnel, or near-field diffraction, and Fraunhofer, or far-field diffraction. For Fraunhofer diffraction to exist, the following relationship must be satisfied at the observation point:

$$R \gg \frac{|x'_{\max}|^2}{\lambda} \quad (3.1)$$

where  $R_0$  is the distance from the aperture to the observation point,  $|x'_{\max}|$  is the distance from the optic axis to the farthest extent of the aperture, and  $\lambda$  is the wavelength of light passing through the aperture [1]. In this case, a 20  $\mu\text{m}$  square aperture and a HeNe laser wavelength of 632.8 nm combine to yield a minimum  $R_0$  of approximately 316  $\mu\text{m}$ . Should the pixel plane be located further than 316  $\mu\text{m}$  from the aperture, Fraunhofer diffraction will be observed, meaning that when a light wave passes through one aperture to a designated pixel, the surrounding pixels will receive photons as well.

Because the scope of this effort is limited, the focus of the research is on the microshutter array, not the signals that the pixels will receive. As such, the shutter array is designed to have the apertures spaced 20  $\mu\text{m}$  apart. This orientation would then provide ease of actuation, as the flaps contain holes periodically through the array so that they only need to be moved 20  $\mu\text{m}$  instead of 160  $\mu\text{m}$ . The aperture array is shown in Figure 3-6, and the full shutter array with the apertures marked is shown in Figure 3-7.

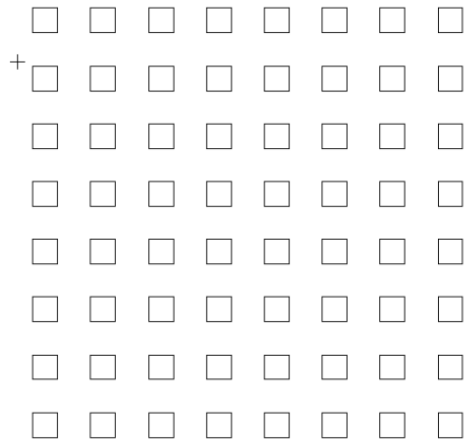


**Figure 3-6:** Aperture array that the microshutters are designed to cover.



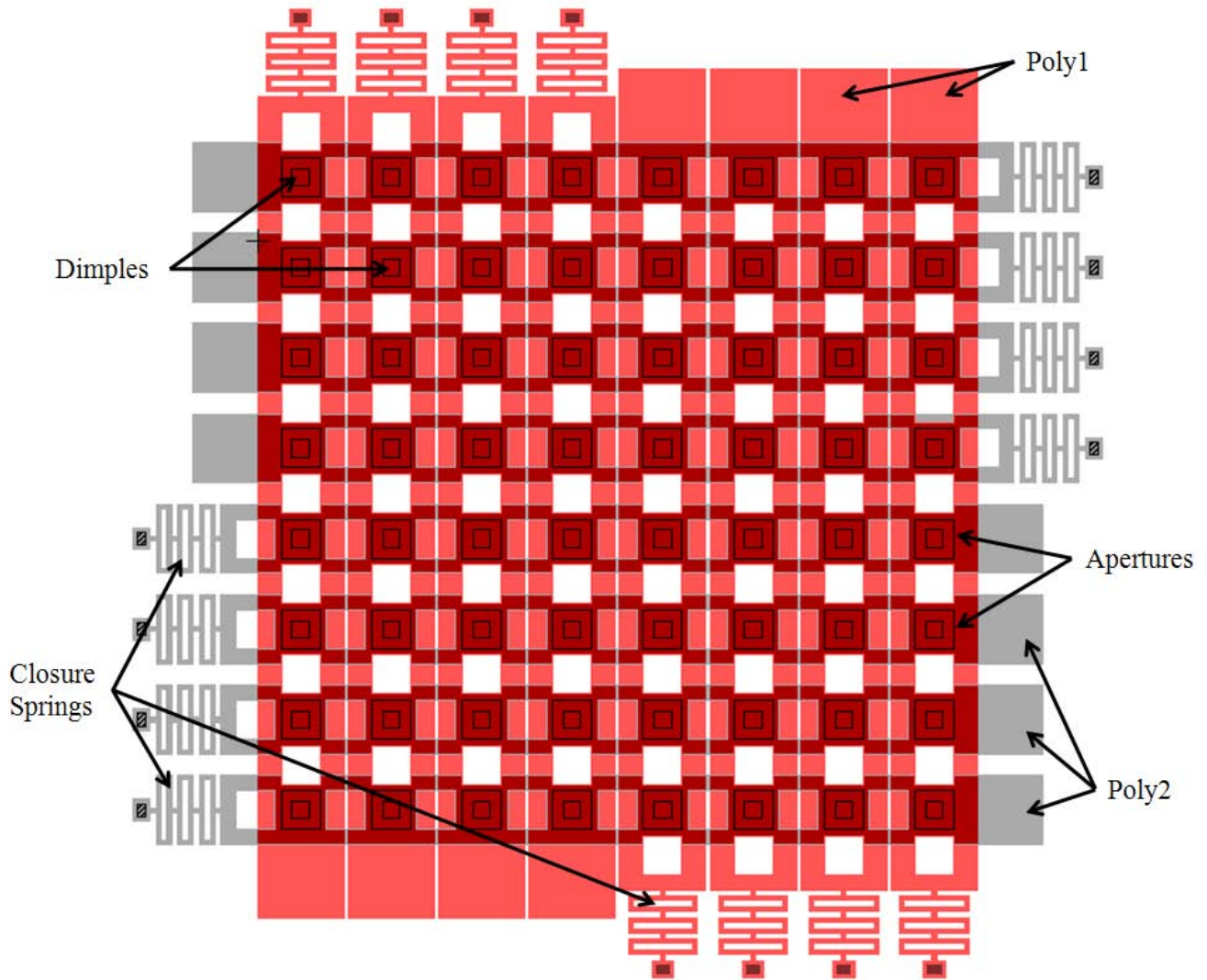


**Figure 3-7:** Line-drivable microshutter array. As before in the previous designs, the light red color corresponds to the Poly1 layer, the grey corresponds to the Poly2 layer, and the dark red is where the two layers overlap. Closure springs are located at the end of each flap, and dimples are located where each aperture should be to minimize stiction when the apertures have not yet been etched.

When studying the design of the line-drivable array, the viewer may notice the differences in the widths and shapes of the Poly1 flaps versus the Poly2 flaps. Due to the conformal nature of the PolyMUMPS™ process, some adjustments were needed so as to ensure the possibility of full functionality of the array. As mentioned in Section 2.3, the

Poly2 layer conforms to whatever layers might lie beneath it. In Figure 3-8, an array of microshutters consisting of Poly1 and Poly2 flaps that have the same shape and width has been designed. The conformal nature of PolyMUMPS™ becomes detrimental to the functionality of the design; the dips in the Poly2 layer are too deep and will not allow those flaps to move.

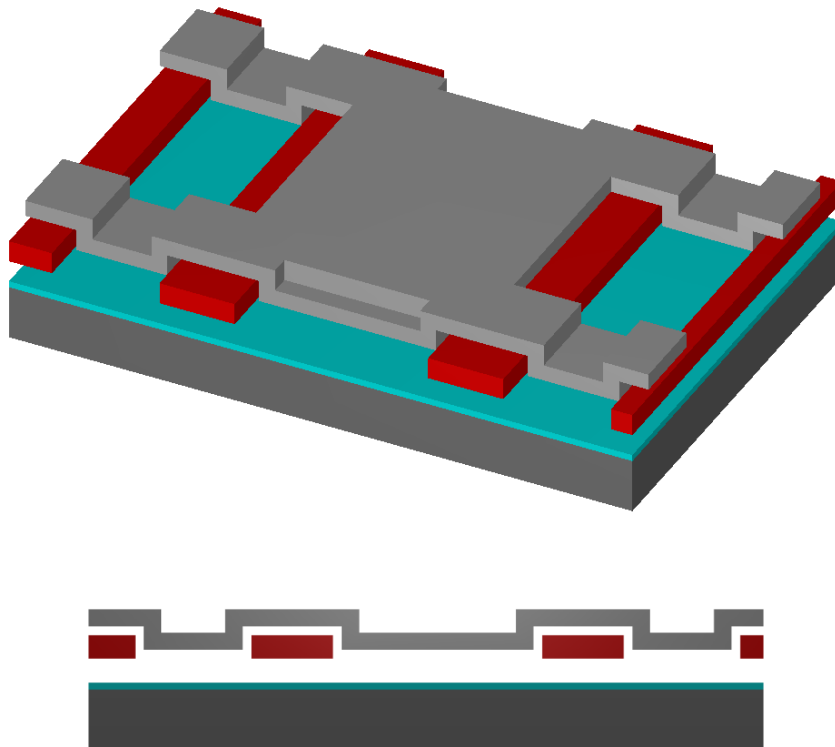


**Figure 3-8:** (top) 3-D view of the original design for the microshutters. The conformal nature of the PolyMUMPS™ process causes the Poly2 layer to fill in the gaps between the shutters, which then keeps the Poly2 flap from moving. (bottom) Cross-section of the original shutter design accentuating where the Poly2 layer will fill in the gaps.

As such, adjustments were made to the widths of the two different flaps. The Poly1 flaps were designed to be as wide as possible without fusing them together; this will minimize the depth of the Poly2 dips between the Poly1 flaps. The distance between each Poly1 flap is 2  $\mu\text{m}$ . The Poly2 flaps were also indented at each location where a

hole in the Poly1 flap would be so that the Poly2 dips would not occur within those holes, thus locking the flaps. In order to ensure the flaps would not break, the aperture and hole size had to be adjusted. With an aperture and hole size of 20  $\mu\text{m}$ , the Poly2 flaps would have only one micron of polysilicon holding the flap together; this most certainly would break either during the release process or in testing. To correct this, the aperture and hole size was reduced to an 18  $\mu\text{m}$  square. This then allowed for 3  $\mu\text{m}$  of Poly2 to hold the flap together, which means the flap is significantly stronger.

### ***3.2.2 Individual gear assemblies***

As shown before in Figure 3-5, the shutter array discussed in the previous section requires a great amount of actuation for it to function properly. Because electro-thermal actuators tend to have a maximum linear displacement of approximately 12-14  $\mu\text{m}$ , using solely electro-thermal actuators would not provide the necessary amount of movement necessary to have a functioning microshutter array.

A prior AFIT thesis encountered a similar problem when developing MEMS safe-and-arm devices [16]. In that research, actuation was achieved through a 4-step process involving two devices termed the “pawl” and “drive” mechanisms. The combined movement of these two mechanisms provided a gear-like actuation when driven by correlating AC electrical signals. An example of that system is shown in Figure 3-9.

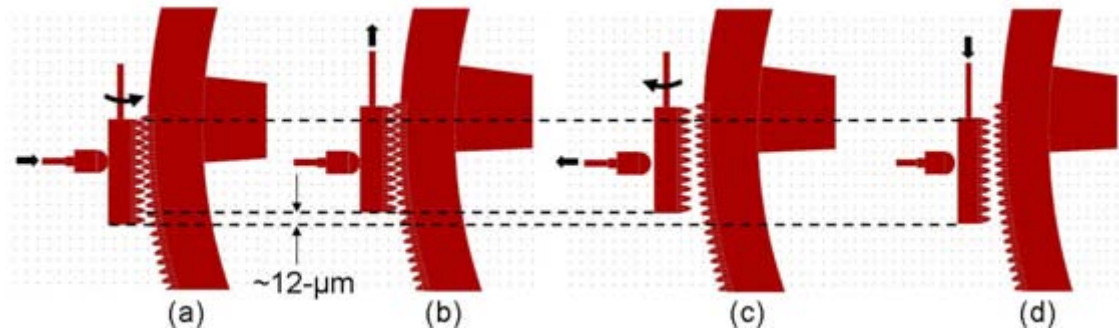


**Figure 3-9:** Illustrated representation of a single cycle of the 4-step pawl and drive mechanisms from a previous thesis effort; (a) shows the pawl pushing the drive gear to an engaged position; (b) depicts the drive actuators pulling in a linear motion causing the gear to rotate; (c) at the peak of the drive stroke, the pawl is released allowing the spring tension in the drive gear arm to clear the drive from the wheel gear teeth; (d) the drive actuator then returns to its original position and the process is repeated until the desired motion is achieved. [16]

While an ideal situation would have allowed for a similar system to actuate the flaps of the array directly, space restrictions on the substrates submitted to PolyMUMPS™ prevented this from happening. As such, an actuation scheme that involved gears was implemented to save on space. A similar pawl and drive system was used to drive the gears, and each of the flaps from the shutter array was attached to a slider mechanism that both anchored the arm and provided the necessary gear teeth to provide actuation. An example of the slider mechanism is shown in Figure 3-10. Unlike the previous thesis effort, this gear actuator design connected the pawl and drive system so as to prevent slipping during actuation. This design is illustrated with both the hot arms connected and the driving gear wheel in Figure 3-11.

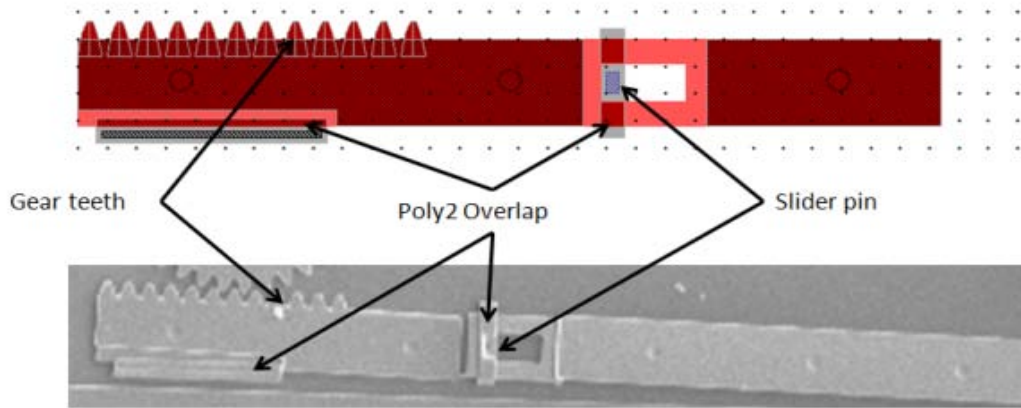


**Figure 3-10:** Design (top) and SEM picture (bottom) of the slider mechanism that is attached to all flaps from the microshutter array. The gear teeth receive the actuation from the gear mechanism, the two Poly2 overlaps provide anchors to keep the flap from floating away during the release, and the slider pin ensures movement only ranges from 0-20  $\mu\text{m}$ .

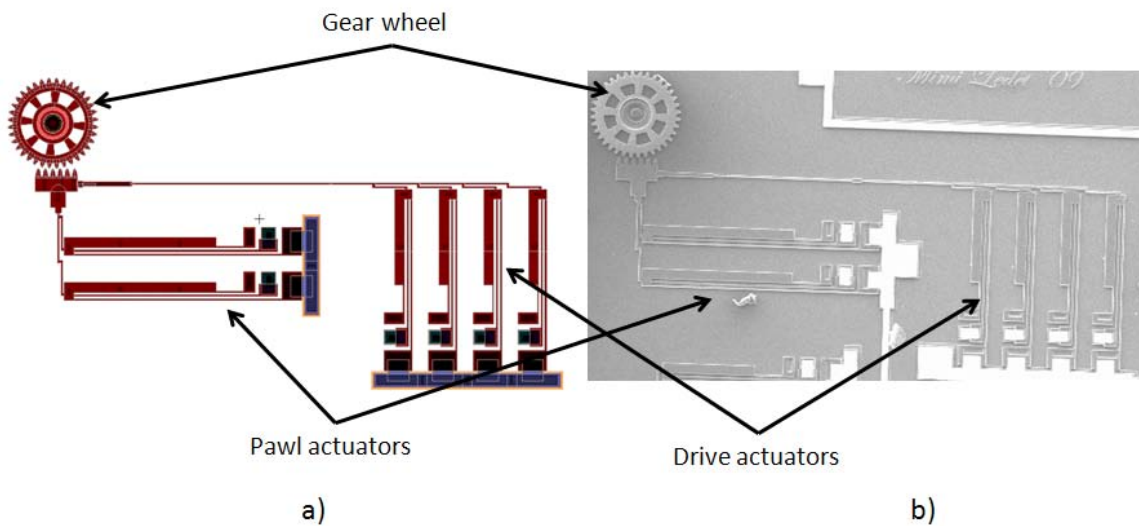


**Figure 3-11:** Design of the individual gear actuator assembly. In this design, the pawl and drive gears are connected so that no slipping between the two mechanisms occurs during actuation. In this setup, the drive gear is actuated first, rather than the pawl as in Figure 3-9; the actuation is still a very similar 4-step process as before.

Unlike the shutters actuated by SDAs, this actuation scheme should reverse so that the shutters may close slowly. Despite the possibility of reversal, however, a secondary closing mechanism was incorporated into the design so that if a flap corresponding to an

aperture other than the desired shutter was to open, the user could remove all electrical signals to that particular flap and it would snap shut. This mechanism was realized in designing a box spring to the end of each flap, as in Figure 3-12. Unfortunately, with a closing mechanism such as this, as soon as both the drive and pawl are returned to neutral in their 4-step actuation scheme, the flap will snap shut. As such, a lock mechanism needs to be in place to ensure the flap continues to open. This was accomplished with another electro-thermal actuator strategically located with the rest of the gear actuators. This can be seen in Figure 3-13. The lock actuator is designed to keep the gear from moving as long as it has no electrical signal. When the lock actuator receives a sufficient voltage, it will pull away from the gear, enabling it to spin. When that voltage is turned off, the lock actuator will snap back into place, preventing further movement of the gear.

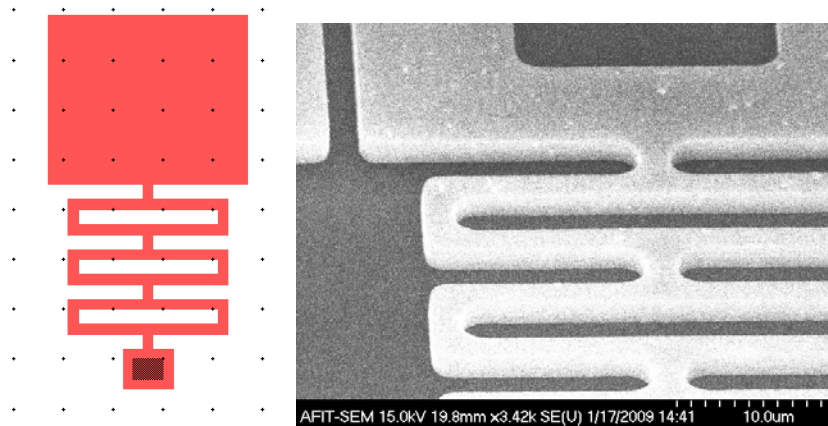
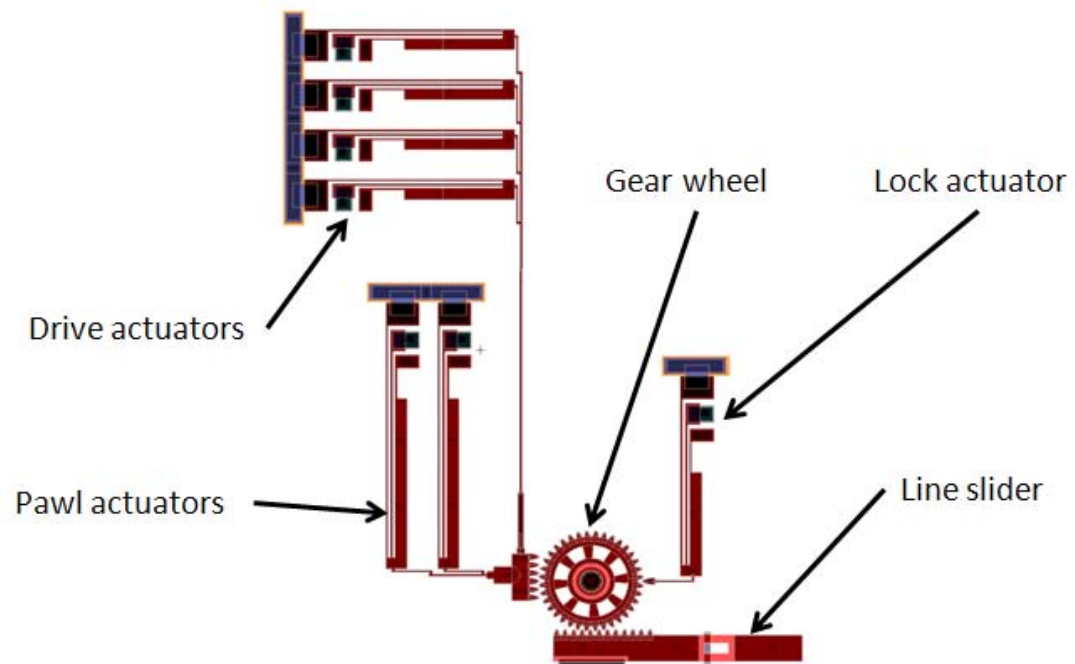
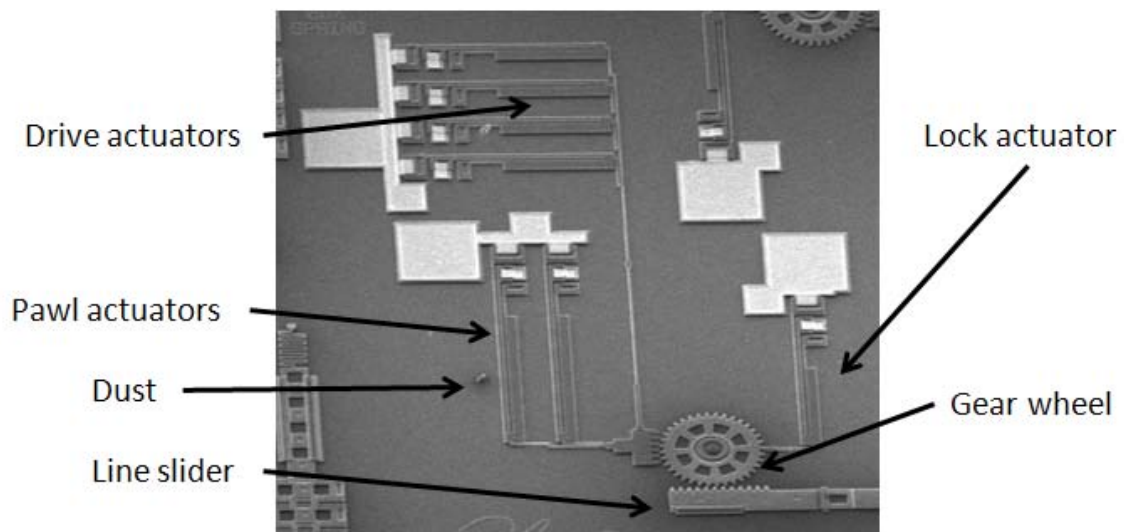


**Figure 3-12:** Example of the box spring incorporated at the end of each microshutter flap. The spring acts to keep the entire array closed when there are no electrical signals to the actuation scheme.



a)



b)

**Figure 3-13:** a) L-Edit design of how the lock actuator is incorporated into the gear actuator. Without having an electrical signal, the lock actuator prevents movement of the gear. b) SEM picture of two test full gear actuators with the lock actuator present.



Because the space allotted for this run was limited, a few more adjustments were needed to ensure that all the microshutter flaps were able to move. First, each microshutter flap required its own gear actuator; given the close proximity of the flaps, this would necessitate increasingly longer and longer flaps to accommodate the entire array. Secondly, each gear actuator needed to be reached by three separate micro-wires to provide the signals to the drive, the pawl, and the lock actuators, meaning that sufficient space for wiring had to be accounted for in the layout of the design. Fortunately, the symmetry of this design allowed for some repeatability in the layout and still allowed adequate space for wiring. The final layout is shown in Figure 3-14.

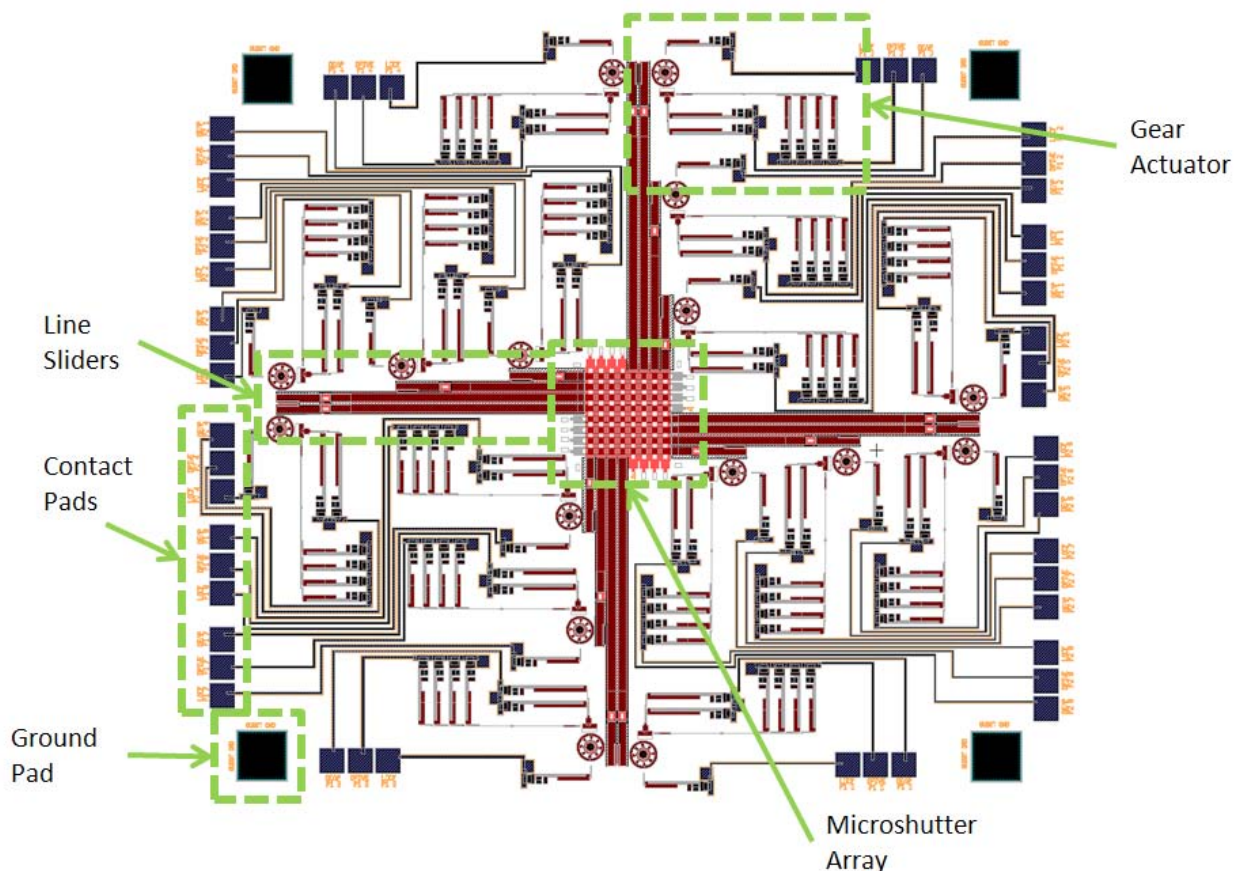


**Figure 3-14:** Illustration of the final layout of the microshutter array design. Note the symmetry and the wiring scheme.



### **3.3 Microshutter Implementation**

Of course, designing a microshutter array accomplishes nothing if it cannot be tested and implemented in some way. This section will discuss the steps needed to fully prepare the chips containing the microshutter array for integration into an ACAI system.

#### ***3.3.1 Microshutter Preparation***

The first goal in preparing an optically functional microshutter array is etching the apertures in the substrate so that light may pass through the shutters when they are open. This is accomplished through a process known as deep reactive ion etching (DRIE), but a few steps are needed before this can be done.

First, a process called lithography must be performed to create the image of the apertures onto the back of the substrate. The pattern of the apertures is fabricated with chrome on a 4" square glass mask. This mask will be used later to imprint the pattern onto the back of the chip containing the microshutters. It should be noted that the chips are received from the foundry covered in photoresist so as to protect the underlying devices prior to their release. The microshutter array was fabricated on a silicon substrate approximately 700- $\mu\text{m}$  thick. This substrate is too thick for a successful DRIE run later, so it is thinned 400  $\mu\text{m}$  via a simple surface etch. Once the substrate is thinned, a 1.5- $\mu\text{m}$  oxide layer is deposited via PECVD to provide the mask for the DRIE run. Once the chip's substrate has been thinned and covered with oxide, it is then cleaned and photoresist is spun onto its backside. The mask mentioned earlier and the photoresist-covered chip are then placed inside a mask aligner, where two optic systems allow the user to mechanically align the features on the mask to their designated location on the

back of the chip. The mask aligner then exposes the areas of photoresist not covered by the mask, thereby changing the underlying resist chemically. The chips then undergo a developing process, which removes all the exposed resist and leaves the unexposed resist in the pattern as seen on the mask.

At this point, the chip now contains the unreleased microshutter array on one side coated with photoresist and an oxide layer covered with patterned photoresist on the other. The oxide on the patterned side of the chip will serve as the mask for the DRIE process, but in order to do this, it must be patterned itself. The chip undergoes a reactive ion etch (RIE) process to remove the oxide from the exposed backside of the chip. Once this is completed, the photoresist is removed by acetone. Following this step, the exposed unreleased devices are coated with a thermal paste for added protection during the DRIE process. After the DRIE is completed, the chips are mostly ready for integration. The last step for the chips involves the removal of the thermal paste in an isopropyl bath, followed by the releasing of the microshutter devices by dissolving the oxide layers in HF acid. Once the chips are dry, their preparation is complete.

### ***3.3.2 Integration and Assembly***

The first step in integrating the microshutter array is ensuring that a platform is ready to accept the array. In this research effort, a standard microscope slide will provide this platform for all needed optical testing, because the thin glass in the slide will have little, if any, optical effects on the apertures. As the microshutter array contains 52 contact pads and most probe-testing stations have a maximum of four micro-probes, larger contact pads will be needed for any substantial electrical testing of the array.

These contact pads will be patterned onto the slide using the same mask aligner process with photoresist. The contact pads will be created of an evaporated gold film and will be large enough for standard small wire clamps to reach. Four contact pads will be evaporated onto the slide: one each for the lock, pawl, and drive actuators, and one more for the ground plane. Once the large contact pads are in place on the microscope slide, the chip containing the microshutters can then be adhered to the slide. The contact pads on the slide then need to be connected to the contact pads on the chip via wire-bonding; this process uses 10  $\mu\text{m}$  gold wires to electrically and physically connect micro-contacts to larger contacts. Only some of the contact pads from the chip will be connected to the slide in this effort; this is purely to show how the microshutters function and not to code any images. When this step is complete, then the microshutter array is ready for testing.

### **3.4 Chapter Summary**

In this chapter, the methodology for designing a functional set of microshutters was reviewed. Three designs of microshutters were analyzed, and their advantages and disadvantages discussed. A thorough review of a fourth microshutter design was conducted that incorporated a line-drivable array of overlapping polysilicon flaps. An aperture scheme was analyzed and optimized for this research effort, and a full two-dimensional microshutter array was designed. Obstacles in the form of conformality in the polysilicon layers and diffraction were discussed, and adjustments to the microshutter array design were implemented to account for and overcome these limits. An actuation scheme was designed that involved the coupling of groups of electro-thermal actuators and pairing them with a gear system to move each of the flaps. As each flap was designed

with a small spring designed to keep it closed, the lock actuator was added to overcome the forces of the automatic closing springs. Finally, preparation processes and integration steps were discussed so that implementing the microshutter design into a proper testbed may be accomplished. The results of that testing will be disclosed in Chapter 5.

## **4. Analytical Modeling**

This chapter will review the concepts of electro-thermal actuators. Specifically, it will evaluate different forms of electro-thermal actuation schemes and investigate their output capabilities and their functionality. Additionally, a technique to link these devices together in order to provide linear displacements and increase their output forces will be explored in their value to this experiment. Based on these evaluations, each configuration will be assessed in terms of the amount of force and deflection it is capable of producing for a given amount of instantaneous power. This information will be used to form a basis from which to evaluate performance.

### **4.1 Electro-Thermal Actuator**

As previously discussed in Section 2.4.2, the electro-thermal actuator uses thermal expansion caused by Joule heating, shown in Figure 2-20, to create mechanical displacement. Through this actuation scheme, voltages of less than 20 V are converted to displacements around 15  $\mu\text{m}$ . This actuation scheme is desirable in many applications due to its low power requirements and performance reliability. A previous research effort at AFIT by Captain Roger Platteborze evaluated these actuators in great detail [16], and so this section will present an abridged summary of their functionality.

#### ***4.1.1 Electro-Thermal Actuator Analysis***

Figure 4-1 shows a voltage-versus-deflection curve from an electro-thermal-mechanical analysis modeled in CoventorWare<sup>®</sup> for a 300- $\mu\text{m}$  stacked Poly1/Poly2 single hot-arm [16]. The data shows that when 12 volts is applied to the actuator, a maximum

deflection of just over 25  $\mu\text{m}$  is possible; this deflection also translates to a maximum force of over 12  $\mu\text{N}$  [16].

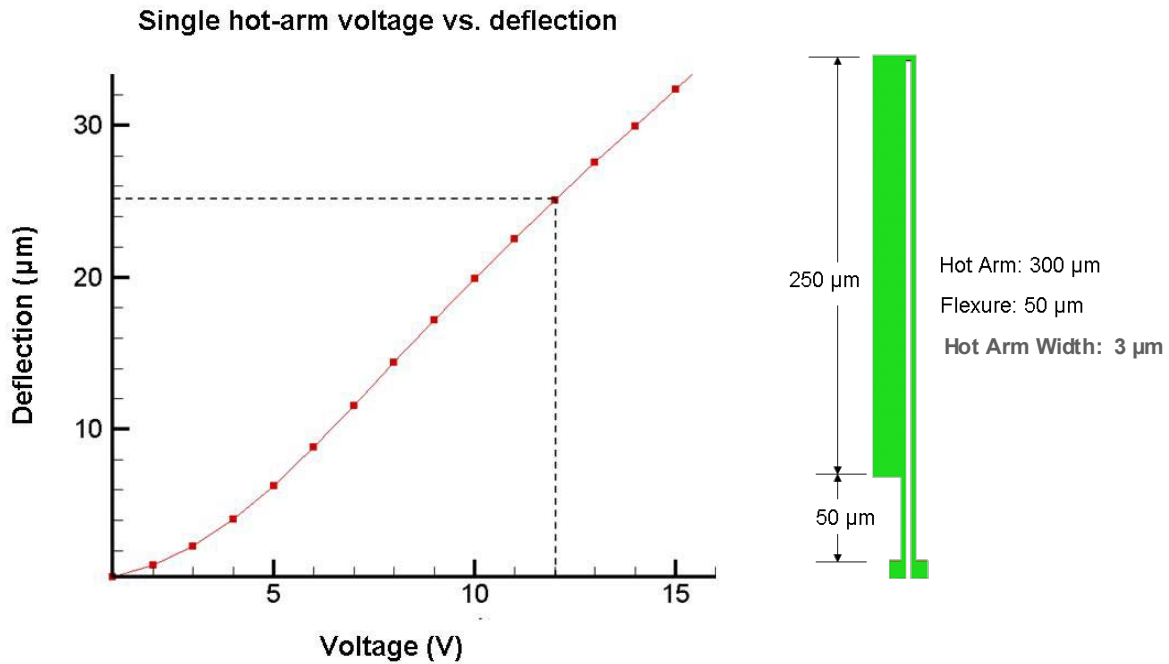


**Figure 4-1:** Applied voltage versus deflection curve for Poly1/Poly2 stacked 300- $\mu\text{m}$  single hot-arm actuator (shown on right); analysis modeled in CoventorWare® Version 6.0 [16].

In a double hot-arm device, both hot-arms contribute to the lateral deflections from Joule heating; while the deflections themselves are less than that of the single hot-arm, the forces behind those deflections are increased due to the curvature of both hot-arms. Figure 4-2 shows the voltage-versus-deflection curve for an electro-thermal-mechanical CoventorWare® analysis of a double hot arm actuator using the same cold arm as the one used for modeling the single hot arm device [16]. The deflection at 12 volts for this actuator is approximately 6  $\mu\text{m}$  shorter than the 25  $\mu\text{m}$  seen from the

single hot-arm; this stems from the higher resistance of the double hot-arm, thus causing lower current flow.

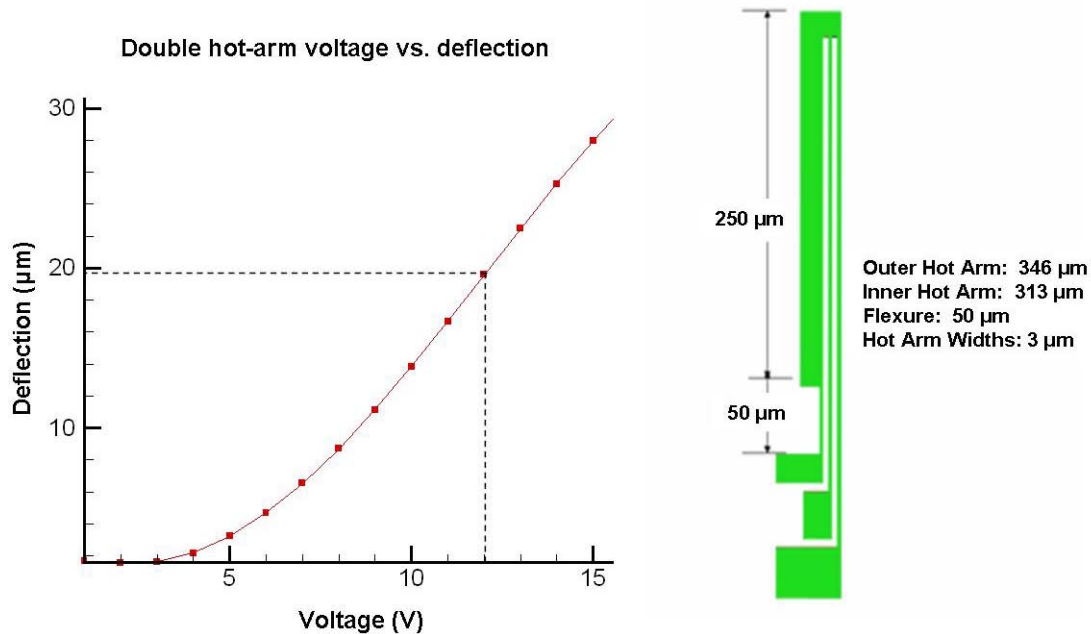


**Figure 4-2:** Applied voltage versus deflection curve for Poly1/Poly2 stacked 300- $\mu\text{m}$  double hot-arm actuator (shown on right); analysis modeled in CoventorWare Version 6.0 [16].

Platteborze also conducted a simple CoventorWare® analysis of the currents and forces available from these devices. In it, he revealed that the double hot-arm provided more than double the force available from the single hot-arm. He also studied how much power would be needed to drive the two devices in order to determine which was more efficient; his work concluded that the double hot-arm is three times more efficient than the single hot-arm [16]. His complete comparison of these devices can be seen in Table 4-1.

**Table 4-1:** Comparison of Single and Double Hot-Arm Thermal Actuator Devices [16]

	Applied Voltage	Current	Power	Force	Force/Power Ratio
Single Hot Arm	12 V	13.7 mA	164 mW	12.7 $\mu$ N	0.08
Double Hot Arm	12 V	8.15 mA	98 mW	26 $\mu$ N	0.26

#### 4.1.2 Wedge-style Shutters using Electro-Thermal Actuation

While the coupled electro-thermal actuators studied in Sections 4.2 and 4.3 all use the double hot-arm as their basis, the wedge-style shutters presented in Section 3.1.1 all used a single hot-arm as the basis of their operation. Through CoventorWare®, iterative studies were performed to simulate the opening of the shutters through increasing input voltages. The first study was performed for the quarter-wedge shutter without the trapped oxide. In this study, input voltages to all four hot-arms were incrementally increased from 1 V to 15 V. Figure 4-3 shows the difference between operating the shutter at 5 V and at 12 V, which is typically the optimum input voltage for electro-thermal actuators due to their maximum deflection and repeatability. The aperture is magnified and shown to be 47  $\mu$ m.

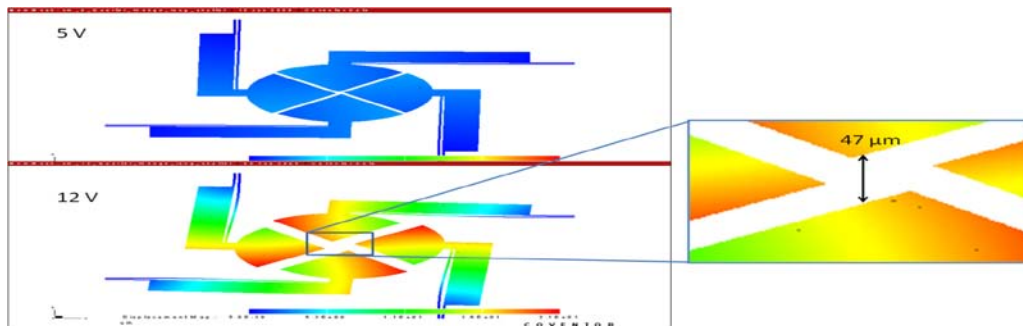


**Figure 4-3:** CoventorWare® simulation of a Poly1/Poly2 stacked, 250- $\mu$ m-long quarter wedge shutter at both 5 V and 12 V. The aperture is 47  $\mu$ m when the shutter is at 12 V.



A similar study was performed on the sixth wedge shutter. Again, all six of the electro-thermal actuators received the same incremental voltage increases from 1 V to 15V. Figure 4-4 illustrates the CoventorWare® results at both 5 V and 12 V. In this case, the aperture is smaller, only 33  $\mu\text{m}$ .

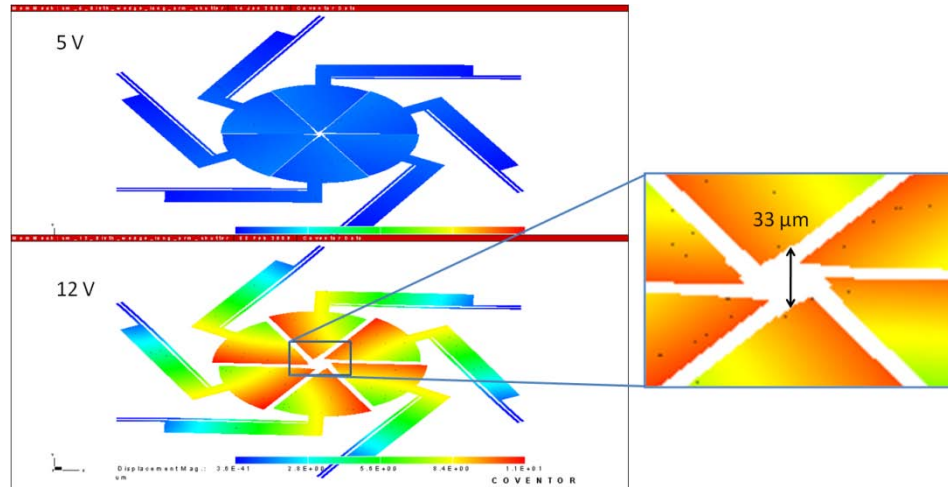


**Figure 4-4:** CoventorWare® simulation of a Poly1/Poly2 stacked, 200- $\mu\text{m}$ -long sixth wedge shutter at both 5 V and 12 V. The aperture is 33  $\mu\text{m}$  when the shutter is at 12 V.

When comparing these two shutters, not only is it important to compare the apertures available at 12 V, but it is also prudent to analyze the deflection vs. power curves as well as the power requirements to achieve the aforementioned apertures. Table 4-2 delineates the power requirements for each shutter for each aperture, and Figure 4-5 analyzes the deflection vs. power requirements for an individual wedge from each shutter.

**Table 4-2:** Power requirements at 12 V for each wedge shutter.

	Voltage	Aperture	Total Power Needed
Sixth Wedge	12 V	33 $\mu\text{m}$	1300 mW
Quarter Wedge	12 V	47 $\mu\text{m}$	737 mW

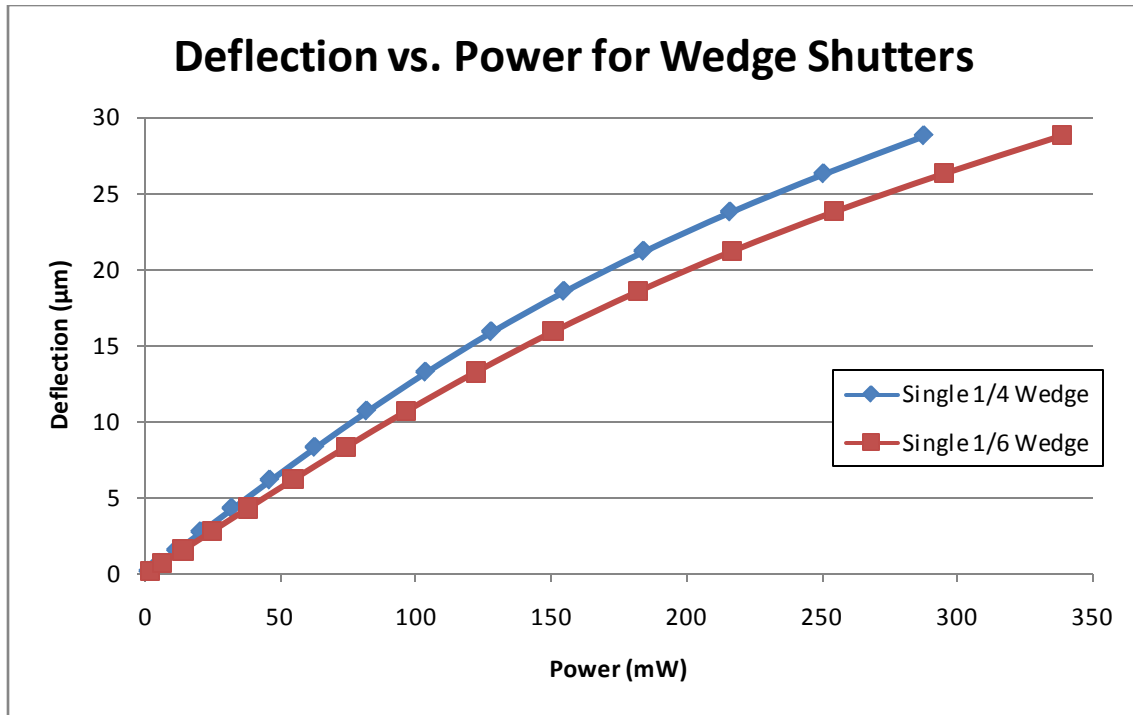


**Figure 4-5:** Deflection vs. power curves for an individual wedge from each shutter type. These values were obtained from iterative studies in CoventorWare®.

Not only does the sixth wedge shutter provide a smaller aperture, but it requires much more power to actuate, most likely stemming from the two more electro-thermal actuators required to operate this shutter. The sixth wedge shutter's smaller aperture is a direct result of the shorter electro-thermal actuators used in its design. Even so, the quarter wedge is able to achieve more deflection per unit power, and this in turn causes the aperture available with this shutter to be larger than that available from the sixth-wedge shutter.

#### *4.1.3 Electro-thermal Actuator Summary*

In order to have a functioning microshutter array, actuators must be incorporated into the design so that the components of the array move as desired. Section 2.4

discussed the various methods of MEMS actuation and determined that electro-thermal actuation was best suited for this application due to its repeatability and relatively low voltage and space requirements. Figure 4-6 compares the actuator displacement vs. applied power for both single and double hot-arms; this clearly shows that while greater deflection can be realized with the single hot-arm, the double hot-arm provides greater efficiency in converting that power into actual displacement whenever power above 50 mW is involved.

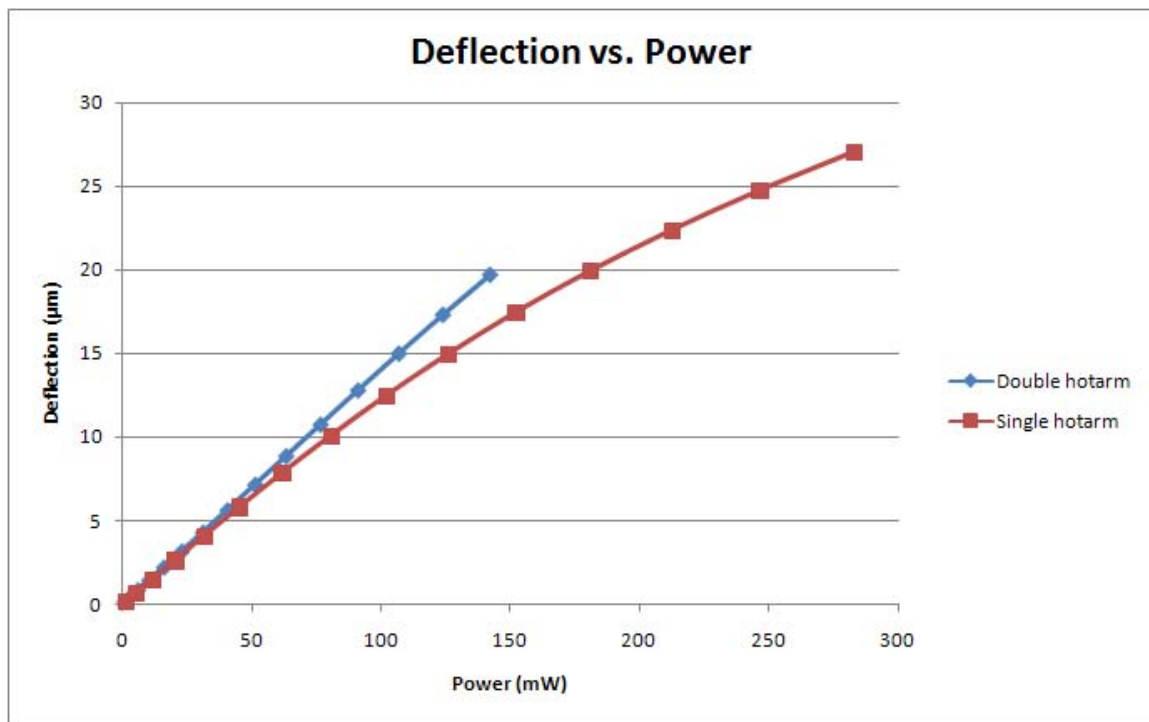


**Figure 4-6:** CoventorWare® analysis of actuator displacement vs. applied power for both the single and double hot-arms.

## 4.2 Coupled Electro-Thermal Actuators

Since electro-thermal actuators become unreliable if used to the maximum of their capability, another method for gaining necessary force and deflection without sacrificing

reliability must be explored. Fortunately, the electro-thermal actuators' geometry lends itself easily to coupling, or grouping them together, to maximize their performance and enhance their capability and reliability. This section will discuss a general coupling strategy for the double hot-arm and the two coupling schemes used in this effort and evaluate their overall performance.

#### *4.2.1 Coupled Actuator Designs*

Because the microshutter flaps designed to be moved are much larger than the actuators themselves, it can be safely assumed that more than one actuator will be needed to provide the necessary force to operate the microshutters. To bank the actuators together, a 2.5- $\mu\text{m}$  wide coupling beam was used to connect the actuators as in Figure 4-7. This 2.5- $\mu\text{m}$  beam is a Poly1-2 stack and is designed to be thick enough to provide enough rigidity to exert force in a somewhat linear motion, yet flexible enough to maintain that near-linear motion when the actuators are at their maximum deflection.

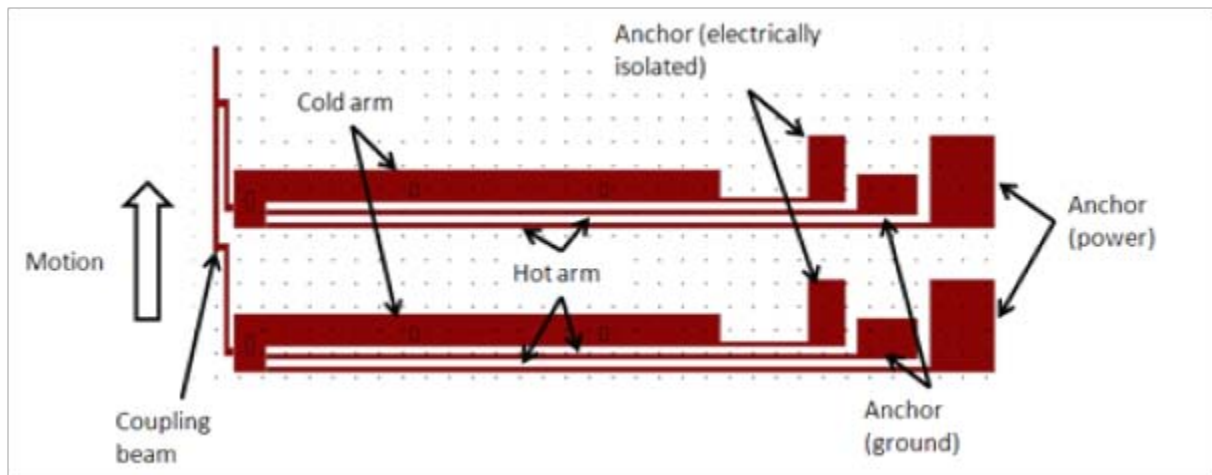


**Figure 4-7:** L-Edit design of two coupled double hot-arm thermal actuators.

With this coupled beam design, any number of electro-thermal actuators can be banked together to create a stronger, more reliable actuation scheme. Because surface area for the microshutter array was limited, the designs for this research effort strove to optimize actuation strength while still leaving enough space so that each microshutter flap could be individually actuated. This optimization led to the selection of two and four banked actuators for the pawl and drive gears, respectively. These can be seen in Figure 4-8.

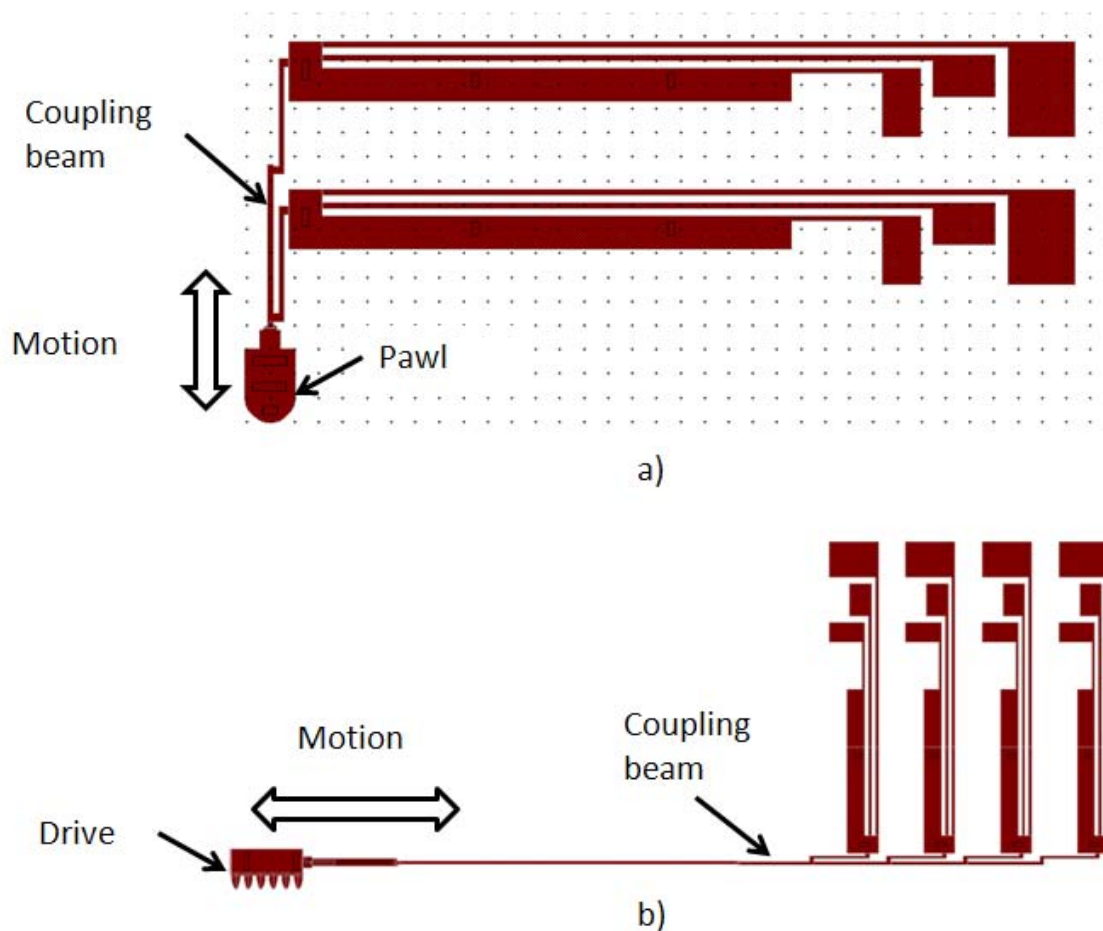


**Figure 4-8:** a) Two banked electro-thermal actuators coupled together to provide the pawl device for the gear actuator. b) Four coupled electro-thermal actuators banked together to provide the drive for the gear actuator.

#### 4.2.2 Coupled Actuator Analysis

Of course, these designs will be of no use if their functionality is not fully explored and analyzed. Platteborze [16] used CoventorWare® to calculate and predict the deflection and force outputs of various numbers of banked electro-thermal actuators. His work demonstrated that the higher the number of banked actuators, the higher the force available for a given deflection. Figure 4-9 illustrates the difference between the force vs. deflection curves for banked actuators containing between one and five actuators.

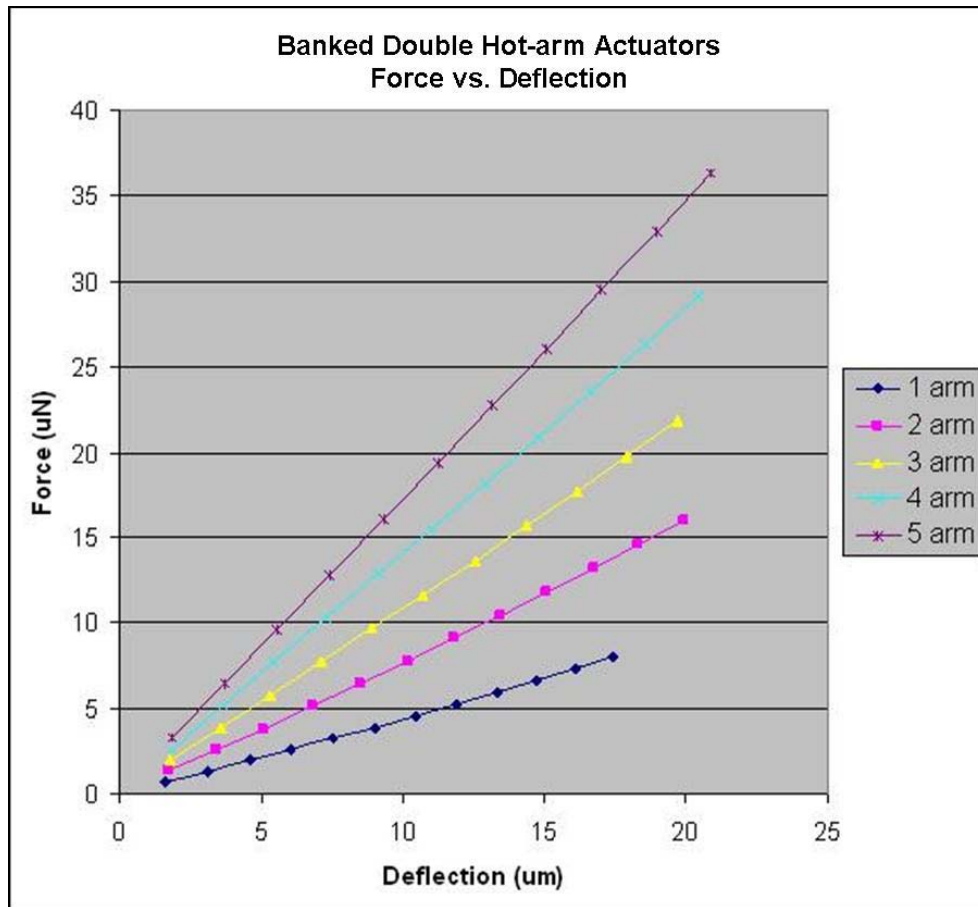


**Figure 4-9:** Force vs. deflection curve for 1-5 banked electro-thermal actuators. [16]

Because the actuation scheme in this effort calls for repeatability to rotate gear wheels to move the microshutter flaps, the coupled actuators will be studied at 10 volts rather than 15 volts so as to prevent device failure. Table 4-3 delineates the power requirements, force available, and deflection available when the coupled hot-arms are given a 10-volt input.

**Table 4-3:** Comparison of coupled actuator devices.

	Applied Voltage	Current	Power	Force	Deflection
2 Hot-arm Pawl Device	10 V	12.6 mA	126.3 mW	8.5 $\mu\text{N}$	9.19 $\mu\text{m}$
4 Hot-arm Drive Device	10 V	35.6 mA	355.7 mW	11.8 $\mu\text{N}$	8.16 $\mu\text{m}$

An important characteristic to note is the melting point of polysilicon; the point of failure for these actuators typically results from overheating of the hot-arms, causing them to melt and thus either disconnect or short out completely. Figure 4-10 shows at which voltage and deflection these two actuators are expected to reach this point of failure; one must be careful not to overstep these bounds when actuation testing or failure of the devices is imminent. For each of these devices, those failure points exist where the input voltage is approximately 12 volts; this translates to a deflection of approximately 11  $\mu\text{m}$  for the 4-actuator drive device, and approximately 13  $\mu\text{m}$  for the 2-actuator pawl device.

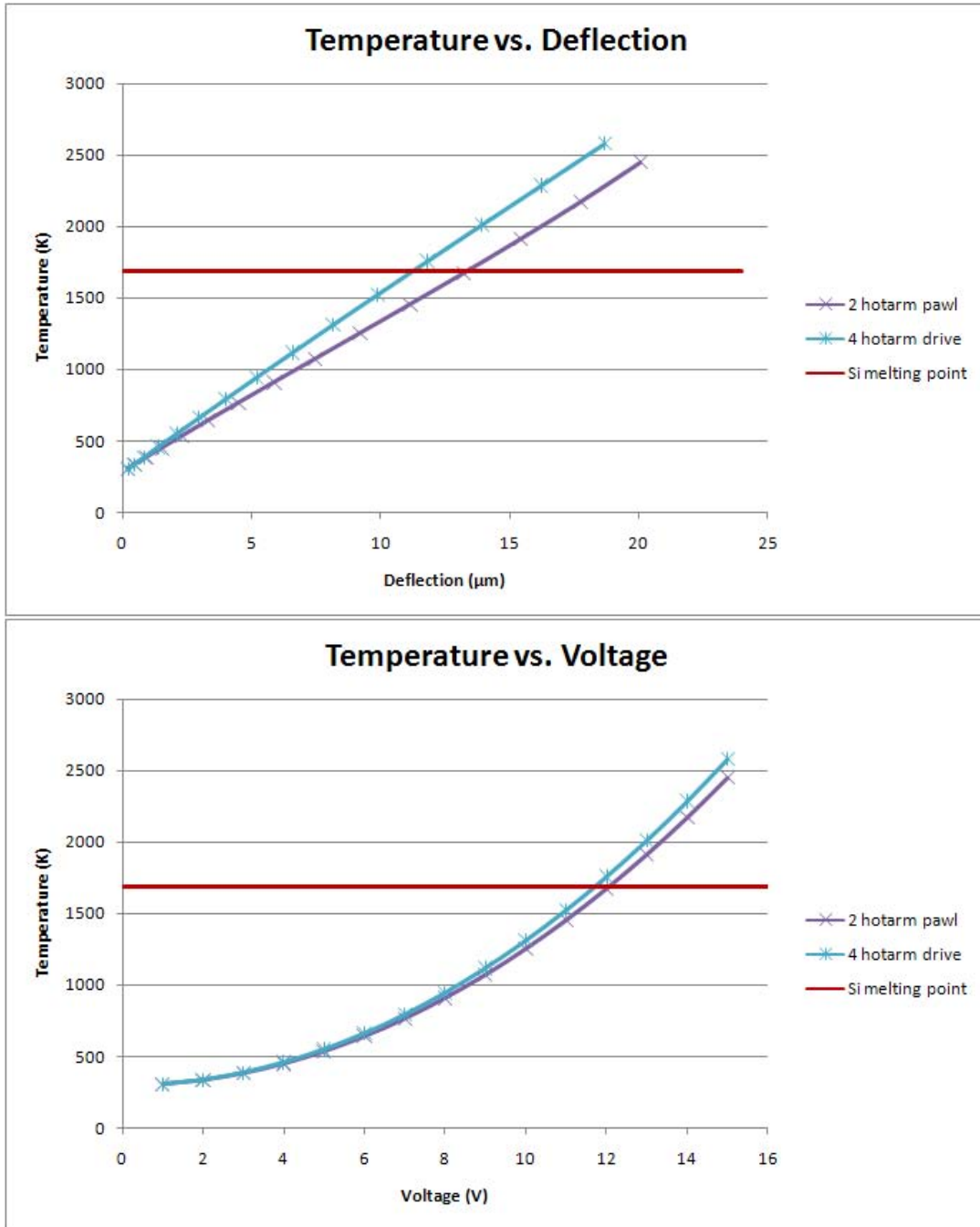


**Figure 4-10:** Temperature charts depicting how the temperature of the electro-thermal actuators increases with deflection and voltage. The red horizontal line represents the melting point of polysilicon; failure points of the devices lie where this line intersects the curves.



### 4.3 Two-Dimensional Electro-Thermal Gear Actuator

While the two banked actuators discussed in the previous section provide actuation in one direction, this is not useful for the two-dimensional actuation required to move the flaps either directly or indirectly through a gear mechanism. This two-dimensional actuation can be achieved by physically connecting the pawl and drive devices; this was illustrated in Figure 3-9. Unlike in Figure 3-9, however, the physical joining actually provides an advantage for this design; previous tests have shown that the pawl device has a tendency to slip either above or below the drive device particularly when high frequencies are involved, and the combining of these two devices eliminates that possibility [16]. Figure 4-11 illustrates how the two are connected.

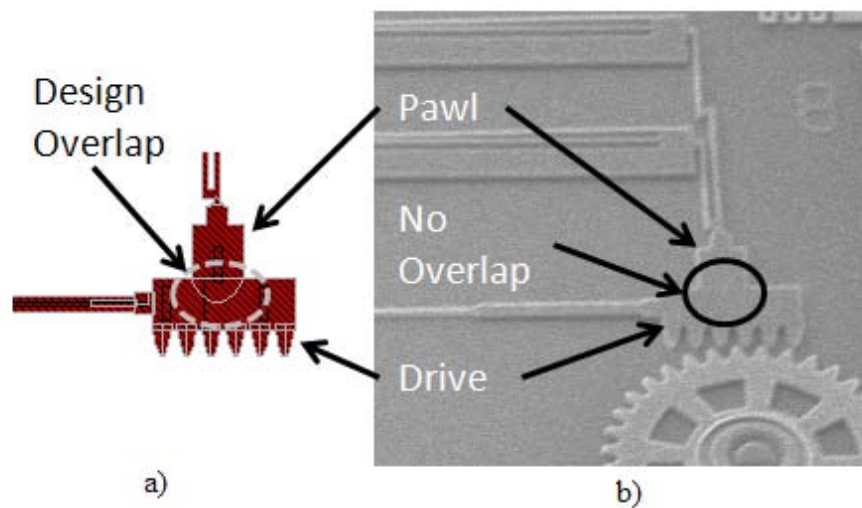


**Figure 4-11:** a) L-Edit design of combined pawl and drive device; while the design shows the original design of the pawl as it is combined with the drive, b) shows that no physical overlapping takes place.

A CoventorWare® analysis of this device simulated this combined actuator and predicted its movement with input forces varying between 1 and 8 volts. Table 4-4 lists

how the steps in CoventorWare® were calculated with the input voltage through both the pawl and drive actuator components.

**Table 4-4:** CoventorWare® steps and their corresponding input voltages for simulating the gear actuator.

	Step 1	Step 2	Step 3	Step 4	Step 5	Step 6	Step 7	Step 8
Drive—4 actuators	1 V	4 V	8 V	8 V	8 V	4 V	1 V	1 V
Pawl—2 actuators	1 V	1 V	1 V	4 V	8 V	8 V	8 V	4 V

While operation of the gear actuator would ideally use an AC signal, it was not immediately apparent that CoventorWare® could apply such a signal and achieve viable results, thus the 8-step process was chosen to model the gear actuator. According to the CoventorWare® results, the gear and pawl device can achieve a maximum vertical deflection (pawl) of approximately 9  $\mu\text{m}$  and a maximum horizontal deflection (drive) of approximately 3.5  $\mu\text{m}$ . This is illustrated in Figure 4-12.

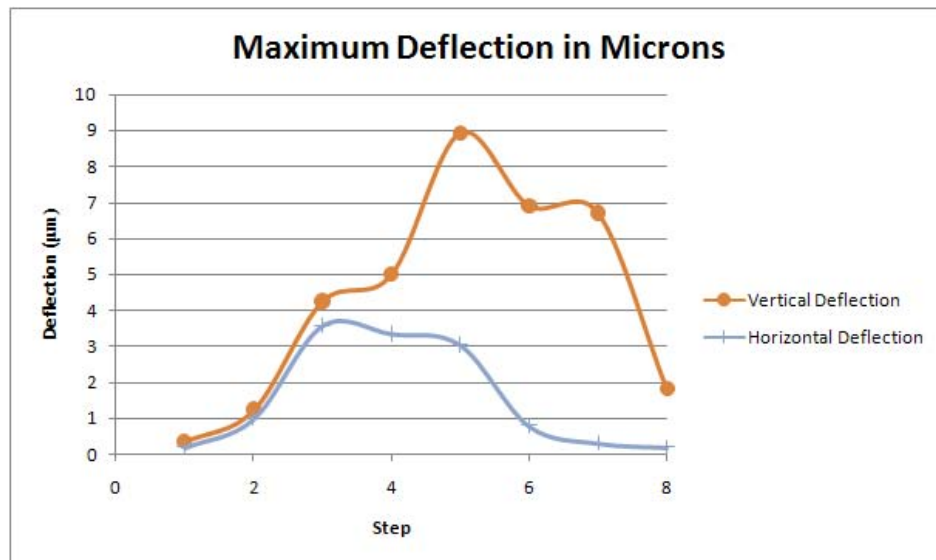


**Figure 4-12:** Chart of deflections achieved with the gear actuator in both horizontal and vertical directions.

CoventorWare®'s Visualizer provided useful insight as to where exactly these deflections would occur as well as the amount of curvature the pawl and drive device can undergo. Figure 4-13 shows the difference in the entire gear actuator between steps 1 and 5 to highlight the deflection when the input voltages are at their maximum and also when they are at a minimum. Figure 4-14 demonstrates the pawl and drive device going through the motion of a full cycle of actuation. Unfortunately, simulating contact between the gear actuator and the gear wheel was unlikely at best due to the large amount of friction coefficients CoventorWare® requires from the user, so that was omitted from this simulation. Figure 4-15 delineates exactly how much power is required to run the gear at each step of the simulation as well as the total deflections at those steps.

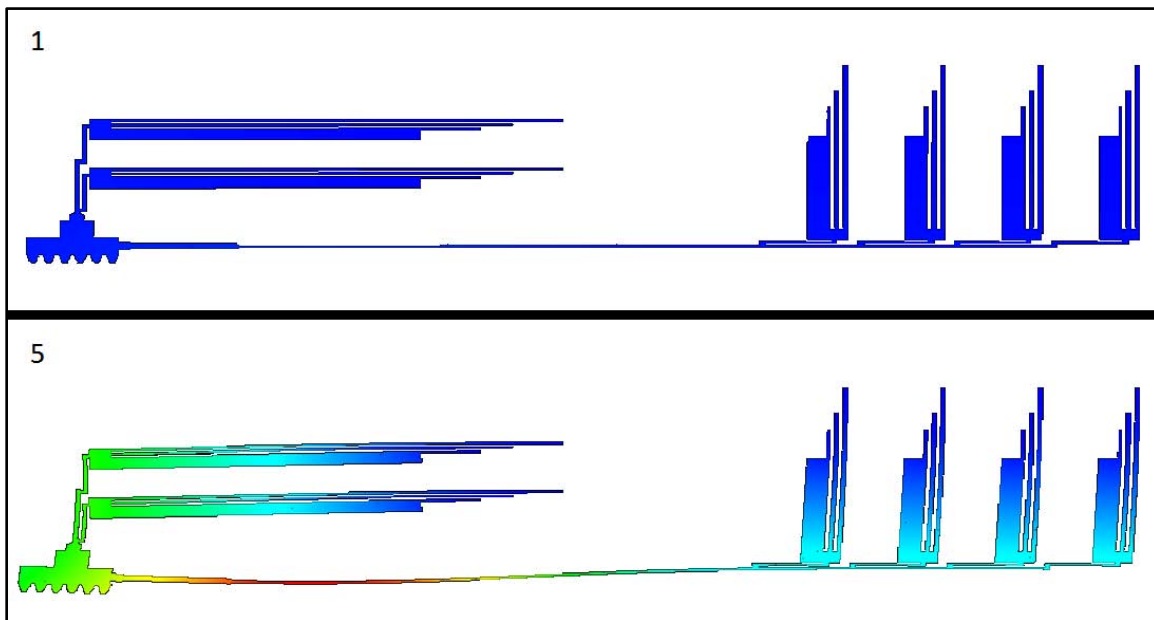


**Figure 4-13:** Comparison between step 1 and step 5 for the gear actuator. Step 1 represents when all inputs are at a minimum of 1 volt. Step 5 represents when all inputs are at a maximum of 8 volts; this is easily seen by the curvature in all six hot-arms as well as the tilting of the gear and pawl device and the bending of the driving arm in the horizontal direction.

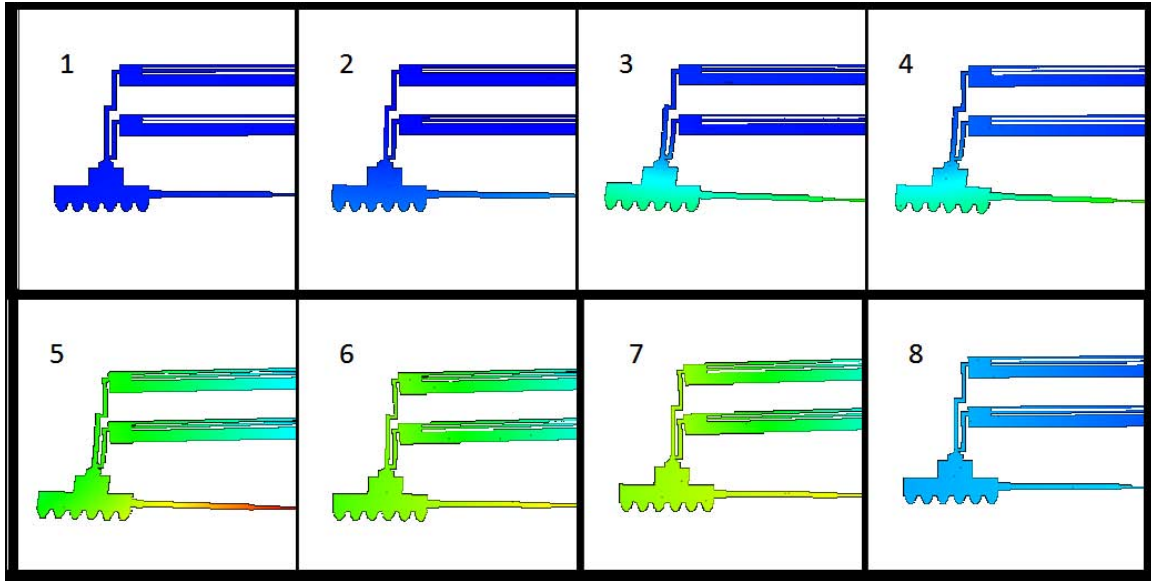


**Figure 4-14:** Illustration of the 8 steps modeled in CoventorWare® for the gear actuator.

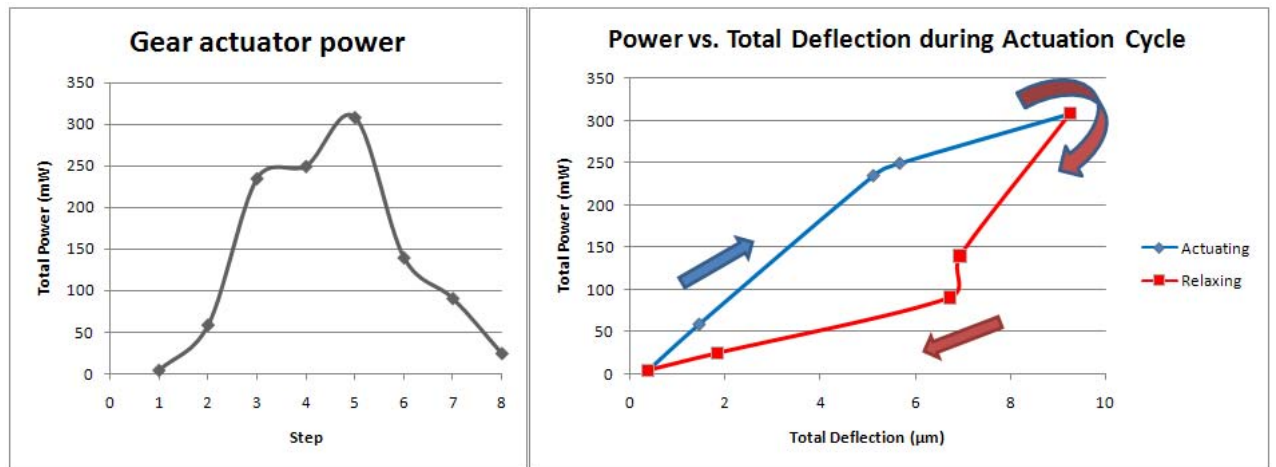


**Figure 4-15:** Charts illustrating the total power required to drive the gear actuator and how much deflection can be expected.

Clearly, this demonstrates that the gear actuator operates as designed—in a circular motion and with enough deflection that it should be able to rotate a gear wheel. The gear actuator has the added benefit of low power requirements. While power

requirements are not usually a factor in functionality within the confines of a laboratory, they play a much larger role during operational testing.

#### 4.4 Optical Modeling

Of course, functionality of the device is moot if the device fails due to overheating from incident light exposure. Fortunately, previous research at AFIT studied the optical properties of the phosphorus-doped polysilicon available through the PolyMUMPS™ process to determine exactly how much of the irradiance on the surface of the device would be converted to heat. Denninghoff [19] studied optical absorption for polysilicon for the purpose of using the heat generated to actuate devices; while any heat generated in this effort would not be used for actuation, it is prudent to study nonetheless for its long-term effects on the microshutter array. His work will be recalculated to apply to the wavelength and polysilicon layers being used for this research. Another dissertation at AFIT also used Raman spectroscopy to measure stress increases when MEMS cantilevers are illuminated with a laser; as an increase in temperature correlates to an increase in compressive stress, this analysis will also be used to determine potential temperature increases [20].

The first step in analyzing polysilicon's optical response to an irradiance is remembering Kirchoff's Law of energy conservation:  $\Phi_{\text{incident}} = \Phi_{\text{absorbed}} + \Phi_{\text{transmitted}} + \Phi_{\text{reflected}}$ , where  $\Phi$  represents flux [21]. If both sides of the equation is divided by  $\Phi_{\text{incident}}$ , Kirchoff's Law is then reduced to

$$1 = a + \tau + \rho \quad (4.1)$$

where  $a$  is the absorptance,  $\tau$  is the transmittance, and  $\rho$  is the reflectance of the material receiving the irradiance [21]. In order to calculate exactly how much of the irradiance will be converted into heat, Denninghoff used the following equations, which result in a final percentage of the incoming flux:

$$\Phi_0 = \Phi_i (1 - \rho) \quad (4.2)$$

$$\Phi(t_0) = \Phi_0 [1 - e^{-\alpha t_0}] \quad (4.3)$$

$$\Phi_{heat} = \Phi(t_0) \frac{h\nu - E_g}{h\nu} \quad (4.4)$$

where, again,  $\rho$  is reflectance,  $\alpha$  is the absorption coefficient in  $\text{cm}^{-1}$ ,  $t_0$  is the thickness of the material being irradiated,  $h$  is Planck's constant at  $6.626 \times 10^{-34}$  J-s,  $\nu$  is the frequency of light, and  $E_g$  is the bandgap of the material [19]. In this case, the bandgap of both Poly1 and Poly2 is 1.12 eV, and a  $\lambda$  equal to 632.8 nm corresponds to an  $h\nu$  equal to 1.96 eV. Because  $\rho$  and  $\alpha$  are experimentally determined, they will be approximated using Figure 4-16. As in the top chart, phosphorus-doped polysilicon at 632.8 nm registers  $\alpha$  at approximately  $9 \times 10^3 \text{ cm}^{-1}$ . The bottom chart shows no experimental data for reflectance when incidence is below 20 degrees from normal; a safe estimate for  $\rho$  would be 0.2 if the data trend were to continue towards normal.

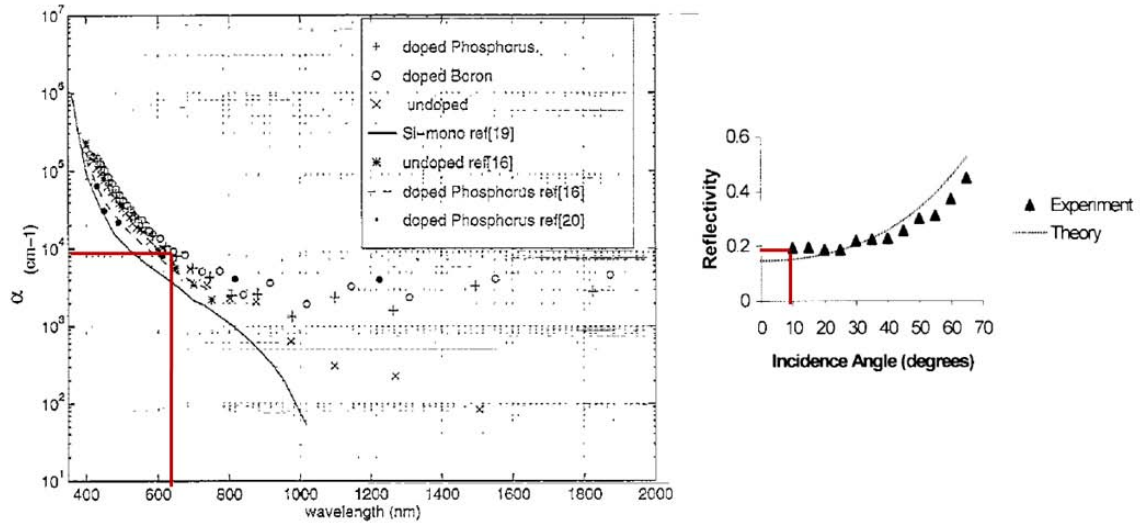


**Figure 4-16:** Experimental data that provides  $\alpha$  and  $\rho$  coefficients. At 632.8 nm,  $\alpha$  is  $9 \times 10^3 \text{ cm}^{-1}$  [22], and  $\rho$  is 0.2 [23].

Calculating the absorption of both Poly1 and Poly2 is simple given the parameters in Table 4-5. Table 4-6 then takes these parameters and inserts them into each statement from Equations 4.2-4.4 that builds upon the result of the previous equation. The total heat conversion from an incoming flux is then calculated to be 28.6% for the Poly1 layer and 25.4% for the Poly2 layer.

**Table 4-5:** Parameters for determining optical absorption for the Poly1 and Poly2 layers.

	$\rho$	$\lambda$	$t_0$	$\alpha$	$E_g$
Poly1	0.2	632.8 nm	2.0 $\mu\text{m}$	$9 \times 10^3$	1.12 eV
Poly2	0.2	632.8 nm	1.5 $\mu\text{m}$	$9 \times 10^3$	1.12 eV

**Table 4-6:** Calculations to determine absorptance and heat conversion for Poly1 and 2. These results are a worst-case scenario.

	$1-\rho$	$1-\exp(-\alpha t_0)$	$\frac{h\nu - E_g}{h\nu}$	<i>Total Absorption</i>	<i>Total Heat Conversion</i>
Poly1	80.0%	83.5%	42.8%	66.8%	28.6%
Poly2	80.0%	74.1%	42.8%	59.3%	25.4%

These calculations show that polysilicon is a relatively good choice for an optical microshutter; not only does it transmit less than 20% of its irradiance, but it is fairly resilient to an outside heat source. This characteristic will be advantageous later when determining the amount of deflection caused by external radiation. A CoventorWare® analysis simulated the deflection caused by a rising temperature on the Poly2 layer of the microshutters to see if the deflection was large enough to cause functional problems in the operation of the microshutter. An image from this simulation is shown in Figure 4-17.

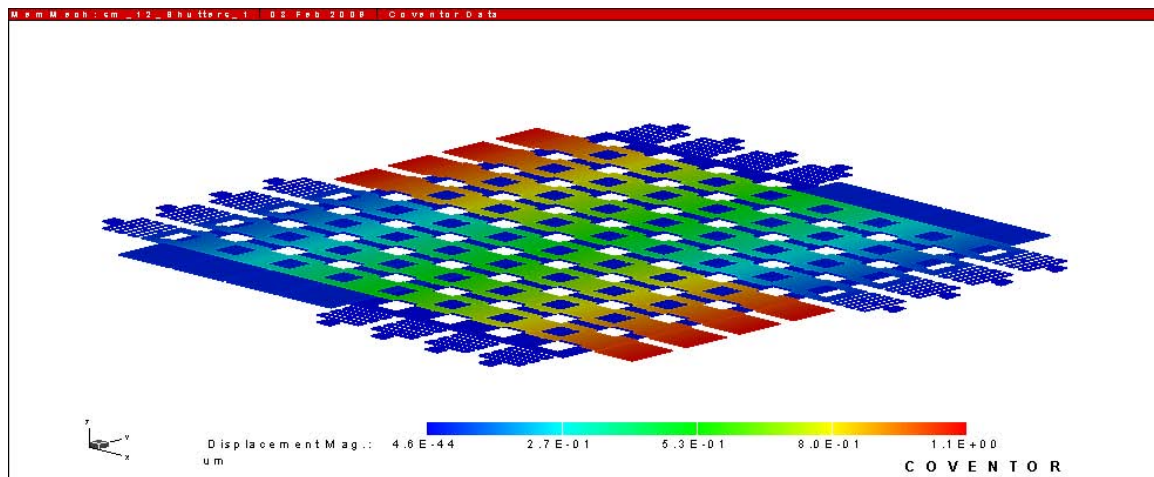


**Figure 4-17:** Simulated image from CoventorWare® detailing the deflection of the microshutter array when the Poly2 layer has been heated to 1400K. The maximum deflection is seen near the ends of the shutter flaps and measures only 1  $\mu\text{m}$  upwards.



Even when the Poly2 layer has been heated to near melting, the anchor points on the shutters act as heat sinks and keep the overall upward deflection of the shutter array to a minimum. In order to calculate exactly how much power would be needed to melt the microshutter array, a few more equations are needed to determine exactly how the polysilicon in the microshutter array disperses heat.

First, each shutter flap can be modeled as a fixed-fixed beam using the equivalent thermal circuit shown in Figure 4-18. Even though the shutters are not fixed at both ends, the dimple on the shutter flap at the opposite end of the spring will serve as the other anchor in this case. These are assumed to be on an infinite heat sink for ease of calculations as silicon nitride has a heat capacity very similar to that of polysilicon. The majority of the heat will be conducted to the substrate through the beam, designated  $G_b$ , while some will be conducted through the air beneath the beam, designated  $G_g$  [20]. To complete the circuit,  $C_b$  represents the thermal capacity of the beam,  $I_b$  represents the power into the system,  $T_b$  is the temperature of the beam, and  $T_s$  is the temperature of the substrate [20].

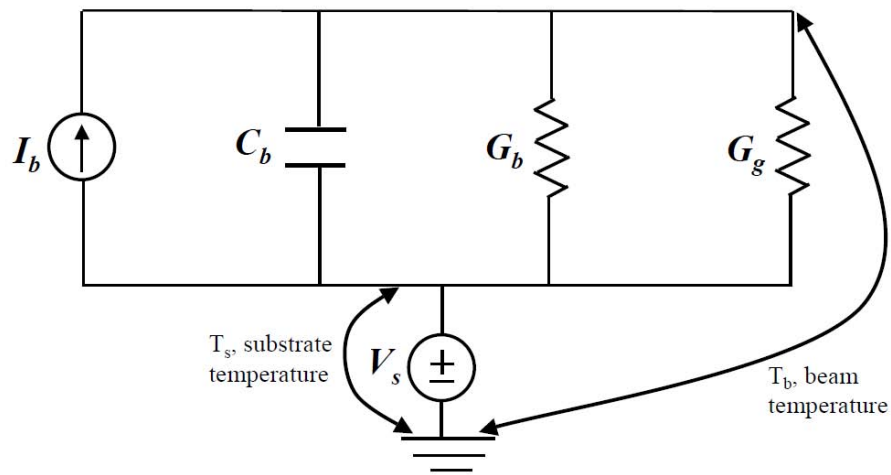


**Figure 4-18:** Representative thermal circuit for a fixed-fixed polysilicon beam. [20]

In order to evaluate the above circuit, the following equations are given to determine  $I_b$ ,  $C_b$ ,  $G_b$ , and  $G_g$ :

$$I_b = P_0 (1 - \rho) \quad (4.5)$$

$$C_b = \rho_b C_p w t l \quad (4.6)$$

$$G_b = \frac{N_{poly} w t}{l} \quad (4.7)$$

$$G_g = \frac{F_s N_{poly} w l}{h_s} \quad (4.8)$$

where  $P_o$  is the optical power not reflected by the shutter flap,  $\rho$  is the reflectance of the flap,  $\rho_b$  is the density of polysilicon,  $C_p$  is the thermal capacity of polysilicon,  $N_{poly}$  and  $N_{air}$  are the thermal conductivities of polysilicon and air,  $F_s$  is a unitless shape factor that accounts for fringing heat flux effects, and  $w$ ,  $t$ ,  $l$ , and  $h_s$  correspond to the width, thickness, length, and height of each beam respectively [20]. Because each shutter flap has a relatively complex geometry compared to a flat polysilicon beam, weighted averages were used for both the width and height of each beam to simplify calculations. The values for the physical constants used in this analysis are given in Table 4-7.

**Table 4-7:** Physical parameters for thermal equations [20]

Parameter	Value	Description
$h_s$	2.0 $\mu\text{m}$ (Poly1) 1.07 $\mu\text{m}$ (Poly2)	Weighted average elevation above next physical layer
$w$	32.2 $\mu\text{m}$ (Poly1), 22.2 $\mu\text{m}$ (Poly2)	Weighted average width of shutter flap
$C_p$	$7.54 \times 10^2 \text{ J/(kg-K)}$	Heat capacity of polysilicon
$\rho_b$	$2.33 \times 10^3 \text{ kg/m}^3$	Density of polysilicon
$N_{air}$	30 W/(m K)	Thermal conductivity of air
$N_{poly}$	0.02 W/(m K)	Thermal conductivity of polysilicon

To find the weighted values for the width of each shutter flap, the top surface area was first measured from the L-Edit design software. Knowing that the shutter flaps were 381  $\mu\text{m}$  long, the width was then determined to be an average 33.2  $\mu\text{m}$  for the Poly1 flaps and 22.2  $\mu\text{m}$  for the Poly2 flaps. The height value for Poly1 was unchanged from the given 2.0  $\mu\text{m}$  as there were no physical layers underneath it besides the nitride layer. For the Poly2 flap, 320  $\mu\text{m}$  of the flap is above one of the Poly1 flaps, signifying a 0.75  $\mu\text{m}$  gap, while 61  $\mu\text{m}$  is above the nitride layer, which is a 2.75  $\mu\text{m}$  gap. A simple weighted mean calculation resulted in a 1.07  $\mu\text{m}$  average height for the Poly2 flap.

Typically, the  $F_s$  shape factor incorporates time-consuming numerical methods when dealing with any shape other than a rectangular beam. To save on time and calculations, each of the shutter flaps was mathematically averaged over width and height to result in a uniform rectangular beam.  $F_s$  is then found by

$$F_s = \frac{t}{w} \left( \frac{2h_s}{t} + 1 \right) + 1 \quad (4.9)$$

where again  $w$ ,  $t$ , and  $h_s$  correspond to the width, thickness, and height of each beam respectively [20]. For a Poly1 shutter flap, this value is 1.18, and for a Poly2 shutter flap, the value is 1.16. Using this shape factor with analysis from the thermal circuit model in Figure 4-18, the temperature rise in a shutter flap is given by

$$T_b = P_o (1 - \rho) Z \quad (4.10)$$

where  $T_b$  is the increase in flap temperature, and  $Z$ , the equivalent thermal impedance, is given by

$$Z = \frac{1}{\sqrt{(G_g + G_b)^2 + \frac{C_b^2}{\tau_{th}^2}}} \quad (4.11)$$

where  $C_b$ ,  $G_b$ , and  $G_g$  are the values calculated in Equations 4.6-4.8 [20]. The thermal time constant for polysilicon,  $\tau_{th}$ , is simply  $C_b/(G_b + G_g)$  and balances the storage of heat within the shutter flaps and the dissipation of heat through the anchor points [21]. Given an incident laser power of 1.5 mW on the shutter array, this results in a 3.29 K increase for the Poly2 shutter flaps and a 1.82 K increase for the Poly1 shutter flaps. If the shutters were to be heated to the melting point of polysilicon, which is 1687 K, then 633 mW would need to be incident to melt the Poly2 flaps, and 1.15 W would be needed to melt the Poly1 flaps. As a 1.5 mW laser will be used for testing, failure due to laser exposure is not expected.

#### 4.5 Chapter Summary

The data introduced in this chapter demonstrated the most efficient use of an electro-thermal actuator and how to achieve the most deflection with its use. Simulations revealed that a polysilicon wedge shutter can open and reveal a 33- $\mu\text{m}$  aperture in the case of the sixth-wedge or a 47- $\mu\text{m}$  aperture in the case of the quarter-wedge. The actuation scheme for the microshutter array was also studied at length to fully comprehend its functionality and whether it will properly operate the microshutter array; simulations revealed that the gear and pawl device will move in a circular motion to provide up to 10  $\mu\text{m}$  of deflection in order to rotate a gear wheel. Optical absorption was studied to grasp if Poly1 and Poly2 will sustain a prolonged exposure to an external

irradiance; it was determined that not only will these layers endure an irradiance, but they will do so with very little upward deflection. These results will all be experimentally tested in the next chapter.

## 5. Results

In Chapter 3, possible designs and layouts were explored regarding both individual microshutters and an 8x8 microshutter array. An actuation scheme was also designed for the purpose of operating the microshutter array. These designs were further studied and modeled in depth in Chapter 4 in order to broaden understanding of their functionality, strengths, and weaknesses. This chapter will discuss how the fabricated microshutters, microshutter array, and actuation scheme compared to the modeled results seen in the previous chapter. This chapter will also experimentally test the aluminum microshutters that were fabricated by AFRL and explore their usefulness and application to this project. Finally, this chapter will conclude with optical testing to see how polysilicon reacts to a constant irradiance from a low-power HeNe laser and if the absorptance ( $a$ ), transmittance ( $\tau$ ), and reflectance ( $\rho$ ) coefficients for the microshutter array as a whole produced from this experiment mirror those found in Chapter 4.

### 5.1 Fabrication Results

As mentioned before in Section 2.3, the PolyMUMPS™ process was chosen for fabrication due to its relatively low cost and quick turnaround time of approximately two months. Unfortunately, the PolyMUMPS™ process also has its drawbacks. Its tolerances for alignment throughout the fabrication process dictate at least a minimum of 2  $\mu\text{m}$  spacing between all devices; however, 2  $\mu\text{m}$  is still large enough of an aperture to permit light to pass and is not acceptable for fully functional microshutters. PolyMUMPS™ is also a conformal process, meaning that the Poly2 layer follows the

shape of the Poly1 layer beneath it. The following subsections will outline where these drawbacks to the PolyMUMPS™ process caused component failure.

### 5.1.1 PolyMUMPS™ Run 83 Fabrication Results

Run 83 was the first attempt at fabrication through the PolyMUMPS™ process, and all of the designs from this run were based off adding wedges to the ends of electro-thermal actuators. Three of the designs were presented in Chapter 3, and two others were similar in that they used a double hot-arm electro-thermal actuator, but with a slightly different geometry.

The first detail noticed when examining these shutters under a microscope is that etch lines between the individual wedges appear to be nonexistent. Upon further scrutinization of the designs through an SEM, all the shutters were indeed found to be fused. Figure 5-1 shows the SEM images taken of each of the shutters and highlights the fused areas of each.

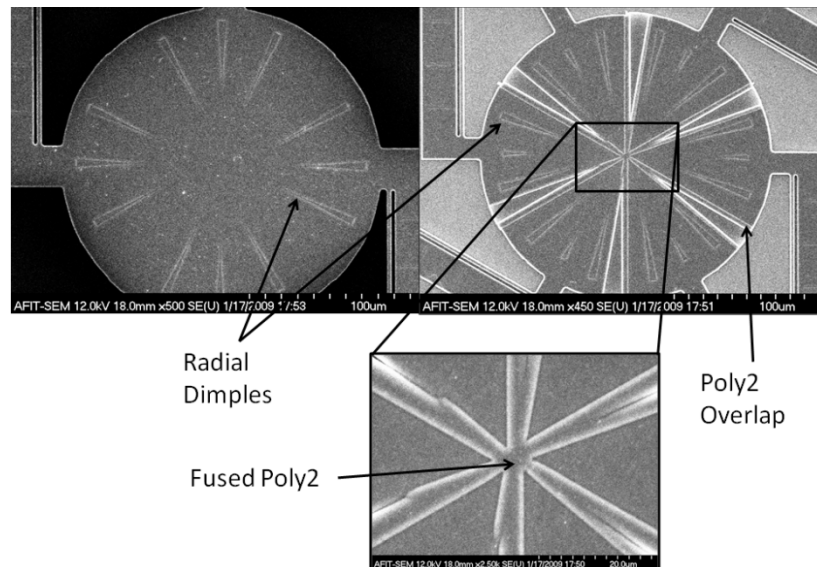


**Figure 5-1:** SEM pictures showing both the quarter wedge and sixth wedge shutter with wedges fused.

Because every shutter was fused, no shutter testing could be performed outside the CoventorWare® analysis presented in Chapter 4. However, if the reason for the fusing is uncovered, then future work can account for this to achieve a functioning wedge shutter. Figure 5-2 is a magnification of the center of the quarter wedge shutter with its spacing clearly marked. The design rules for the PolyMUMPS™ handbook state that the minimum spacing between both Poly1 and Poly2 layers is  $2\text{ }\mu\text{m}$  [14]. As shown in Figure 5-2, the spaces between the wedges is  $0.25\text{ }\mu\text{m}$  smaller than the minimum spacing called for in the PolyMUMPS™ design rules [14], which could possibly be the reason for the fusing of these shutters.

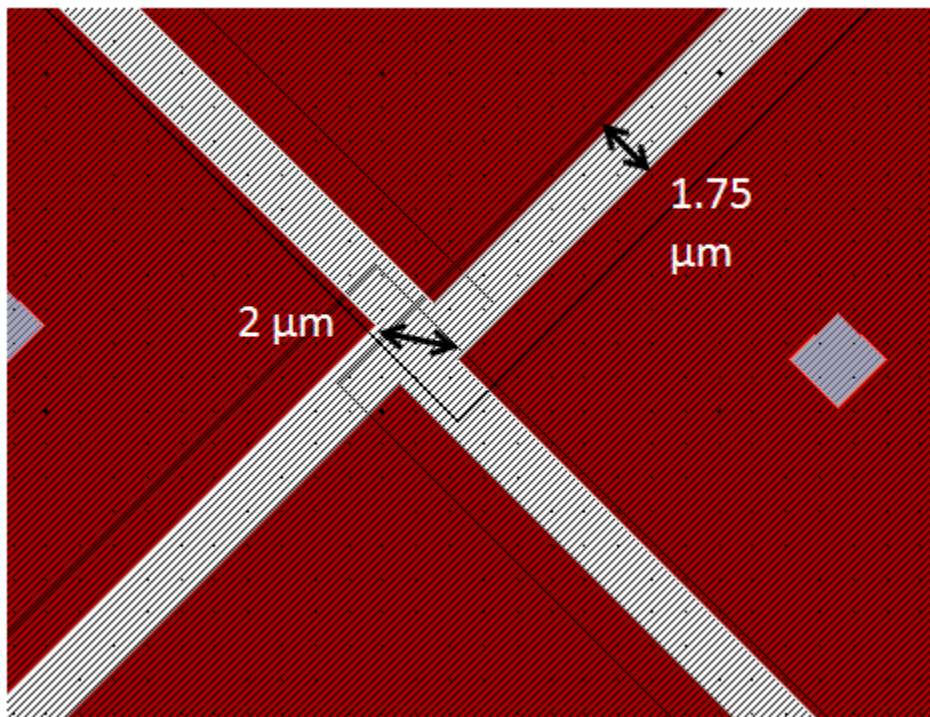


**Figure 5-2:** Magnification of quarter-wedge shutter highlighting spaces between wedges in the original design. The actual spacing between the wedges is  $0.25\text{ }\mu\text{m}$  smaller than the minimum spacing called for by the design rules [14].



However, in the case of the sixth-wedge shutters, the design rules were followed, as demonstrated in Figure 5-3. The only conclusion that can be drawn from this scenario is that the design rules for PolyMUMPS™ themselves are somewhat presumptuous in their tolerances; this essentially closes any possibilities of fully closing wedge shutters.

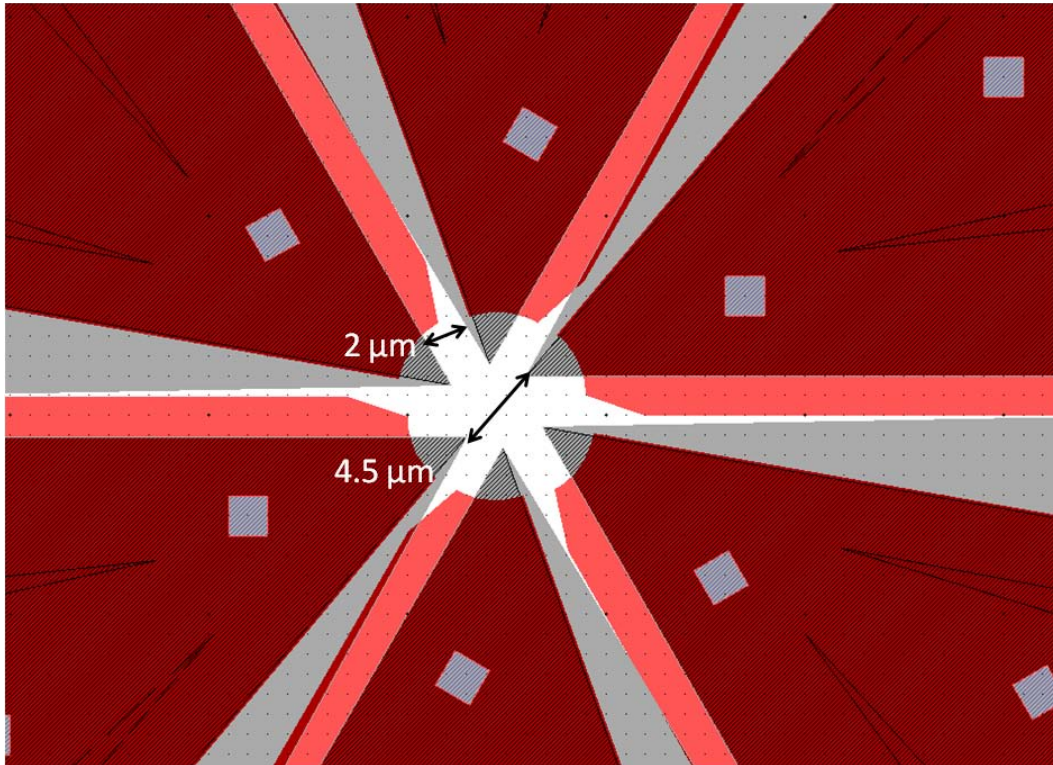


**Figure 5-3:** Magnification of sixth-wedge shutter highlighting spaces between wedges in the original design.

Fortunately, individual wedges and electro-thermal actuators were also included with the design, so the individual wedge from each of these designs was actuated and characterized; these results can be seen in Figure 5-4. Despite the fusing of the shutters, this demonstrates that wedge shutters are possible through PolyMUMPS™ as long as the design rules for spacing are followed with an extra tolerance.

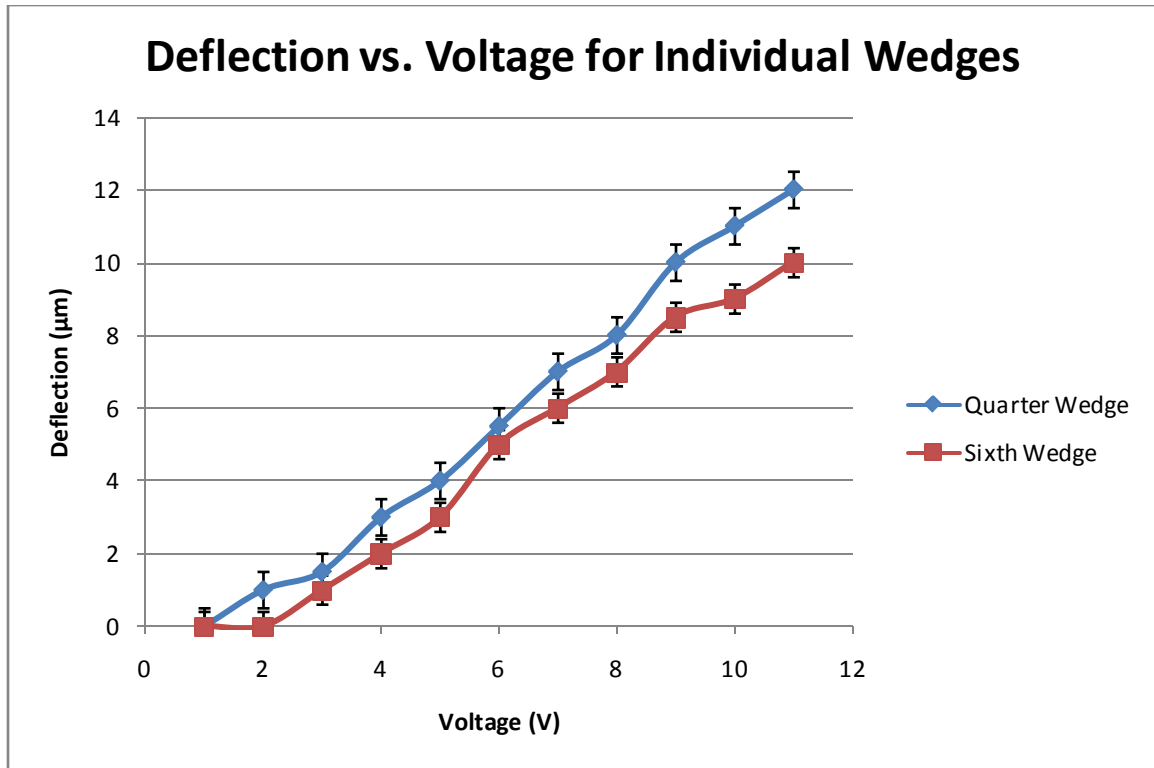


**Figure 5-4:** Deflection vs. voltage curves for an individual wedge from both the quarter-wedge and sixth-wedge shutters. The smaller deflections for the sixth wedge result from shorter electro-thermal actuators.

### 5.1.2 PolyMUMPS™ Run 84 Fabrication Results

Run 84 was the final PolyMUMPS™ attempt for fabrication due to changes within the foundry's schedule. This run included the full microshutter array as well as extra gear actuators and shutter flaps for additional testing. While this run did not have the previous error of fusing, numerous other problems were encountered during the testing of these fabricated designs.

While the tests of the gear actuators proved that they do deflect as intended, issues were encountered in translating those deflections into rotations in the gear wheels. In an ideal actuation scheme, these actuators would be driven by two separate AC signals that

are 90 degrees out of phase and amplified by a DC voltage. However, when the gear actuators were fed these two signals, the pawl and drive device would only actuate in one direction, not the two-dimensional circular motion needed to drive the gear wheel that was presented in Chapter 4. In trying to simplify the input voltages and achieve actuation, the gear actuator received the same DC inputs that were listed in Table 4-4. Circular motion was achieved with these DC inputs; however, that motion could not provide enough force to rotate the gear wheels. In an attempt to gain force, voltages were increased, but no rotation was achieved before the electro-thermal actuators failed from overheating; this failure caused the hot-arm to physically break from its contact pad. Figure 5-5 shows both aspects of the gear actuator after failure.

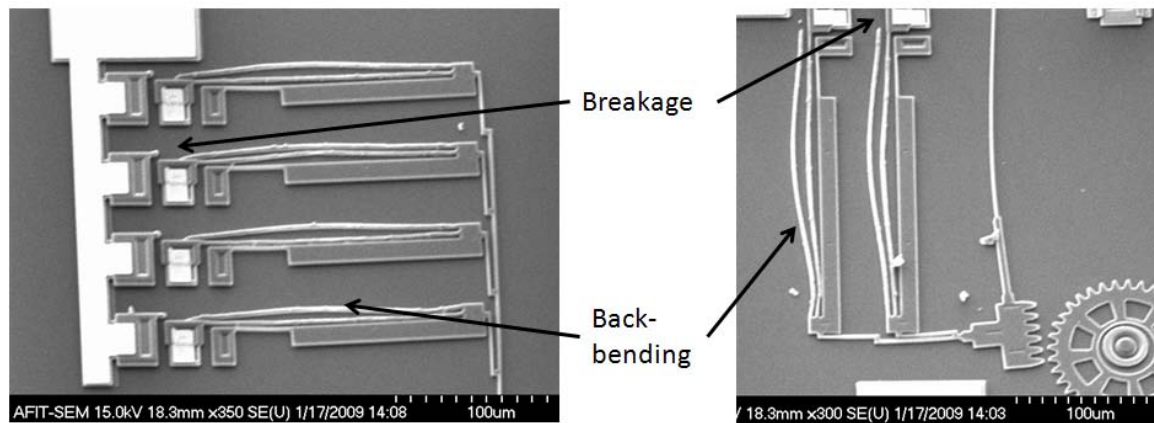


**Figure 5-5:** Both the drive- and pawl- banked actuators after actuation failure. Both back-bending, or plastic deformation, was observed, as well as breakage of the hot-arms in both cases.

Another key failure point for this fabrication run was discovered within the microshutter array itself. As mentioned in Section 3.2.1, the conformal nature of the PolyMUMPS™ process could cause problems during actuation due to interlocking between the Poly1 and Poly2 layers. Unfortunately, this problem was realized in two

aspects of the microshutter array. First, the widening of the Poly1 flaps provided no advantages to the operation of the array; Figure 5-6 displays how the Poly2 layer conformed to the Poly1 layer beneath it; this prevented any movement from the Poly2 flaps. In addition, the design required near-perfect alignment during fabrication due to the shape and strength requirements for the Poly2 shutter flaps. This alignment caused the Poly2 layer to fill in the Poly1 holes on one side, shown in Figure 5-6, thus preventing the Poly1 flaps from moving as well.

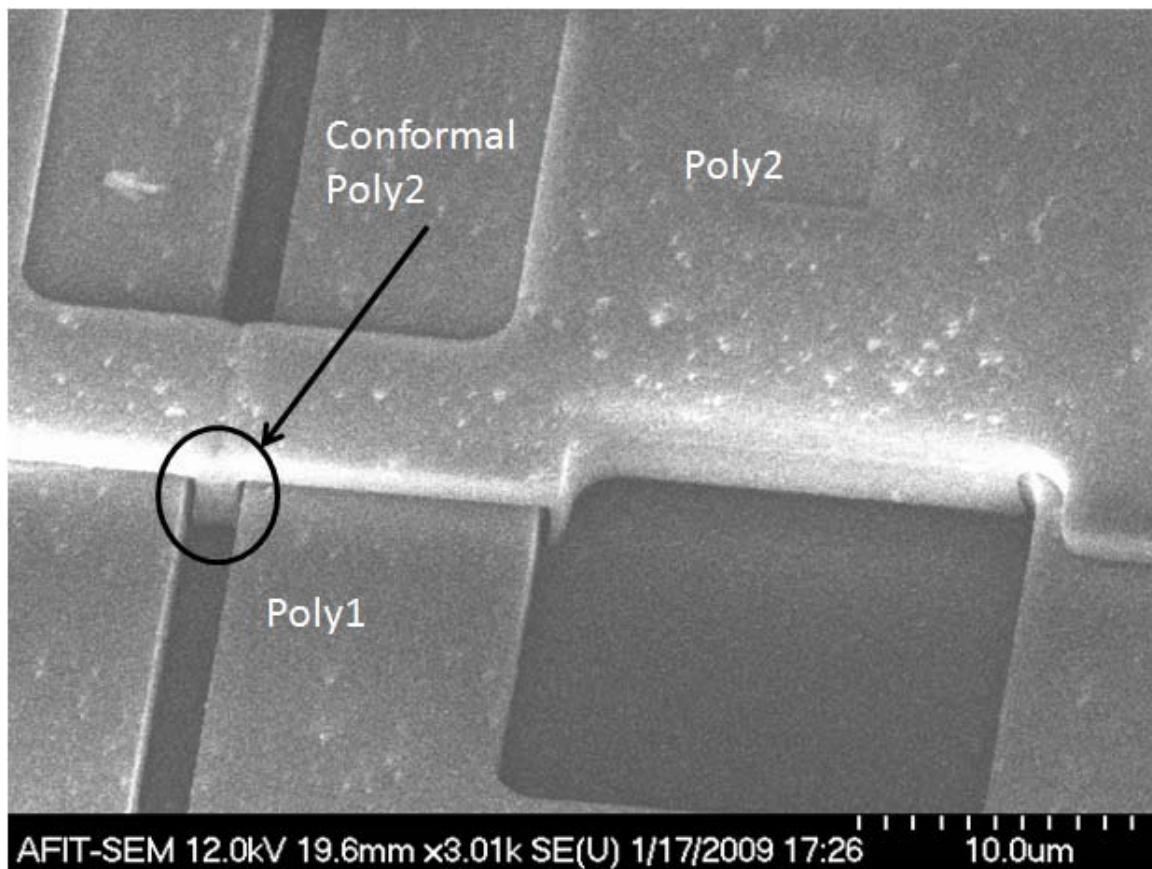


**Figure 5-6:** SEM image of the Poly2 shutter flap conforming to the Poly1 layer beneath it. These small conformal dips, while no deeper than 2  $\mu\text{m}$ , prevented the Poly2 shutter flaps from moving.

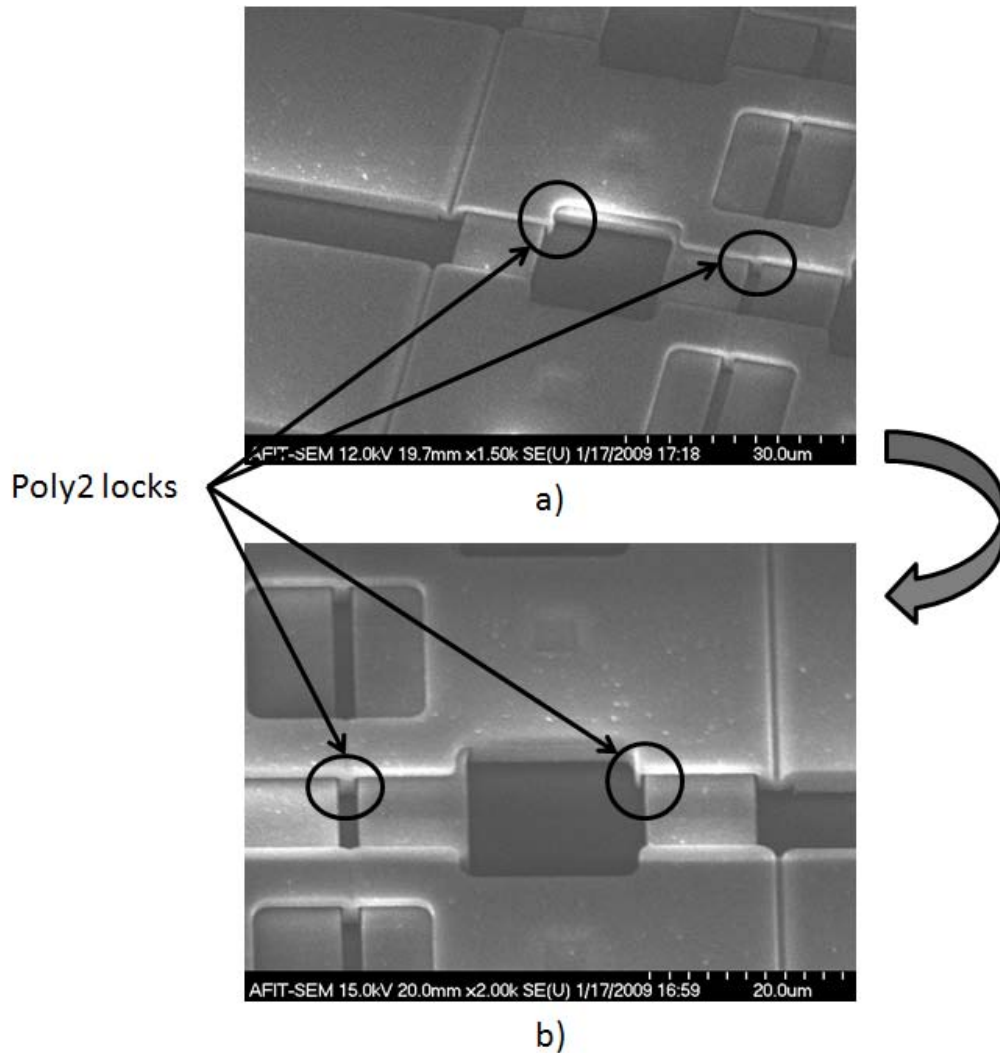


**Figure 5-7:** a) SEM image of one side of an aperture in the Poly1 shutter flap. There is very little Poly2 filling in the hole on this side. b) SEM image of the other side of the same aperture. The Poly2 has filled the hole slightly on this side, preventing the Poly1 shutter flap from moving. In both images, the Poly2 dips between Poly1 flaps have been marked.

While a solution to the conforming problem of the microshutter array is not readily apparent, a possible solution to make the gear actuators more efficient exists. In attempting to ensure that the gear teeth of both the shutter flaps and the drive and pawl device were not fused as in Run 83, the teeth of the drive and pawl devices were placed

3  $\mu\text{m}$  away from the teeth of the shutter flaps. While this ensured that fusing did not occur, this also reduced the contact area between the gear teeth, which may have contributed to the lack of rotation of the gear wheel. Optimization of the gear placement should correct this for future studies.

## **5.2 AFRL Quartz Wafer Results**

In addition to the two PolyMUMPS<sup>TM</sup> runs discussed in the previous section, microshutters fabricated on a quartz wafer at AFRL were also tested for functionality. On these wafers, quarter-wedge shutters of varying sizes ranging from 100  $\mu\text{m}$  to 400  $\mu\text{m}$  in diameter were fabricated with 2  $\mu\text{m}$  of aluminum; this was chosen primarily for its accessibility and higher coefficient of thermal expansion. Quartz wafers were used for their ability to pass both visible and IR light, thus eliminating the need to etch a physical aperture through the substrate.

Due to internal stress stemming from either the CO<sub>2</sub> critical drying process or the deposition of the aluminum itself, most wedges from the 200- $\mu\text{m}$ , 300- $\mu\text{m}$  and 400- $\mu\text{m}$  diameter microshutters were physically bent out of plane of the substrate, rendering testing impossible; those that were not bent upwards succumbed to stiction and were immovable. Fortunately, some wedges from the 100- $\mu\text{m}$  aperture survived the release and were tested for their functionality. Figure 5-8 shows the shutter being actuated.



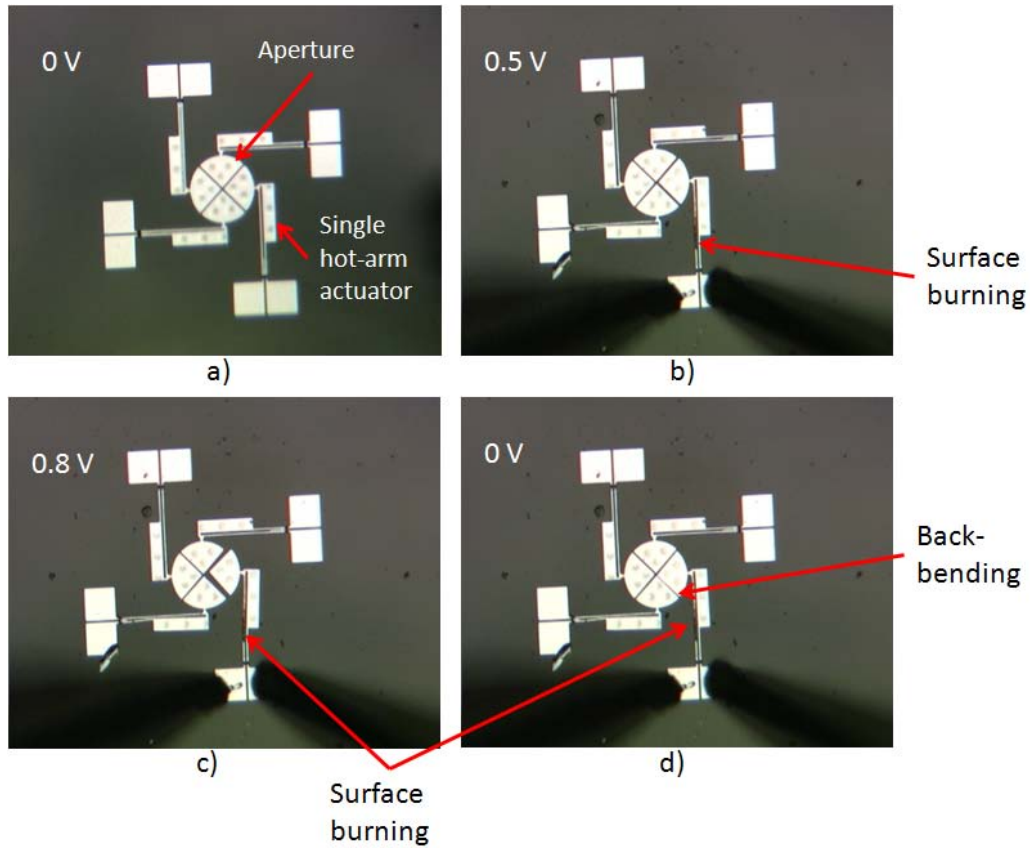


**Figure 5-8:** a) 100  $\mu\text{m}$  Al shutter prior to actuation. b) Shutter with 0.5 V actuation. Surface burning has already begun. c) Shutter at its maximum, 0.8 V. d) Shutter back-bent after being relaxed back to 0 V.

All of these wedges had the problem of undergoing plastic deformation, or back-bending, if they experienced currents of more than 100 mA; this translated to a voltage of approximately 0.7 V. As significant opening of the apertures was not achieved lower than 0.5 V, every wedge was back-bent after actuation. Despite these deformations, these wedges still repeated their actuation after ten tests. As no spacing markers were added in the design, the exact amount of deformation is not known, but it can be safely estimated to be within a range of 5-7  $\mu\text{m}$  when the input voltage is between 0.5-0.7 V.

### 5.3 Optical Results

The final task within this research effort was to optically characterize the various PolyMUMPS™ chips to test for failure due to overexposure. All chips were tested with a 632.8-nm, 1.5-mW HeNe laser to measure their absorptance, reflectance, and transmittance and thus determine their viability as a material for future microshutter work. Figure 5-9 is an illustration of the optical bench setup. First, the HeNe laser beam was passed through a Jodon spatial filter to remove all higher transverse electric and magnetic (TEM) modes of operation; the lowest order, or TEM<sub>00</sub> mode, is used for a multitude of reasons: the flux density is ideally Gaussian over the beam's cross section, there are no phase shifts in the electric field across the beam as there are in other modes, the beam's angular divergence is the smallest, and it can be focused down to the smallest-sized spot [1]. Once the beam has been spatially filtered, it passes through a 70-mm convex lens that focuses the beam onto a 60% reflective mirror that is oriented 45 degrees off-axis. After 40% of the original power has passed through the reflective mirror, it expands and is then focused onto the microshutter array on a PolyMUMPS™ chip mounted on a glass slide through another 70-mm convex lens; this spot size was an estimated 500-μm by 500-μm, thus encasing the 400-μm by 400-μm microshutter array. This 70-mm lens also captures the diffracting reflectance of the microshutter array and focuses it down again onto the reflective mirror. Two radiometers are then strategically placed to measure the transmittance and the reflectance; the absorptance is then subtracted from the original flux when no chip is present.



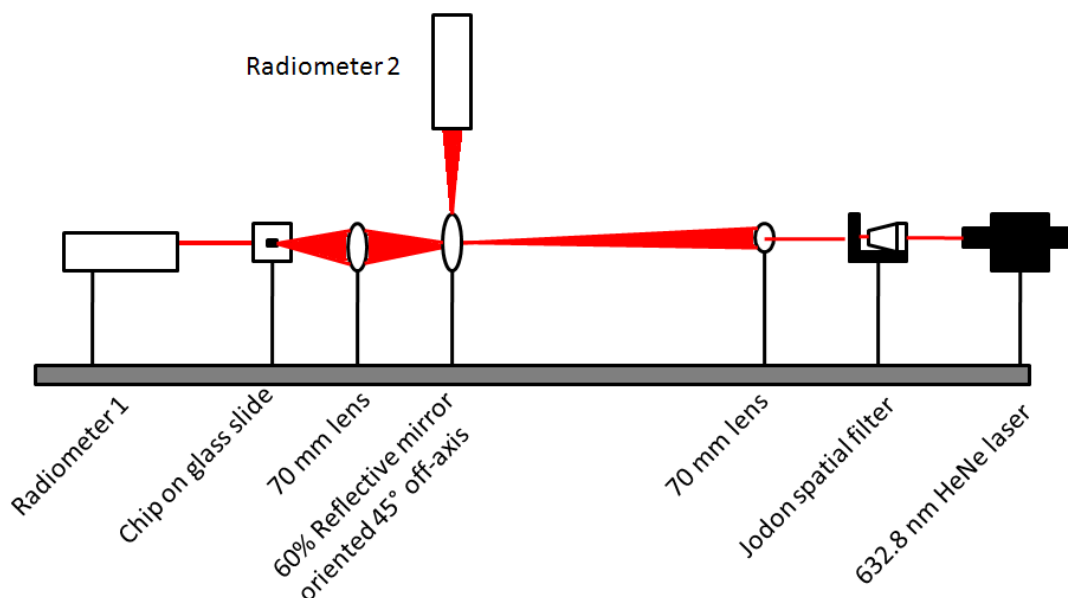


**Figure 5-9:** Optical setup to find  $\alpha$ ,  $\tau$ , and  $\rho$  coefficients for PolyMUMPS™ chips. The Jodon spatial filter passes only the TEM<sub>00</sub> mode of the 1.5 mW HeNe laser. The 70 mm convex lens focuses the beam onto a 60% reflective mirror that is designed to measure the reflection from the mounted chips. Radiometer 1 measures both the original flux and the transmittance, while Radiometer 2 measures the reflectance.

As most chips fabricated in Run 84 of PolyMUMPS™ did not survive the release process, only five chips had intact microshutter arrays that were available for optical testing. The average values are listed in Table 5-1 while figures of the results showing measured ranges for each coefficient are shown in Figure 5-10.

**Table 5-1:** Measured values for reflectance, transmittance, and absorptance from five chips from the PolyMUMPS™ process.

Average Value	Reflectance ( $\rho$ )	Transmittance ( $\tau$ )	Absorptance ( $a$ )
Run 84	42.18%	0.01056%	47.25570%

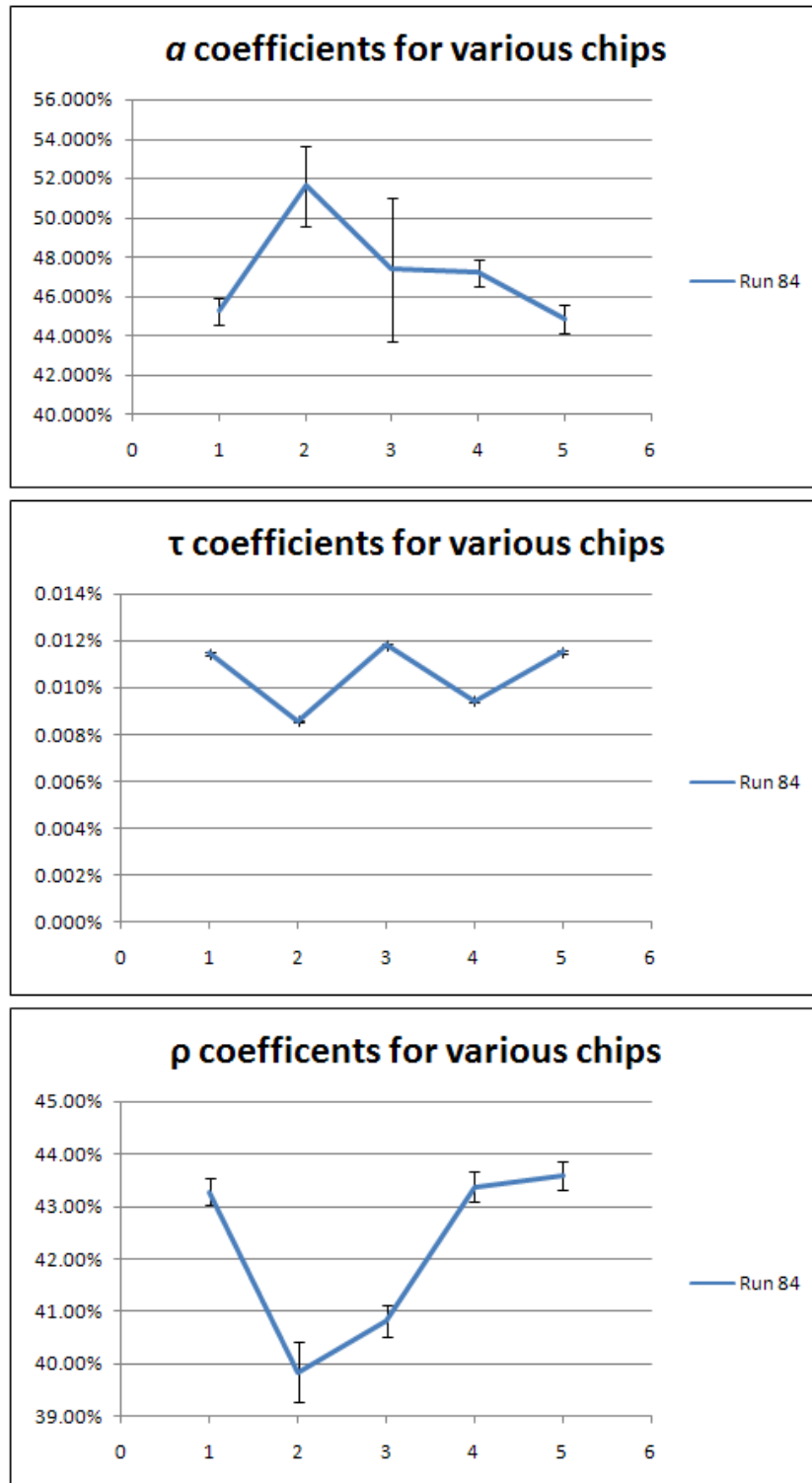


**Figure 5-10:** Charts illustrating the results of optical testing for five different microshutter arrays. The numbers along the x-axis represent each individual chip tested.

While all of the measured optical results are in relative agreement with each other, they do not coincide with those expected from theory. As stated in Section 4.4, the expected absorptance coefficients were to be between 60-65%, the reflectance near 20%, and transmittance near 15-20%. While none of the measured results are close to these numbers, they seem to agree more with common sense in that the transmittance is extremely small. In addition, because the solid angle between the microshutter array and the 70-mm lens is so small, some of the reflected light is lost, signifying that these reflectance measurements are still small. This is markedly higher than what is expected from theory.

Even with the disparities between theory and actual data, the temperature rise in the polysilicon layers was estimated. Given that the laser's output power is 1.5 mW and is passed through a 60% reflective mirror, 40% of the laser power, or 0.6 mW, is incident on the microshutter array. Using Equations 4.5-4.11 and the measured average reflectance, the temperature rise in the Poly2 shutters is only 1.86 K, and the temperature rise in the Poly1 shutters is 1.03 K. Neither of these temperatures are large enough to provide upward deflection in the microshutter array. It should be noted that it would take an estimated incident 0.5 W to melt the Poly2 shutters and an incident 0.8 W to melt the Poly1 shutters; this coincides to a 1.12 W source and a 2.03 W source, respectively.

## **5.4 Results Summary**

Obstacles through the fabrication process prevented much of the planned testing, but results were still found. First, due to the functionality of the individual wedges, it is fully expected that a wedge-style microshutter can be accomplished by using the

PolyMUMPS™ process, as long as sufficient space is provided between the wedges. With a more stringent fabrication process, the microshutter array might become functional, but that is dependent on the process's alignment requirements and conformality. Gear actuators were operated, but their lack of force meant they could not cause gear wheels to rotate. Aluminum shutters on a quartz wafer were characterized and actuated, further proving the functionality of the wedge-style shutter. Optical tests were run and determined that illumination of the polysilicon within PolyMUMPS™ will not undergo out-of-place deflection when illuminated by a 1.5 mW HeNe laser.

## **6. Conclusions and Recommendations**

### **6.1 Thesis Objectives Restated**

The goal of this effort was first and foremost to design a functioning microshutter array that allows the shutters to be as close as possible to each other. For this effort, an 8 x 8 array of 64 apertures measuring 18 microns x 18 microns spaced 22 microns apart was chosen, as typical small pixels tend to be approximately the same size. The array was designed to have as few macroscopic moving parts as possible, and was designed in such a way that each shutter within the array can be individually opened and closed. The actuation scheme was modeled in such a way as to predict its performance; this modeling also applied to the functioning of individual wedge-shaped shutters. These pie shutters were compared to an already fabricated wedge shutter from research sponsored by AFRL.

### **6.2 Conclusions**

First and foremost, the most prevalent problem encountered during this research stemmed from the inaccuracies of the PolyMUMPS™ process; tolerances within the design rules and alignment are not stringent enough for the requirements of this thesis. Despite the shortcomings of PolyMUMPS™, however, some progress has been made. It has been demonstrated that a wedge-style shutter would be fully functional if the wedges are given proper spacing; this increases the prospects of achieving a functional micro-optical-electro-mechanical-systems (MOEMS) device, if not directly applicable to ACAI. In addition, wedge-style shutters fabricated from aluminum were successfully actuated, further proving that wedge-style microshutters can be operational. Finally, the optical

properties of polysilicon were studied and acknowledged so that further MOEMS or ACAI elements fabricated from polysilicon can be designed with optical and temperature limits in mind.

### **6.3 Recommendations**

As the majority of the obstacles encountered in this thesis originated from the PolyMUMPS™ process, the first recommendation for future work is to explore other options for fabrication, whether it is in-house or by using another foundry process, such as Sandia National Lab's SUMMiT-IV or SUMMiT-V processes. The PolyMUMPS™ process was chosen for this effort due to its relatively low cost and turnaround time, but its loose tolerances with alignment severely limit the amount of work that can be designed for a functioning microshutter array. One key advantage that the two SUMMiT processes have over the PolyMUMPS™ process is that they have more than two releasable layers; the SUMMiT-IV process has three, while the SUMMiT-V process has four. In both cases, the releasable layers above the Poly2 layer are planarized and do not conform to the layers beneath them; this factor alone would provide many answers to design problems for a microshutter array. In addition, their spacing requirements are half of those found in PolyMUMPS™ due to stricter alignment requirements, thus opening the door to further microshutter designs.

Regardless of the fabrication process, a few key design areas must be fixed to achieve functionality of the microshutter array. The first area needing rework is that of the gear actuator. The actuation scheme must be redesigned so that it does not take up as much surface area on the chip, but can still provide the necessary force to move the

microshutter flaps, whether that is via a gear wheel or another device. A simple fix for this might be to make the gear actuator rely on a 4 x 4 scheme of banked electro-thermal actuators; this may provide the needed force to move microshutter flaps. The driving arm should also be designed to be thicker so that it can translate more of the force provided from the actuators to the gears. The lock actuator would then be redesigned; a simple fix to this would be to implement ratchet-like gear teeth on the microshutter flaps themselves and devise a method to release the ratchet, whether through electro-thermal actuation or another actuation method. Despite the redesigns, it is very likely that functioning microshutters can be fabricated through the PolyMUMPS™ process to create MOEMS, if not ACAI, devices.

## A. Appendix A

### A-1 PolyMUMPs™ Failed Wedge Shutter Designs

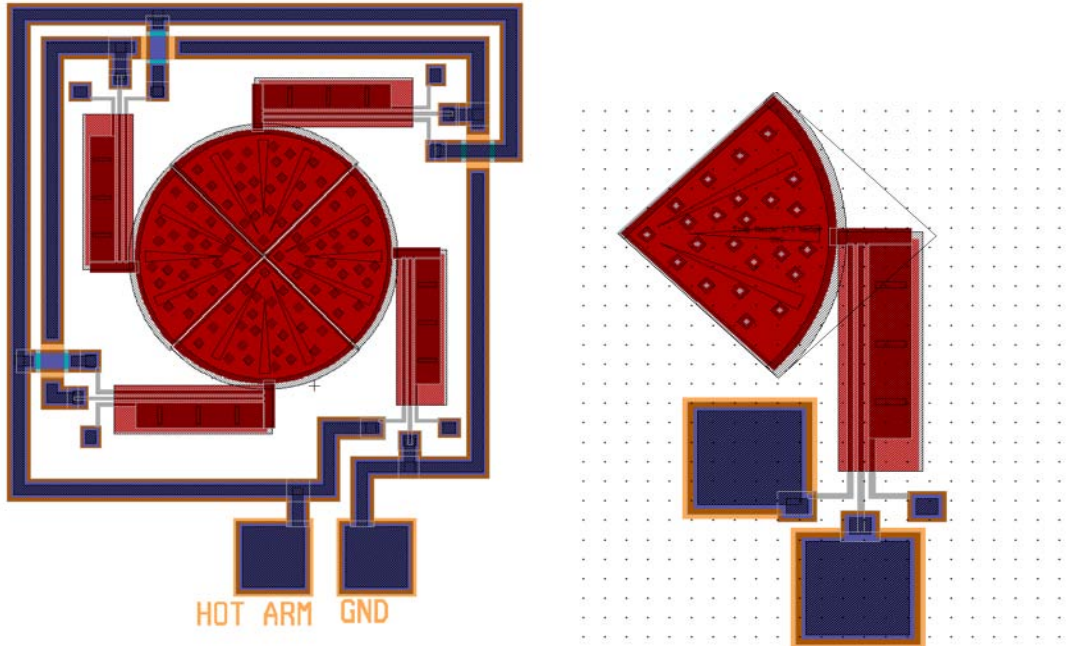


**Figure A-1:** Test design of a quarter-wedge, double hot arm shutter.

**Layout:** The hot arm is 150  $\mu\text{m}$  in length, and the wedge has a 100  $\mu\text{m}$  radius. This is a poly1-2 stack with a trapped oxide layer.

**Comments:** The bent hot-arm and anchor arms were detrimental to the function of this design. In each case, no deflection was seen before the electro-thermal actuators failed from overheating.



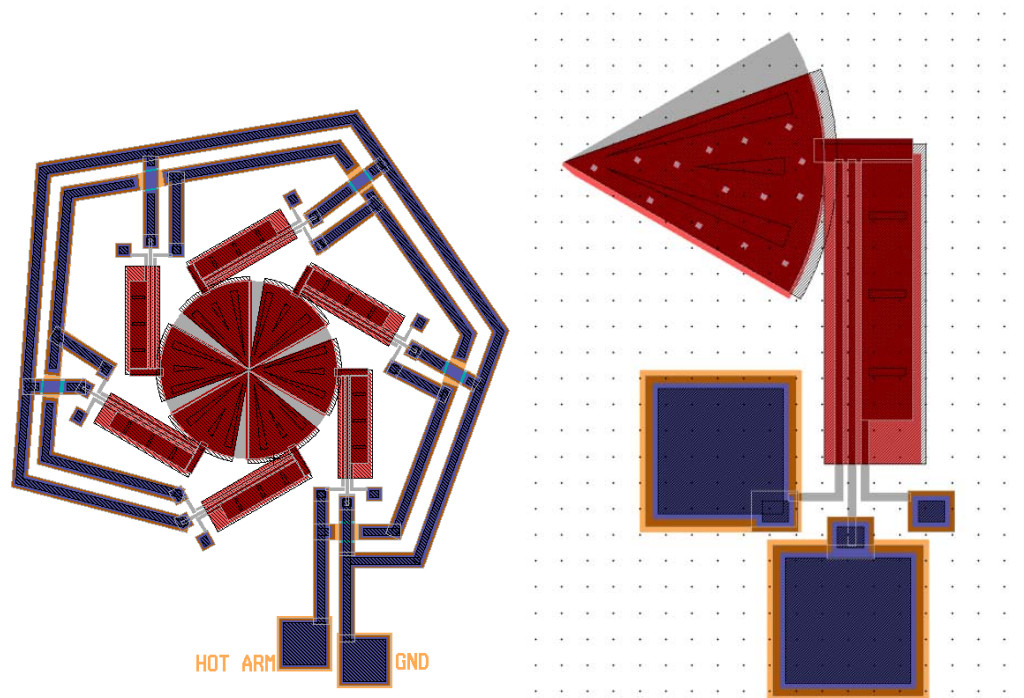


**Figure A-2:** Test design of a sixth-wedge, double hot arm shutter.

**Layout:** The hot arm is 150  $\mu\text{m}$  in length, and the wedge has a 100  $\mu\text{m}$  radius. This is a poly1-2 stack with no trapped oxide layer, and the extra flaps of polysilicon allow for more conformal covering of the aperture.

**Comments:** The bent hot-arm and anchor arms were detrimental to the function of this design. In each case, no deflection was seen before the electro-thermal actuators failed from overheating.

## A-2 Failed iris-style shutter using scratch drive actuation

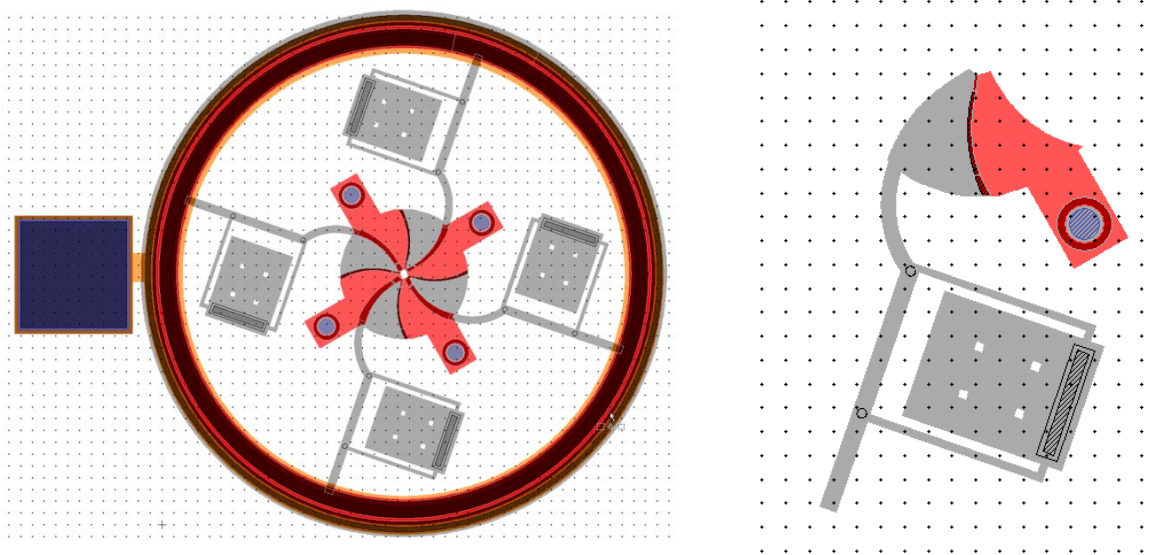


**Figure A-3:** (left) Iris-style shutter with scratch drive actuation, submitted to PolyMUMPS™ Run 84. (right) Individual wedge of iris-style shutter.

**Layout:** The four SDAs are attached to four flaps consisting of a Poly1 layer and a Poly 2 layer. The Poly1 layer is attached to the pivot anchor, and the Poly2 layer and SDA connected to it is directly clockwise from the Poly1 layer.

**Comments:** Like the wedge shutters, these were also fused. Also, because there is no closure mechanism designed into this shutter, the shutter would have remained open once it has undergone actuation.

### A-3 Failed flat shutter using scratch drive actuation

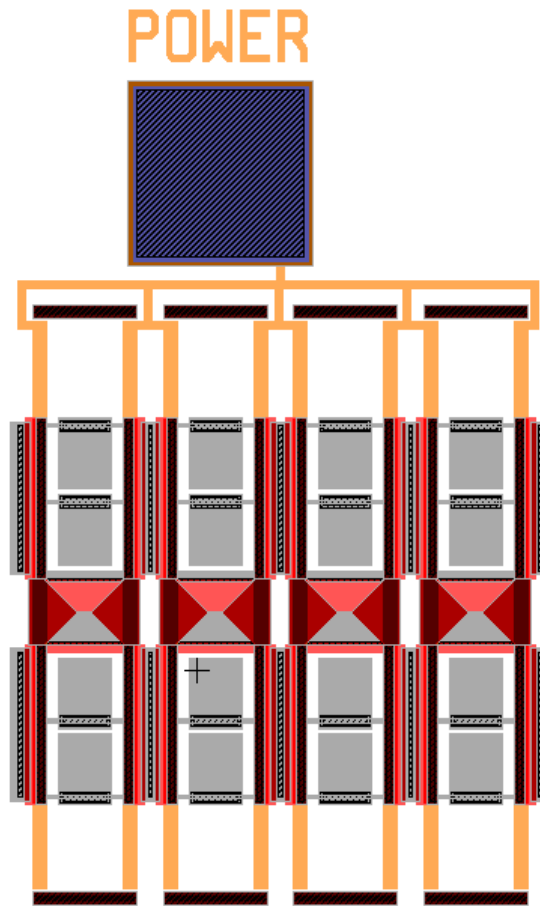


**Figure A-4:** Design of a 4x1 array of a flat shutter using SDAs, submitted to PolyMUMPS™ Run 85 for fabrication.

**Layout:** The two SDAs on the bottom of each shutter are designed to pull the Poly2 blade, while the two SDAs above each shutter are designed to pull the Poly1 blade. The substrate is used as ground, and so there are no ground contacts in this image.

**Comments:** As with the other failed shutters, these were entirely fused due to an oversight in design, rendering testing impossible.

## B. Appendix B

### B-1 PolyMUMPS™ Run 83 Submission

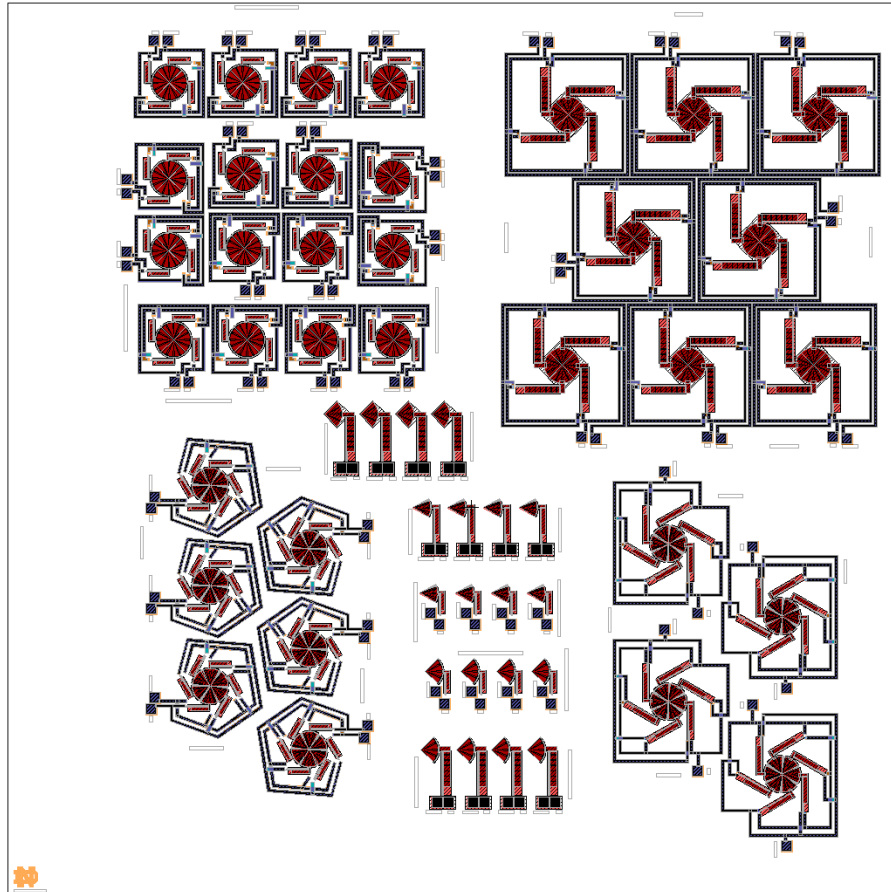


**Figure B-1:** Run 83 final design.

**Layout:** This was the first opportunity for a MEMS fabrication run, and so these designs were experimental in nature regarding the shape and size of the electro-thermal actuators to save as much surface area as possible.

**Comments:** All the full shutters on this run were fused together, but the wedges connected to the longer, single hot-arms were fully functional.

## B-2 PolyMUMPS™ Run 84 Submission

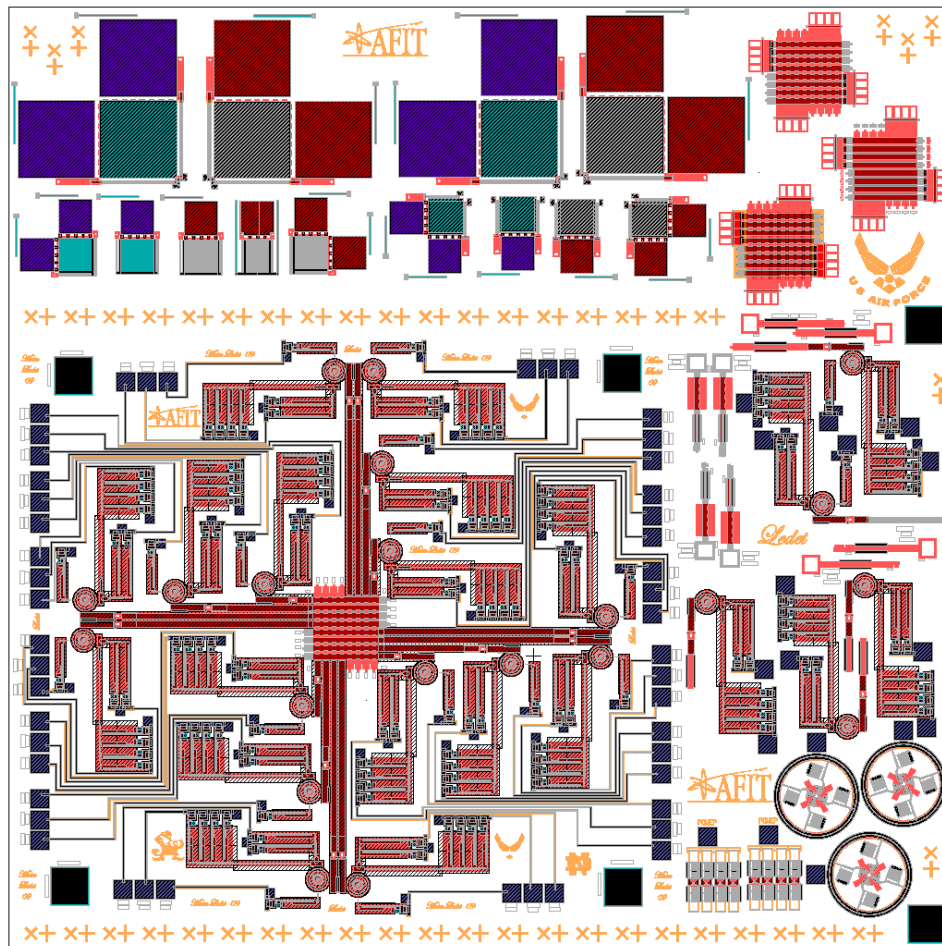


**Figure B-2:** Run 84 final design.

**Layout:** This was the final run submitted to PolyMUMPS™. This run includes the full microshutter array, its actuation schemes, and contact pads. It also includes test shutters using SDA actuation, extra gear actuators, and different microshutter layouts.

**Comments:** None of the extra microshutter layouts survived the release process, and all the shutters using SDAs were fused together.

## References

- [1] Hecht, E., "Optics, Fourth Edition", *San Francisco, Addison Wesley*, 2002.
- [2] Gottesman, S.R. "Coded apertures: past, Present, and Future Application and Design." *Proceedings of the SPIE*, Volume 6714, pp. 671405. 2007.
- [3] In 't Zand, J. "Coded Aperture Imaging Concept."  
<[http://astrophysics.gsfc.nasa.gov/cai/coded\\_intr.html](http://astrophysics.gsfc.nasa.gov/cai/coded_intr.html)>
- [4] "Microshutters." The James Webb Space Telescope at NASA.  
<<http://jwst.gsfc.nasa.gov/microshutters.html>>.
- [5] McNie, M.E, et al. "Reconfigurable Mask for ACAI based on an addressable MOEMS Microshutter Array." *Proceedings of the SPIE*, Volume 6714, pp. 67140B. 2007.
- [6] Slinger, C., et al. "An Investigation of the Potential for the Use of a High Resolution Adaptive Coded Aperture System in the Mid-Wave Infrared." *Proceedings of the SPIE*, Volume 6714, pp. 671408. 2007.
- [7] Osiander, Robert; Darrin, M. Ann Garrison; Champion, John. *MEMS and Microstructures in Aerospace Applications*. CRC Press. 2005.
- [8] Motohara, Kentaro; Takahasi, Takuya; Toshiyoshi, Hiroshi; Mita, Makoto; Kobayashi, Naoto; Kashikawa, Nobunari. "Development of microshutter arrays for ground-based instruments."  
<<http://ssed.gsfc.nasa.gov/gunther/gunther/motoharaELT2006.pdf>>.
- [9] "Countering Stiction." *Resolve Online Magazine*. Lehigh University. Vol 2. 2007.  
<[http://www3.lehigh.edu/engineering/resolvevol2/match\\_side\\_stiction.html](http://www3.lehigh.edu/engineering/resolvevol2/match_side_stiction.html)>.
- [10] Langley, D., Starman, L., Rogers, S. "Fabrication Studies for Scaling Photonic MEMS Micro-shutter Designs." *Proceedings of the SPIE*, Volume 7096, pp 70960G. 2008.
- [11] Mahalanobis, A., Neifeld, M., Vijaya Kumar, B.V.K., Haberfelde., T. "Design and Analysis of a Coded Aperture Imaging System with Engineered PSFs for Wind Field of View Imaging." *Proceedings of the SPIE*, Volume 7096, pp. 70960C. 2008.
- [12] Ravnkilde, Jan Tue, Larsen, Kristian Pontoppidan, Henningsen, Henning. "Fabrication of Nickel Microshutter Arrays for Spatial Light Modulation."  
<[www2.mic.dtu.dk/research/mems/publications/Papers/Dicon\\_Meso2002.pdf](http://www2.mic.dtu.dk/research/mems/publications/Papers/Dicon_Meso2002.pdf)>.

- [13] Zawadzka, J., Li, L., Uttamchandani, D. "Characterisation of a nanostepper driven optical shutter for application in free-space microoptics." IEE Proceedings-Scientific Measuring Technology. Vol 151, No 2. March 2004.
- [14] Carter, J., Cowen, A, Busbee, H., *et al*, "PolyMUMPs™ Design Handbook," Revision 11.0, MEMSCAP Inc., Copyright 1992-2005.
- [15] Starman, L., Langley, D., Rogers, S., "Micro-Shutter Developments for IR Applications." Proceedings of the SPIE, Volume 7096, pp. 70960K. 2008.
- [16] Platteborze, R. C., "Microelectromechanical Systems (MEMS) Safe and Arm Barrier for Low-Energy Exploding Foil Initiators (LEEFI)," *Master's Thesis*, Air Force Institute of Technology, AFIT/GEO/ENG/08-01, March 2008.
- [17] Zu, J.W., Qu, Q., Cheng, G, "Analytical Modeling and Quantitative Analysis of Scratch Drive Actuator," In Proceedings of International Conference on MEMS, NANO, and Smart Systems. 2004.
- [18] Li, L, Brown, J.G., Uttamchandani, D., "Study of Scratch Drive Actuator Force Characteristics," *Journal of Micromechanics and Microengineering*, Vol. 12, November 2002.
- [19] Denninghoff, D., "Power Scavenging MEMS Robot," *Master's Thesis*, Air Force Institute of Technology, AFIT/GE/ENG/06-17, March 2006.
- [20] Starman, L., "Characterization of Residual Stress in Microelectromechanical Systems (MEMS) Devices Using Raman Spectroscopy," *Dissertation*, Air Force Institute of Technology, AFIT/DS/ENG/02-01, April 2002.
- [21] Dereniak, E. L., Boreman, G. D., "Infrared Detectors and Systems," *Wiley-Interscience*, April 2006.
- [22] Y. Laghla, E. Scheid, Optical study of undoped, B or P-doped polysilicon, *Thin Solid Films*, Volume 306, Issue 1, August 1997, Pages 67-73.
- [23] J. Zou, M. Balberg, C. Byrne, C. Liu, and D. Brady, "Optical Properties of Surface Micromachined Mirrors with Etch Holes," *Journal of Microelectromechanical Systems*, vol. 8, no. 4, p. 506–513, December 1999.

## **Vita**

Captain Mary M. Ledet lived in Alabama, Iowa, Indiana, and Tennessee before graduating from high school. She graduated as valedictorian of the class of 2000 from Centennial High School in Franklin, TN. She went on to earn her undergraduate degree in electrical engineering from the University of Notre Dame, where she graduated magna cum laude in 2004. While at Notre Dame, she was a member of the university's AFROTC detachment and received her commission in 2004.

Captain Ledet's first assignment was at Kirtland AFB where she was assigned to the Airborne Laser (ABL) System Program Office (SPO), Beam Control/Fire Control (BCFC) Branch. There, she specialized in the technical management and aircraft installation of the Beacon Illuminator Laser (BILL) and Tracking Illuminator Laser (TILL). In February 2006, she was selected to be a keyboardist for the Air Force's Expeditionary Entertainment group, Tops in Blue. While a member of Tops in Blue, she performed 150 shows in 30 countries within a 10-month time span, and also functioned as a flight chief for five of her other team members. She returned to the ABL SPO in April 2007, and was reassigned to the Advanced Capabilities Technology Insertion Branch. In August 2007, she enrolled at the Air Force Institute of Technology, Wright-Patterson AFB, where she was a student of the Electro-Optics program. Upon graduation, she will be assigned to the Air Force Research Laboratory, Materials Directorate. She is a member of Eta Kappa Nu and Tau Beta Pi.





REPORT DOCUMENTATION PAGE				Form Approved OMB No. 074-0188	
<p>The public reporting burden for this collection of information is estimated to average 1 hour per response, including the time for reviewing instructions, searching existing data sources, gathering and maintaining the data needed, and completing and reviewing the collection of information. Send comments regarding this burden estimate or any other aspect of the collection of information, including suggestions for reducing this burden to Department of Defense, Washington Headquarters Services, Directorate for Information Operations and Reports (0704-0188), 1215 Jefferson Davis Highway, Suite 1204, Arlington, VA 22202-4302. Respondents should be aware that notwithstanding any other provision of law, no person shall be subject to a penalty for failing to comply with a collection of information if it does not display a currently valid OMB control number.</p> <p><b>PLEASE DO NOT RETURN YOUR FORM TO THE ABOVE ADDRESS.</b></p>					
1. REPORT DATE (DD-MM-YYYY) 26-03-2009		2. REPORT TYPE Master's Thesis		3. DATES COVERED (From - To) March 2008 - March 2009	
4. TITLE AND SUBTITLE  Utilizing Microelectromechanical Systems (MEMS) Micro-Shutter Designs for Adaptive Coded Aperture Imaging (ACAI) Technologies				5a. CONTRACT NUMBER	
				5b. GRANT NUMBER	
				5c. PROGRAM ELEMENT NUMBER	
6. AUTHOR(S)  Ledet, Mary M., Captain, USAF				5d. PROJECT NUMBER ENG-08-180	
				5e. TASK NUMBER	
				5f. WORK UNIT NUMBER	
7. PERFORMING ORGANIZATION NAME(S) AND ADDRESS(S) Air Force Institute of Technology Graduate School of Engineering and Management (AFIT/EN) 2950 Hobson Way, Building 640 WPAFB OH 45433-8865				8. PERFORMING ORGANIZATION REPORT NUMBER  AFIT/GEO/ENG/09-03	
9. SPONSORING/MONITORING AGENCY NAME(S) AND ADDRESS(ES) Air Force Research Laboratory Attn: Mr. Stanley Rogers Stanley.rogers@wpafb.af.mil 2241 Avionics Circle, Bldg 620 WPAFB, OH 45433-7301 DSN: 674-9953				10. SPONSOR/MONITOR'S ACRONYM(S) AFRL/RYDX	
				11. SPONSOR/MONITOR'S REPORT NUMBER(S)	
12. DISTRIBUTION/AVAILABILITY STATEMENT  Approved for Public Release; Distribution Unlimited					
13. SUPPLEMENTARY NOTES					
14. ABSTRACT <p>The Air Force has long relied on surveillance for intelligence and strategic purposes. Most surveillance systems rely on a lensing system to acquire their images, most of which are in either the visible or infrared wavelengths. Because lensing systems can be expensive, obtrusive, or hard to maintain, researchers have designed adaptive coded aperture imaging (ACAI) as a replacement system. Coded aperture imaging (CAI) has been used in both the astronomical and medical communities for years due to its ability to image light at short wavelengths and thus replacing conventional lenses. Where CAI is limited, researchers have discovered that adaptive coded aperture imaging can recover what is lost. ACAI uses a reconfigurable coding mask and digital signal processing to recover the original scene from the detector.</p> <p>In this effort, a prototype of MEMS microshutters has been designed and fabricated onto a 3 mm x 3 mm square of silicon substrate using the PolyMUMPS™ process. This prototype is a line-drivable array using thin flaps of polysilicon to cover and uncover an 8 x 8 array of 20 μm apertures and is the first known microshutter array to incorporate a line-drivable array driven by physical actuation. A characterization of the micro-shutters to include mechanical, electrical and optical properties is provided. This prototype, its actuation scheme, and other designs for individual microshutters have been modeled and studied for feasibility purposes, and this revealed that the actuation scheme failed in its design due to oversights in the design process and lack of space for each gear actuator. Because of conformality in the PolyMUMPS™ process, none of the microshutters could physically move, but optical analysis with a 632 nm HeNe laser revealed that they will not undergo upward deflection when exposed to irradiance sources of less than 0.5 W. The microshutters were also designed to transmit less than 20% of irradiated light and initial testing confirmed that fact. In addition, microshutters fabricated from an Al-Au alloy on a quartz wafer were characterized and showed that wedge-style shutters are functional, if not ideal for an ACAI array.</p>					
15. SUBJECT TERMS Microelectromechanical Systems; Adaptive Coded Aperture Imaging; Microshutters; Coded Aperture Imaging					
16. SECURITY CLASSIFICATION OF: Unclassified			17. LIMITATION OF ABSTRACT  UU	18. NUMBER OF PAGES  131	19a. NAME OF RESPONSIBLE PERSON La Vern A. Starman, Maj, USAF
a. REPORT  U	b. ABSTRACT  U	c. THIS PAGE  U			19b. TELEPHONE NUMBER (Include area code) (937) 255-3636, ext 4618 (LaVern.Starman@afit.edu)

